Novel Models for High-Dimensional Imaging: High-Resolution fMRI Acceleration and Quantification

by

Shouchang Guo

A dissertation submitted in partial fulfillment
of the requirements for the degree of
Doctor of Philosophy
(Electrical and Computer Engineering)
in the University of Michigan
2022

Doctoral Committee:

Professor Jeffrey A. Fessler, Co-Chair
Professor Douglas C. Noll, Co-Chair
Associate Professor Laura K. Balzano
Assistant Professor David F. Fouhey

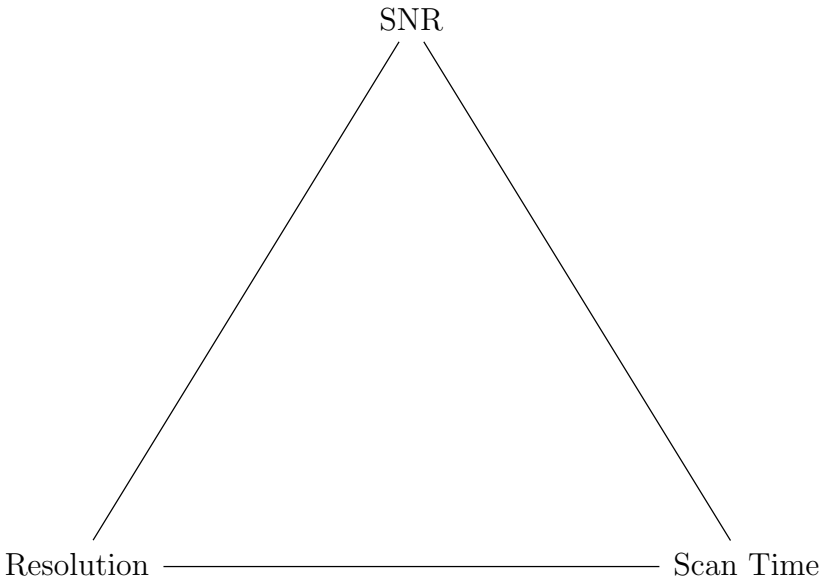
SNR
Resolution
Scan Time

Shouchang Guo

shoucguo@umich.edu

ORCID iD: 0000-0002-0329-1638

To mom and dad, grandparents, water and wind.

ACKNOWLEDGEMENTS

As a student who knew nothing about medical imaging when started, I am eternally grateful to my advisors Prof. Doug Noll and Prof. Jeff Fessler for their trust and patience, and for everything I have learned to become who I am today. Their genuine zest and devotion for science and teaching, and genuine care and support for our growth have always been the source of courage and enthusiasm for me. Prof. Noll's incredible insights and intuition, and profound knowledge of physics and MRI have guided me through darkness and uncertainty at every stage of research. It is magnificent and magical to see how Prof. Fessler tackles sophisticated problems with elegant mathematical modeling and inspiring flows of equations. I have been extremely lucky to learn from both of them about how to connect and innovate, how to solve problems with intuition and skills, and how to pursue my goals with passion and perseverance.

I am deeply grateful to my committee members Prof. Laura Balzano and Prof. David Fouhey for their guidance and encouragement, all the invaluable ideas and advice, and their amazing research that intrigues me to think above and beyond.

I want to express my deep appreciation to all the senior members in the group, Drs. Scott Peltier, Jon-Frederik Nielsen, Luis Hernandez-Garcia, Kathleen Ropella, Sydney Williams, Tianrui Luo, Anish Lahiri, Amos Cao, Melissa Haskell, Sai Ravishankar, David Hong, Hao Sun, Jiabei Zheng, and my roommate Dr. Shriya Sethuraman for their generous support and all the important insights and discussions that help me grow.

I have been very fortunate to have spent innumerable happy hours with my friends and labmates Michelle Karker, Claire Lin, Dinank Gupta, Guanhua Wang, Mingjie Gao, Haowei Xiang, Mariama Salifu, Caroline Crockett, Cameron Blocker, Naveen Murthy, Steven Whitaker, Eric Cheek, Tao Hong, Xijia Quan, David Frey, and others.

Special thanks to NIH Grants U01EB026977 and R01EB023618. I also wish to thank all the participants in MRI studies and staff members Kristen Thornton, Theresa Russ, Kim Sharma, and others for being so kind and supportive. Ann Arbor

is such a beautiful place with all the great people.

Finally, I want to thank my parents, grandparents, my brother, and my all-time best friends, for their love and trust, and their sometimes unwarranted confidence in me.

"What does a fish know about the water in which he swims all his life?" It has been a wonderful journey with infinite dimensions of things that I do not know, and I hope that I have infinite courage and enthusiasm to learn and do something meaningful.

TABLE OF CONTENTS

LIST OF FIGURES

Figure

LIST OF TABLES

Table

ABSTRACT

The goals of functional Magnetic Resonance Imaging (fMRI) include high spatial and temporal resolutions with a high signal-to-noise ratio (SNR). We introduce a novel method for fMRI named *Oscillating Steady-State Imaging (OSSI)*. OSSI can provide 2 to 3 times higher SNR than the standard method. However, the SNR improvement comes at a cost of spatial-temporal resolution.

To simultaneously improve spatial and temporal resolutions and maintain the high SNR advantage of OSSI, we present novel pipelines for fast acquisition and high-resolution fMRI reconstruction and physics parameter quantification. We design a sparse sampling pattern to accelerate scan time. Because OSSI images are high-dimensional, we propose a *patch-tensor low-rank model* to exploit the local spatial-temporal low-rankness of the images. The proposed method enables high-resolution 3D fMRI with a factor 10 acceleration and 1.3 mm spatial resolution, and yields 2 times higher SNR than the standard fMRI methods with 2 times more brain activation.

To accurately model the nonlinearity of OSSI oscillation pattern, instead of applying subspace models that might not be perfectly suited for the data, we propose a *physics-based manifold model* that builds the MR physics for OSSI signal generation as a regularizer for the undersampled reconstruction. The proposed manifold model reconstructs high-resolution fMRI images with high SNR and a factor of 12 acceleration. Furthermore, the model enables dynamic tracking of important physics parameters for more accurate brain activity monitoring with a 150 ms temporal resolution.

To exploit learning-based approaches for dynamic MRI with better temporal modeling and richer representations, we propose a *voxel-wise attention network* that combines MR physics with the attention mechanism for temporal learning and mapping. We also develop a two-stage learning scheme to resolve the training data limitation. The proposed network reconstructs dynamic MRI sequences with a factor of 12 undersampling and provides high-quality functional maps with 4 times faster reconstruction

than model-based approaches.

With novel models for acquisition and reconstruction, we demonstrate that we can improve SNR and resolution simultaneously without compromising scan time. All the proposed models outperform other comparison approaches with higher resolution and more functional information.

CHAPTER I

Introduction

1.1 Motivation

Three factors, simple but overwhelmingly important, have governed the quality of magnetic resonance imaging (MRI): the signal-to-noise ratio (SNR), the resolution, and the scan time. The trade-offs among SNR, resolution, and scan time, have been sources of inspiration for MRI research.

In functional MRI (fMRI), a time series of MRI images are acquired to track brain activity. Because signal changes for brain activation are very small, we need high SNR to distinguish brain signals from noise sources. Because functional units of the brain are on the order of 1 mm or smaller, we need fine spatial resolution to precisely locate functional signals. As SNR is proportional to voxel size, high SNR is essential for high spatial resolution. To achieve high spatial resolution or high SNR, traditional methods must increase scan time for each image in the fMRI time series. The increased scan time per image or decreased temporal resolution would diminish the temporal accuracy of fMRI signals.

1.2 Background

1.2.1 High SNR Functional MRI

Functional MRI acquires a time series of MRI images to track brain activity. The SNR of an fMRI image [1, 2, 3] is determined by

$$\text{SNR} \propto BCV\sqrt{T}, \tag{1.1}$$

where B represents magnetic field strength, C is a head coil dependent term, V is the voxel volume for the brain image, and T is proportional to the scan time for each image. The scan time for collecting each of the images in the time series is also referred to as the temporal resolution of fMRI.

Brain activity related signal changes are small and can be easily buried in noise. As SNR is proportional to voxel volume and functional units of the brain are on the order of 1 mm or smaller, high SNR is critical for high-quality and high-resolution fMRI. However, current methods for SNR improvement are limited.

Improvements in B and C require a new set of hardware. Increasing B with higher field strength systems is a costly investment and leads to severe distortion issues in the images. Increasing the number of coils for C in a head array suffers from diminishing returns as coil elements get smaller, particularly for deep brain structures.

For software related factors, V and T correspond to spatial resolution and scan time of an image, respectively. There is a triangle trade-off between SNR, spatial resolution, and scan time in MRI. To increase the SNR, one would need to increase scan time, or compromise resolution; to improve resolution, SNR would be sacrificed or the scan time would need to increase; to reduce scan time, the SNR and/or the resolution of the image would decrease. It is very hard to improve all three factors at the same time, and the main goal of this thesis is to improve SNR, resolution, and scan time simultaneously without costly equipment.

1.2.2 High-Resolution Image Reconstruction

In MRI, the data collected via scanning are in "k-space", and a Fourier transform relationship holds between the object image and the acquired k-space data [4, 5]. Therefore, the k-space is basically the Fourier domain of an MRI image, and the simplest way to reconstruct the image is to take the inverse Fourier transform of the k-space data. Collecting data with a larger k-space extent can increase spatial resolution at the expense of scan time.

To improve resolution without compromising scanning time, compressed sensing [6, 7] and model-based reconstruction [8, 9] propose random sparse sampling (dramatically reduced sampling rates compared to the Nyquist sampling criteria) in k-space. Furthermore, prior information on images is imposed to solve the undetermined problem with a limited amount of measurements. The image reconstruction problem is

formulated as

$$\arg\min_{\mathbf{x}} \frac{1}{2}\|\mathcal{A}(\mathbf{X}) - \mathbf{y}\|_2^2 + \alpha\mathcal{R}(\mathbf{X}), \tag{1.2}$$

where $\mathbf{X}$ are the images to be reconstructed, and $\mathbf{y}$ denotes the small number of k-space measurements. $\mathcal{A}$ is a linear operator representing the MR physics, and $\mathcal{A}$ represents the Fourier transform for single-coil MRI with Cartesian sampling. $\mathcal{R}(\cdot)$ regularizes the images with prior information and assumptions. α is the regularization parameter.

Typical priors used as constraints on the images include total variation [8, 9], low-rank and/or sparse [10, 9, 11], and learned dictionary [12]. Recent works [13, 14, 15] use neural networks as regularizers for undersampled reconstruction. In this work, we propose novel models and techniques for high SNR and high-resolution fMRI image reconstruction.

1.3 Outline and Contributions

This thesis is organized as follows:

Chapter II, published in [16], describes a new Oscillating Steady-State Imaging (OSSI) method for high SNR fMRI. OSSI establishes a new steady state by combining balanced gradients in balanced steady-state free precession [17] and quadratic RF phase progression in RF-spoiled GRE [18]. The resulting oscillating steady-state signal combines high SNR of the balanced steady state and the T_2^* contrast of gradient echo (GRE) imaging for fMRI. OSSI provides at least 2 times higher SNR than standard GRE fMRI without costly equipment investments. However, the SNR advantage of OSSI comes at a price of spatial and temporal resolutions.

Chapter III, published in [19], describes a novel pipeline for fast acquisition and high-resolution and high-dimensional fMRI. As the unique oscillation pattern of OSSI images makes it well suited for high-dimensional modeling, we propose a patch-tensor low-rank model to exploit the inherent high-dimensional structures and local spatial-temporal low-rankness of the images. We also develop a practical sparse sampling scheme with improved sampling incoherence. With an alternating direction method of multipliers based algorithm, we improve OSSI spatial and temporal resolutions with a factor of 12 acquisition acceleration and 1.3 mm isotropic spatial resolution in prospectively undersampled experiments. Compared to the standard GRE imaging at the same spatial-temporal resolution, the proposed model demonstrates 2 times

higher SNR with 2 times more functional activation.

Chapter IV, under revision and available in [20], describes a new manifold model for high-resolution fMRI joint quantification and reconstruction. Because OSSI signals exhibit a nonlinear oscillation pattern and to accurately model the nonlinearity, instead of using subspace models that might not be perfectly suited for the data, we build the MR physics for OSSI signal generation as a regularizer for the undersampled reconstruction. Our proposed physics-based manifold model turns the disadvantages of OSSI acquisition into advantages. OSSI manifold model (OSSIMM) outperforms subspace models and reconstructs high-resolution fMRI images with a factor of 12 acceleration and without spatial-temporal smoothing. Furthermore, OSSIMM can dynamically quantify and track important physics parameters for more accurate brain activity monitoring with a 150 mm temporal resolution.

Chapter V describes a novel learning-based approach and training scheme for dynamic MRI acceleration and reconstruction. Because learning-based temporal modeling in dynamic MRI is an open question and often requires large amounts of training data, we propose a voxel-wise attention network that incorporates an attention mechanism for temporal learning and mapping. The proposed network combines MR physics with a data fidelity layer for end-to-end inference. We also develop a two-stage learning scheme that pretrains the network with voxel-wise simulated data, and then fine-tunes with human data to resolve the lack of training data. Our proposed model reconstructs dynamic MRI images with a factor of 12 undersampling, and provides high-quality images and functional maps. The proposed voxel-wise, attention-based model can potentially be used for MR fingering reconstruction and other dynamic reconstruction applications.

Chapter VI proposes future work on other novel spatial-temporal models for MRI image sequence reconstruction and acceleration.

CHAPTER II

Oscillating Steady-State Imaging (OSSI): A Novel Method for Functional MRI

Signal-to-noise ratio (SNR) is crucial for high-resolution fMRI, however, current methods for SNR improvement are limited. A new approach, called Oscillating Steady-State Imaging (OSSI), produces a signal that is large and T_2^*-weighted, and is demonstrated to produce improved SNR compared to gradient echo (GRE) imaging with matched TE and spatial-temporal acquisition characteristics for high-resolution fMRI. Quadratic phase sequences were combined with balanced gradients to produce a large, oscillating steady-state signal. The quadratic phase progression was periodic over short intervals such as 10 TRs, inducing a frequency-dependent phase dispersal. Images over one period were combined to produce a single image with effectively T_2^*-weighting. The OSSI parameters were explored through simulation and phantom data, and 2D and 3D human fMRI data were collected using OSSI and GRE imaging. Phantom and human OSSI data showed highly reproducible signal oscillations with greater signal strength than GRE. Compared to single slice GRE with matched TE and spatial-temporal resolution, OSSI yielded more activation in visual cortex by a factor of 1.84 and an improvement in temporal SNR by a factor of 1.83. Voxelwise percentage change comparisons between OSSI and GRE demonstrate a similar T_2^*-weighted contrast mechanism with additional T_2'-weighting of about 15 ms immediately after the RF pulse. OSSI is a new acquisition method that exploits a large, oscillating signal that is T_2^*-weighted and suitable for fMRI. The steady-state signal from balanced gradients creates higher signal strength than single slice GRE at varying TEs, enabling greater volumes of functional activity and higher SNR for

high-resolution fMRI. [1]

2.1 Introduction

Because the signal-to-noise ratio (SNR) in MRI is proportional to voxel volume, and the functional units of the brain are on the order of 1 mm, high SNR is required for functional MRI (fMRI) of these small brain structures. Many common methods for improving SNR have already been well-used, but now face limitations. For example, extending readouts increases sensitivity to off-resonance distortions, and increasing the number of coils in a head array suffers from diminishing returns as coil elements get smaller, particularly for deep brain structures. One can also enhance SNR by going to higher field systems, but this requires a costly investment. Thus, there is a compelling need for alternative approaches to improving the SNR in fMRI.

Functional MRI using the blood oxygenation (BOLD) effect has been based on T_2^*-weighted gradient echo (GRE) imaging from its inception and has commonly been implemented using single-shot fast imaging methods like echo-planar imaging (EPI) or spiral imaging. There has also been some work on acquisition using steady-state methods. These include T_2^*-weighted, 3D GRE acquisitions of several variations [23, 24] and short TR, fast recovery (STFR) sequences that preserve magnetization through principles of driven equilibrium [25]. There are also variants of balanced steady-state methods like balanced steady-state free precession (bSSFP, also known as True FISP, FIESTA, bFFE), such as transition-band bSSFP [26, 27], have exploited shifts in resonant frequency associated with changes in blood oxygenation. At the same time, blood oxygenation changes have also led to observable signal changes using passband bSSFP resulting from changes in T_2 directly and from diffusive effects around small vessels [28, 29, 30].

Standard implementations of bSSFP use constant excitation phase or a linear phase sequence for RF pulses. In this work we use a similar balanced-gradient pulse sequence, but with quadratic phase sequences, which is equivalent to a linearly sweeping frequency. Since the frequency response is periodic in the frequency domain, a frequency sweep will lead to periodic signal oscillation. We note that if the gradients are not balanced (e.g. gradient spoiled), the quadratic phase sequence will lead to a RF-spoiled gradient echo acquisition, provided that the sweep rate is sufficiently

[1] This chapter was published in [16, 21, 22].

fast. Also, if the quadratic phase sequence is sufficiently slowly evolving, then the balanced-gradient acquisition leads to contrast that is very similar to the standard bSSFP contrast though the response slowly shifts over time. In this work, we explore a novel domain using balanced-gradients but with a quadratic phase sequence that is rapid, having a period on the order of 10 TRs, which leads to an oscillatory signal. We refer to this approach as Oscillating Steady-State Imaging (OSSI). We show that the OSSI signal is large compared to Ernst angle GRE imaging and further show that the OSSI signal is sensitive to changes in T_2^*, making it suitable for high-resolution fMRI. We distinguish our approach using quadratic phase sequences from other oscillatory steady states resulting from sequences of alternating patterns of phase [31, 32], which have a different contrast.

In this work, we demonstrate a novel fMRI acquisition method that has the potential to improve the SNR over GRE with matched TE and spatial-temporal acquisition characteristics. It focuses on a unique oscillating steady-state source of signal that is large and T_2^*-weighted, and we explore its signal properties in both simulation and experimental studies.

2.2 Theory

2.2.1 Oscillating Steady-State Imaging

Quadratic phase sequences in conjunction with a constant gradient dephasing is a well-recognized approach for establishing a spoiled steady state. The sequence is typically applied using the RF phase increment [33]

$$\phi(n) - \phi(n-1) = \psi_A n + \psi_B, \tag{2.1}$$

where ψ_A is commonly chosen to provide full cancellation of the transverse magnetization prior to the next RF pulse; typical values for spoiling are $\psi_A = 117°, 50°, 150°$, etc. The constant term, ψ_B, represents a constant frequency shift and is not important in most of these analyses. The linear phase increment is equivalent to a quadratic phase sequence, for example, $\phi(n) = \psi_A n^2/2$ is the same as in (2.1) for the case of $\psi_B = -\psi_A/2$. In this work, we examine such quadratic phase sequences with balanced gradients, which maintains the steady-state components leading to stronger signals. This approach was proposed by Foxall [34] to implement bSSFP with T_2-like

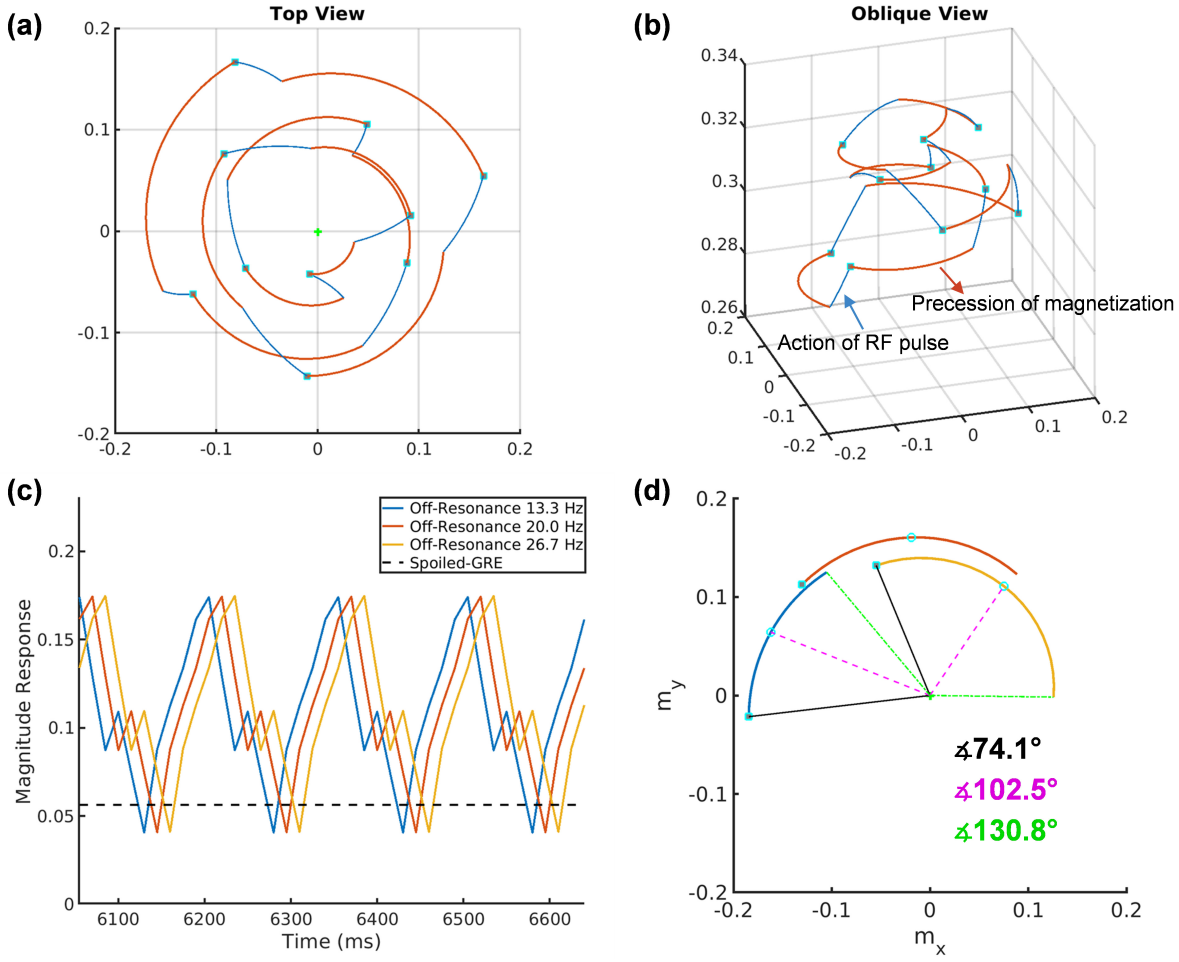

Figure 2.1: Simulation of OSSI spin behavior and signals.
(a) and (b) Periodic motion of magnetization through RF pulses (the filled squares are at the end of the RF pulse) and free precession for a gray matter spin at -20 Hz off-resonance frequency, $T_1 = 1433.2$ ms, $T_2 = 92.6$ ms, TR = 15 ms, $n_c = 10$, and FA = 10° from two different views. (c) Magnitude signal variation of different isochromats (6.67 Hz apart) for the magnetization in (a) and (b) just after the RF pulse, the black dashed line is the Ernst angle signal for spoiled-GRE. (d) Spin positions during free precession for different isochromats (same isocromats as in (c)) leading to phase dispersion and T_2^*-weighting. The cyan circles mark the center of the precession interval.

weighting whereby the frequency-dependent bands in image intensity slowly shifted over the acquisition. Foxall argued that bSSFP-like contrast would be preserved if the phase increment is kept small ($\psi_A < 3°$). We have observed that larger phase increments also leads to steady-state signals, however that the contrast is no longer similar to bSSFP contrast, but instead has contrast that is both T_2- and T_2'-weighted, and thus effectively T_2^*-weighted. With appropriate selection of ψ_A, the phase sequence can be made to be periodic with cycle length n_c by setting

$$\psi_A = \frac{2\pi}{n_c}. \tag{2.2}$$

This periodic sequence leads to oscillations in the steady-state signal with period $\mathrm{T_{OSSI}} = n_c\mathrm{TR}$. Maintenance of transverse components via a steady state tends to make the resultant signals T_2-weighted, while the different phases of different isochromats lead to T_2'-weighting. We note that Wang et al. [35] have similarly observed that quadratic phase RF pulses lead to frequency dependent phase variations and T_2^*-weighting.

The OSSI signals have a variety of interesting properties. Like bSSFP, the OSSI response is frequency dependent and the spectral properties are periodic with 1/TR in the frequency domain. Further, it can be shown that shifts in frequency will lead to signal being shifted in time. Specifically, a frequency shift of $1/\mathrm{T_{OSSI}}$ will lead to the phase sequence being shifted by exactly one TR, which leads to the OSSI response being similarly shifted in time by one TR. Note that a frequency shift of $1/\mathrm{T_{OSSI}}$ is equivalent to $\Delta\psi_B = 2\pi/\mathrm{T_{OSSI}}$. Frequency shifts that are not integer multiples of $1/\mathrm{T_{OSSI}}$ will also have oscillatory behavior, but with slightly different temporal signal responses. Thus, different isochromats within an image will have unique time courses, each of which is periodic with $\mathrm{T_{OSSI}}$, and depending on the frequency, these time courses will be shifted in time and/or have slightly different shape. The shifts in time for different isochromats induces a frequency dependent phase dispersal, effectively leading to T_2^*-like contrast. In order to produce a stable and usable time course for fMRI analyses, we commonly combine the n_c images for one period of the OSSI signal by some method, for example using root mean square (RMS) or 2-norm combination.

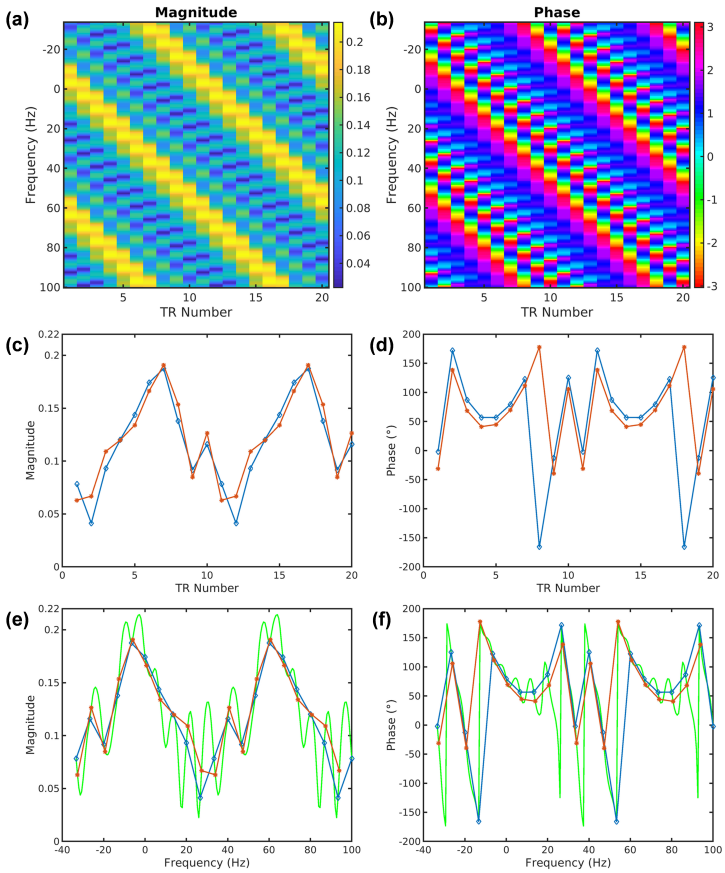

Figure 2.2: Simulation for signal properties just after the RF pulse, where the pulse duration was adjusted to minimize off-resonance phase accumulation during the RF pulses (TE $<$ 0.02 ms). The left and right panels show simulated OSSI signal magnitude and phase, respectively. (a) and (b) show magnitude and phase responses as a function of off-resonance frequency and time (TR number), observe the periodicity in time ($T_{OSSI} = n_c TR$) and frequency ($1/TR = 66.67$ Hz). (c) and (e) are magnitude response of the signal vs. time and frequency, respectively, and (d) and (f) are the phase responses showing phases after correction for the excitation RF phase. The blue and red lines in temporal plots (c) and (d) correspond to two isochromats at off-resonance -33.33 Hz and -32.67 Hz, respectively. It can be seen that an off-resonance amount of less than $1/T_{OSSI}$ lead to some modest changes in the shape of the response. The green curve in (e) and (f) are the magnitude and phase of the frequency response, respectively, and indicate the manifold on which the steady-state response exists. The blue and red lines connect 6.67 Hz apart samples of the manifold and start from off-resonance -33.33 Hz and -32.67 Hz respectively. Particularly, by comparing (c) and (e), (d) and (f), it is clearly shown that the time and samples of frequency responses have exactly the same shape, only flipped.

2.2.2 OSSI Spin Behavior and Signal Simulation

OSSI spin behavior was examined using a Bloch equation simulator for spins having relaxation parameters similar to gray matter using the average of reported values [36] $T_1 = 1433.2$ ms and $T_2 = 92.6$ ms at 3T, and pulse sequence parameters TR = 15 ms with an excitation pulse length of 3.2 ms, number in phase cycle (n_c) = 10, and flip angle (FA) = 10°. The phase progression with $n_c = 10$ is equivalent to a spoiling seed of 36° for spoiled-GRE. An example of magnetization progression at steady state is shown for a spin with off-resonance -20 Hz in Fig. 2.1, with the pattern repeating every n_c TRs. The signal intensity varies as magnetization moves towards and away from the center in (a), and the spin moves up and down in m_z (b). From Fig. 2.1 (c), we can see that the magnitude of the OSSI signal right after the excitation at TE = 1.6 ms has a periodicity of n_cTR and is substantially larger than the spoiled GRE signal for the same parameters. Observe that off-resonance shifts of multiples of $1/\mathrm{T_{OSSI}} = 1/(n_c\mathrm{TR}) = 6.67$ Hz lead to exactly the same temporal waveform with a shift of 1 TR in time. The isochromats in Fig. 2.1 (c) and (d) cover a frequency range of 13.3 Hz and result in a 74.1° phase spread for the time point right after the RF pulse. Note that the phase between isochromats increases during the readout, which indicates increased T_2'-weighting, and there is no spin-echo signal formed at the center of readout, demonstrating a very different contrast mechanism compared to bSSFP. The observed phase accumulation is equivalent to a T_2'-weighting with an effective TE of 15.4 ms at beginning and 27.2 ms at the end of the readout interval, respectively.

Fig. 2.2 (a) and (b) shows the magnitude and phase responses, respectively, as a function of time and frequency. In Fig. 2.2 (c) and (d), one can see that frequency shifts that are not multiples of $1/\mathrm{T_{OSSI}}$ lead to slightly different time courses in magnitude and phase. The duality between time and frequency is shown in Fig. 2.2 (e) and (f). Here one can see that samples in frequency spaced at integer multiples of $1/\mathrm{T_{OSSI}}$ will give exactly the same waveform as the time courses in Fig. 2.2 (c) and (d), but reversed. More specifically, the OSSI signal M_T and the frequency response M_F have the following relationship

$$M_T(k \bmod n_c; f_0) = M_F\left(f_0 + \frac{1 - k \bmod n_c}{n_c\mathrm{TR}}\right), \tag{2.3}$$

where k is the TR number, and f_0 denotes the off-resonance frequency. From this

expression, one can clearly see that the steady-state frequency response is the manifold on which the time-course signals are found.

2.2.3 Acquisition Parameter Optimization

In seeking to optimize the OSSI signal, there are a variety of measures of goodness. First, since we are interested in applying this method to functional MRI, we wish to maximize sensitivity to changes in the signal resulting from changes in T_2', normalized by the square root of imaging time. It is desirable to have smaller n_c as fewer TRs are needed to complete a single image, while longer TRs are preferred because they allow a longer time for acquisition. We also desire to maximize uniformity of the RMS combined OSSI signal as a function of frequency shifts smaller than $1/\mathrm{T_{OSSI}}$.

To understand the impact of pulse sequence parameters on the OSSI signal, additional Bloch simulations were carried out. Fig. 2.3 (a) shows the RMS combined signal intensity for OSSI as a function of n_c and flip angle for TR = 15 ms. Note that $n_c = 1$ corresponds to bSSFP, and for $n_c > 120$, the OSSI signal behaves similarly to bSSFP with a flat phase response (spin-echo-like contrast) over some range of off-resonance frequencies [34]. However, the bright signals in the upper left corner, bounded by the box, were somewhat unexpected and are the focus of this chapter. Here, we examine a range of parameters with respect to sensitivity for fMRI studies and to undesired sources of signal variation. Deoxygenation of blood at 3T primarily affects T_2' in tissue [37] and causes an approximately exponential decay $\exp(-t/T_2')$ of the BOLD signal. This effect can be modeled by averaging complex signals from a large number of spins with different off-resonance frequencies. When the number of spins is sufficiently large, there exists a Fourier relationship between $\exp(-|t|/T_2')$ and the probability density function of off-resonance frequency f, yielding the Cauchy distribution $G(f) = \gamma/(\pi(\gamma^2 + f^2))$, where γ is the scale parameter of the distribution and $T_2' = 1/(2\pi\gamma)$.

Therefore, to simulate the T_2^*-weighted signal of a voxel in the static dephasing regime, we generated complex OSSI signals from 2000 spins with off-resonance frequencies uniformly ranging from -150 Hz to 150 Hz, and calculated weighted sum of the complex signals. The weighting function is the Cauchy distribution $G(f)$ centered at a specific off-resonance frequency and using $T_2' = 148.3$ ms and 135.5 ms, corresponding to T_2^* of 57 ms and 55 ms given an underlying $T_2 = 92.6$ ms for gray matter, which were selected to model baseline and active conditions, respectively. The T_2^*

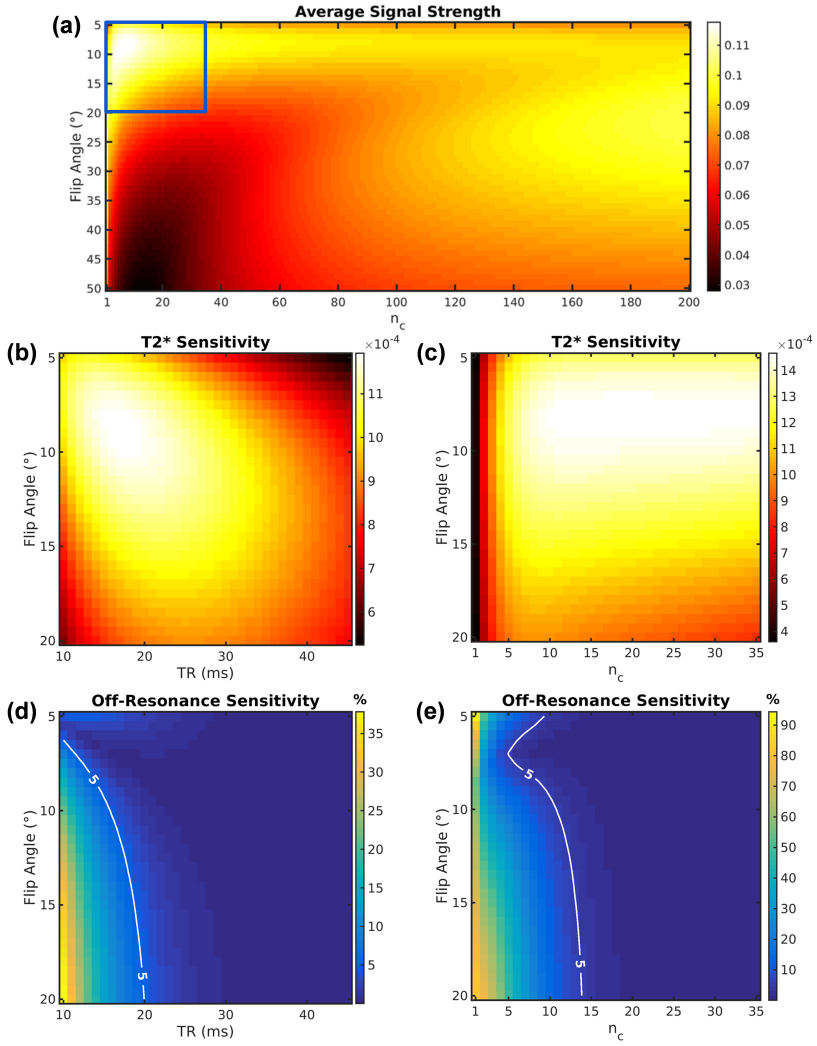

Figure 2.3: Simulation of acquisition parameters for spiral-out readouts (TE = 1.6 ms). (a) to (c) are T_2^* sensitivity defined as $\mathrm{S_{activated}} - \mathrm{S_{rest}}$ in units of $M_0 = 1$. (a) shows the RMS combined magnitude signal as a function of n_c and flip angle for a fixed TR of 15 ms. Notice the bright spot around $n_c = 10$ and flip angle = 10°. We focus on the region denoted by the blue square for OSSI fMRI acquisition parameter optimization, and the results are in (b) to (e). (b) shows how T_2^* sensitivity varies with TR and flip angle for a fixed $n_c = 10$. The signal is normalized by $\sqrt{(\mathrm{TR} - c)/\mathrm{TR}} \approx \sqrt{\mathrm{T_{A/D}}}$ with $c = 5$ ms for SNR efficiency. (c) shows how T_2^* sensitivity varies with n_c and flip angle for TR = 15 ms. (d) gives off-resonance sensitivity at different TR and flip angles for $n_c = 10$. (e) gives off-resonance sensitivity at different n_c and flip angles for TR = 15 ms.

difference represents a typical 1.9% signal change for a T_2^*-weighted GRE image with TE = 30 ms. The OSSI baseline and active signals were obtained by applying RMS combination to every $n_c = 10$ consecutive and non-overlapping time points of the T_2^*-weighted signals.

The OSSI signal of each spin was simulated using a range of parameters for TR, FA, and n_c. We varied two parameters while fixing the third parameter, and performed the simulation for at least 5 T_1s to ensure the signal was in steady state. The T_2^* sensitivity is defined by the difference of the active ($T_2^* = 55$ ms) and baseline ($T_2^* = 57$ ms) signals in units of M_0 either just after the RF pulse for spiral out acquisitions or just before the subsequent RF pulse for spiral-in acquisition. Fig. 2.3 (b) and (c) gives the T_2^* sensitivity for a spiral-out acquisition (TE = 1.6 ms) as a function of different TRs and flip angles for $n_c = 10$, and different n_c and flip angles at a fixed TR of 15 ms, respectively. Supporting Information Fig. 2.10 (b) and (c) presents the same relationship for a spiral-in acquisition (TE = TR - 1.6 ms).

As noted above and shown in Fig. 2.2, the OSSI pulse sequence is very frequency sensitive but for the use in fMRI an important question is the sensitivity of the combined (RMS over n_c points) signal vs. frequency. An example of this effect is the small difference between RMS combined signal of blue and red lines in Fig. 2.2 (c). The combined signal is periodic in the frequency domain with $1/\mathrm{T_{OSSI}} = 1/(n_c\mathrm{TR})$, so we varied the central frequency offset over this range to obtain the signal variability due to field inhomogeneity. The variability was calculated by taking the maximum difference of the combined signals at different central frequencies. Fig. 2.3 (d) and (e) give the frequency-dependent signal variability for the spiral-out acquisition as a function of different TRs and flip angles for $n_c = 10$, and different n_c and flip angles at a fixed TR of 15 ms, respectively. Supporting Information Fig. 2.10 (d) and (e) shows the same relationship for a spiral-in acquisition. Note that the small central frequency dependent variations were averaged across $1/\mathrm{T_{OSSI}}$ for Fig. 2.3 (a)-(c). To assess the T_2^*-weighting of OSSI in comparison to GRE using as long of a TE as possible (equivalent to a spiral-in acquisition), we plot the maximal T_2^*-weighted signal change vs. TR in the Supporting Information, Fig. 2.11.

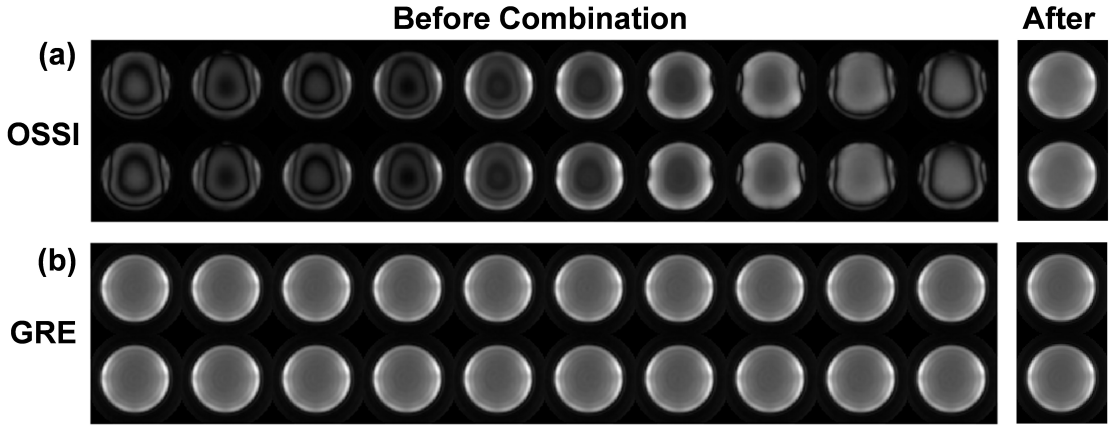

Figure 2.4: Images of steady state with quadratic phase progression ($n_c = 10$) with (a) balance gradients (OSSI) and (b) spoiling gradients (GRE). Each panel has 10 images across the periodic phase pattern and is shown twice to demonstrate the reproducibility. The 2-norm combined images are given on the right. The OSSI and GRE images are not on the same intensity scale.

2.3 Methods

All the studies were performed on a 3T GE MR750 scanner (GE Healthcare, Waukesha, WI) with a 32-channel head coil (Nova Medical, Wilmington, MA). We implemented the OSSI pulse sequence using the vendor's standard pulse programming language, EPIC, and collected data with matched spatial and temporal resolutions using both OSS and GRE approaches.

2.3.1 Phantom Experiments

To demonstrate the principles of OSSI, we collected images of the FBIRN phantom [38] (approximate $T_1/T_2 = 530/60$ ms) using both balanced and spoiled gradients. An oblique slice with FOV = 220 mm and slice thickness = 2.5 mm was acquired, and the voxel size = $6.29 \times 6.29 \times 2.5$ mm^3. For OSSI, we chose TR = 15 ms, $n_c = 10$, FA = 10°, and a fully sampled single-shot spiral-out trajectory. The spoiled-GRE data were acquired with the same parameters, except for the addition of spoiling gradients and the use of a spiral-in readout to make the effective TEs of the two acquisitions more similar. Specifically, the OSSI spiral-out TE = 2.7 ms, which corresponds to an effective TE of 17.5 ms. To bring GRE TE closer to OSSI effective TE and to increase GRE T_2^*-sensitivity with the limited TR = 15 ms, we used GRE spiral-in TE

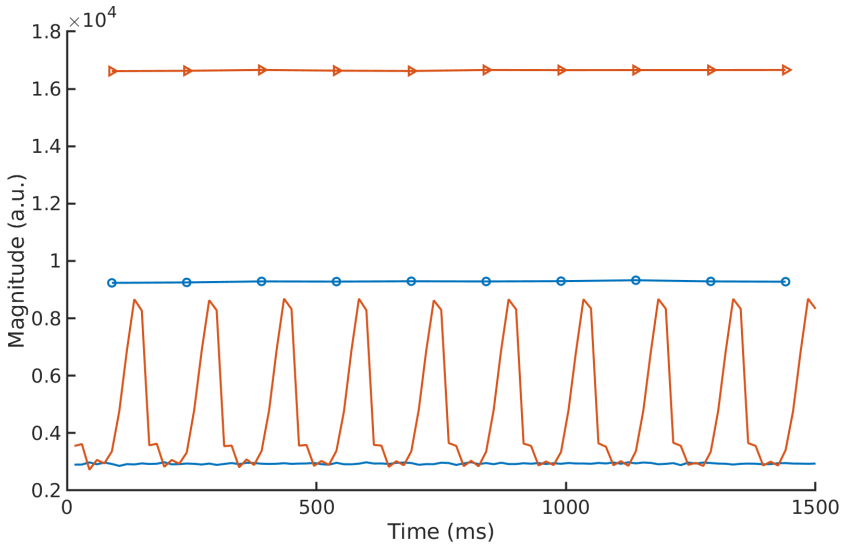

Figure 2.5: Time courses for a 4-voxel ROI in the phantom for OSSI (red) and GRE (blue). Both before and after 2-norm combination, OSSI shows signal strengths roughly two times larger than the spoiled GRE signal.

= 11.2 ms. The number of time points = 100 with 10 s discarded acquisition prior to collecting data. Every $n_c = 10$ images (1 period of the oscillations) were combined pixel-wise using the 2-norm.

2.3.2 Human Experiments

2.3.2.1 2D Human Studies

Human functional imaging studies were performed on 5 subjects using both OSSI and GRE methods with informed consent and IRB approval. The functional task was a left vs. right reversing-checkerboard visual stimulus (with 5 cycles of 20 s L/20 s R). The 2D sampling pattern for both GRE and OSSI was multi-shot (number of interleaves $n_i = 8$) fully sampled variable-density spirals with a densely sampled core (300 k-space points). A single oblique slice through visual cortex was selected with FOV = 220 mm and 2.5 mm slice thickness. The voxel size was 1.77 × 1.77 × 2.5 mm^3 (matrix size 124 × 124). All the 2D images were reconstructed as 128 × 128 matrices. The experiments include 4 spiral-out acquisitions of 4 subjects and 4 spiral-in acquisitions of 4 subjects.

For the OSSI method, we chose TR = 15 ms, $n_c = 10$, and nominal FA = 10°. The OSSI effective TR for each spiral = 150 ms (TR · n_c) and the volume TR =

1.2 s ($TR \cdot n_c \cdot n_i$). For the GRE acquisition, we carefully matched spatial-temporal resolution of OSSI, each interleave was acquired with GRE TR = 150 ms, volume TR = 1.2 s ($TR \cdot n_i$), and the Ernst flip angle FA = 27° to optimize SNR. The number of time points for OSSI was 1670 or 167 combined images, and the number of time points for GRE was 167 with no combination necessary, corresponding to the 200 s of the functional task. To establish the steady state, no data were collected for the first 10 s for both acquisitions. OSSI actual TE was set to minimum (TE = 2.7 ms) for spiral-out imaging and TE = 11.6 ms for the spiral-in case. Recognizing that the OSSI acquisition has some inherent T_2^*-weighting with spiral-out effective TE = 17.5 ms and spiral-in effective TE = 27.5 ms according to the simulations, we used slightly varying GRE TEs for different experiments to get an robust real data estimation of OSSI effective TE. For the 4 spiral-out experiments, we selected GRE TE = 17.5, 20, 20, and 23 ms, and for the 4 spiral-in experiments, we selected GRE TE = 27.5, 30, 30, and 33 ms.

Additionally, a T_1-weighted image was acquired for each subject and used to create a mask for the brain regions using the Brain Extraction Tool [39].

2.3.2.2 3D Human Studies

As an anecdotal demonstration, we acquired a 3D data set for a single human subject. The functional study was the same visual stimulus as in 2D studies (5 cycles of 20s on/20s off). An oblique 12-slice 3D volume was acquired using a stack of single-shot spirals with spiral-out readouts. The matrix size = 64 × 64 × 12, and the voxel size = 3.44 × 3.44 × 3 mm^3. For 3D OSSI imaging, TR = 15 ms, $n_c = 10$, FA = 10°, TE = 2.2 ms for each slice, and the volume TR = 1.8 s ($TR \cdot n_c \cdot n_z$). The spiral sampling trajectory in the k_x-k_y plane was a variable-density spiral with a linearly decreasing sampling density, leading to a factor of 3 undersampling. Along the k_z direction, the spirals were rotated 45° for each spiral platter to reduce undersampling artifacts. For the GRE imaging, the 12 slices were collected using a 2D spiral-out sequence with fully sampled uniform-density spirals, GRE TR = 1.8 s, TE = 23 ms to approximately match OSSI effective TE, and FA = 75°. The number of volumes = 112 for both OSSI (after 2-norm combination) and GRE, for a total about 200 s of acquisition, which followed 10 s of discarded acquisition used to establish the steady state.

We also acquired 2D multi-slice images using a standard spin-warp acquisition for

generating SENSE maps. The 32-channel coil images were compressed to 28 virtual coils, and the SENSE maps were generated using ESPIRiT [40, 41]. The 3D OSSI images were reconstructed from the undersampled measurements using the conjugate gradient SENSE [42, 43], with an edge-preserving regularizer implemented through [44]. The fully sampled GRE data were reconstructed using the gridding method.

2.3.3 Data Analysis

As mentioned above, every $n_c = 10$ consecutive and non-overlapping OSSI images were combined by taking the 2-norm. Functional imaging performance was evaluated for both OSSI and GRE BOLD by evaluating activation maps and the temporal SNR (tSNR). The data from the first cycle (40 s) of the task were discarded to avoid the modeling error in the initial rest period. To reduce the effects of scanner drift, detrending was applied using lower order discrete cosine transform bases. The correlation coefficients were determined by correlation with a reference waveform, and the activated regions were defined by the magnitude of the correlation coefficients larger than a 0.5 threshold. The reference waveform was generated by convolving the canonical hemodynamic response function [45] with the task. The number of activated voxels were counted at the bottom third of the brain, where the primary visual cortex is located. The tSNR maps were calculated by dividing the mean of the time course by the standard deviation of the time course residual (after removing the mean and the task) for each voxel. We calculated the average tSNR over the whole brain over an ROI limited to the brain region and excluding the skull and scalp.

To determine the effective TE of OSSI, we generated scatter plots based on the percent signal change for voxels that were active in both GRE and OSSI acquisitions. In GRE, the percent signal change is approximately equal to $\Delta R_2' \cdot \mathrm{TE}$ [46]. By establishing the relationship between OSSI and GRE percent change and under the assumption that activation change ($\Delta R_2'$) is the same in both cases, we can estimate the effective TE for OSSI using $\mathrm{TE}_{\mathrm{eff}} = b \cdot \mathrm{TE}_{\mathrm{GRE}}$ when the percent changes of OSSI and GRE are highly correlated, where b is the slope of the OSSI-GRE percent change relationship. Due to variability in both data sets, we performed a model II fit with standardized major axis (SMA) regression and 0 intercept to estimate the slope of the relationship for each experiment. Voxels with a percent change greater than 4% in either method, which likely represent vascular signals, were found to be highly variable and were excluded from the regression. In addition, the linearity of

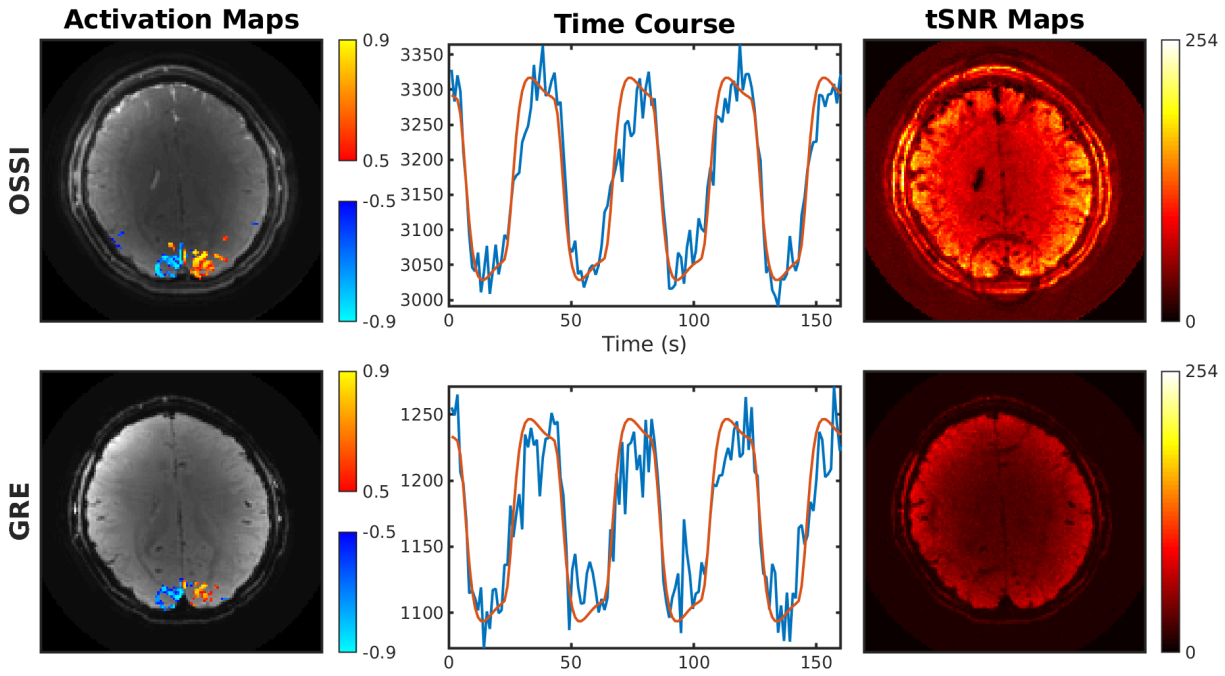

Figure 2.6: OSSI and GRE functional results from multi-shot spiral-out acquisition with OSSI TE = 2.7 ms and GRE TE = 23 ms. At left, the activation map uses a threshold of 0.5 for the correlation with a reference waveform, and the background is the mean image of the OSSI combined or GRE images. The time course for a 4-voxel ROI is shown for each method together with the reference waveform (intensity units are arbitrary signal units). At right, the temporal SNR maps are also shown for both methods.

the relationship between OSSI and GRE percent signal changes was assessed using Pearson's correlation coefficient.

2.4 Results

The phantom images in Fig. 2.4 (a) present the evolution of the oscillation pattern for OSSI over the $n_c = 10$ phase cycles and show the highly reproducible nature of the oscillations. Note that magnetic field inhomogeneity leads to an inhomogeneous spatial pattern in the OSSI data, and that different isochromats have different temporal patterns. Fig. 2.4 (b) shows the same slice with spoiled gradients. Although the spoiled steady-state images are free of oscillations, their magnitudes are much lower. The 2-norm combination of every non-overlapping $n_c = 10$ OSSI images produces spatially and temporally uniform signals. The time courses in Fig. 2.5 show oscillating

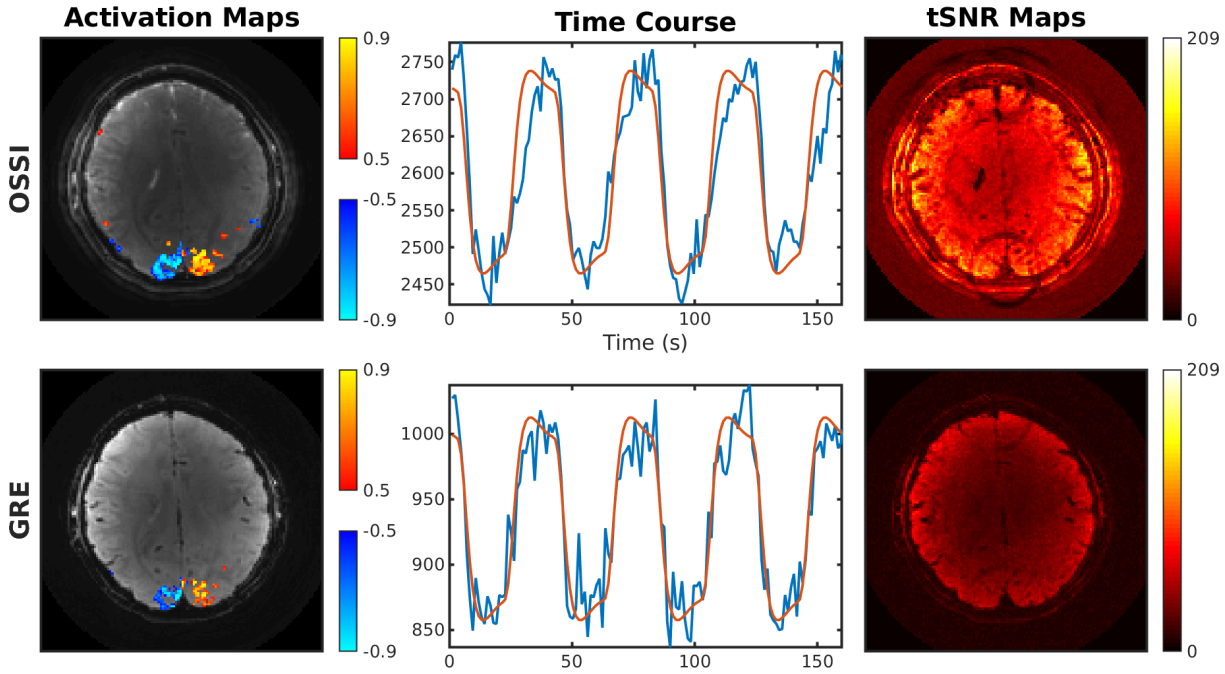

Figure 2.7: OSSI and GRE functional results from multi-shot spiral-in acquisition with OSSI TE = 11.6 ms and GRE TE = 33 ms. The activation map uses a threshold of 0.5 for the correlation with a reference waveform, and the time course for a 4-voxel ROI is shown with the reference waveform for each method (intensity units are arbitrary signal units). The temporal SNR maps are also shown for both OSSI and GRE acquisitions. Compared to the spiral-out results in Fig. 2.6, we can see that spiral-in gives more activations, but relatively lower signal strength and temporal SNR for both OSSI and GRE.

steady-state signal and the stable signal after the 2-norm combination. In comparison to spoiled GRE with matched resolutions and TE, the OSSI signal strength was roughly 2 times larger than the spoiled signal, though the exact relationship is highly dependent on phantom/tissue T_1s and T_2s.

Fig. 2.6 gives 2D human spiral-out activation maps, time courses, and tSNR maps for visual stimulation. Compared to GRE with matched acquisition characteristics and TE, the OSSI result shows more activations according to the activation maps, a larger task-related signal change as in the time course, and higher tSNR presented by the tSNR maps. The OSSI signals appear localized more in parenchyma with less signal from the sulci and vascular regions near the sagittal sinus.

Fig. 2.7 shows 2D human spiral-in functional results and tSNR maps. The OSSI acquisition results in larger activation regions and much higher tSNR in comparison

to GRE. Though anecdotal, the time course of OSSI appears to be less noisy. The spiral-in scheme uses a closer to optimal TE for fMRI (at 3T, a common choice is TE = 30 ms), thereby leading to more activations for both OSSI and GRE compared to the spiral-out results in Fig. 2.6 in spite of the overall lower signal intensity and tSNR.

Fig. 2.8 shows OSSI and GRE percent signal change scatter plots for spiral-out data of Fig. 2.6 and spiral-in data of Fig. 2.7, and the slope of the scatter plots depicts the relationships between OSSI effective TE and GRE TE. The slope resulted from the SMA regression is 0.73 for spiral-out and 0.82 for spiral-in. As described in Methods, we can calculate the effective TE for OSSI as spiral-out OSSI TE_{eff} = 16.7 ms, and spiral-in OSSI TE_{eff} = 27.1 ms for this subject. Scatter plots for the other subjects can be found in the Supporting Information, Fig. 2.16. The mean OSSI TE effective across all the subjects is 17.8 ms for spiral-out, and is 27.1 ms for spiral-in, given the actual TE's of 2.7 ms and 11.6 ms, respectively, which correspond to an effective T_2'-weighting of about 15 ms at the time of the excitation pulse for both spiral-out and spiral-in cases. The average correlation coefficient between OSSI and GRE across all subjects was 0.5, and linearity of the relationship was found to be significant ($p < 0.05$) for all data sets. The high correlation of OSSI and GRE percent signals in the common activated regions is consistent with a similar contrast mechanism for OSSI and GRE acquisitions.

Quantitative measurements for all visual fMRI experiments including number of activated voxels (at the bottom third of the brain) and average tSNR of the whole brain are given in Table 2.1. OSSI shows a 1.84 ratio (s.d. = 0.5) of number of activation voxels in comparison to GRE with matched spatial-temporal resolutions and similar effective TEs. The tSNR ratio of OSSI to GRE has a mean of 1.83 (s.d. = 0.19). tSNR values were compared using a paired t-test, and OSSI was found to be significantly higher ($p < 0.05$). The columns in Table 2.1 directly corresponds to the columns in Supporting Information Fig. 2.13, which presents activation maps and tSNR maps for the 5 subjects. For each subject and GRE TE ranging from 17.5 ms to 33 ms, the OSSI acquisition provides larger activation regions and higher tSNR than GRE. Subject 2 demonstrated motion artifacts, which led to lower tSNR ratios, artifacts in the tSNR maps, and some false positive activations (near the edge of the brain). The circular spatial variation in tSNR maps are believe to result from pulsatile flow at ventricles and vessels in combination with the multi-shot (8-shot) acquisition.

Table 2.1: Quantitative results including number of activated voxels and average tSNR.

		Spiral-Out				**Spiral-In**				
Subject ID		1	2	3	4	1	2	3	5	Mean (SD)
# Activated Voxels	OSSI	215	159	210	84	264	165	236	123	182
	GRE	133	113	116	55	151	84	144	41	105
	Ratio	1.62	1.41	1.81	1.53	1.75	1.96	1.64	3.0	1.84 (0.5)
Average tSNR	OSSI	85.1	55.1	74.7	68.2	71.4	47.2	60.6	47.9	63.8
	GRE	40.9	34.9	41.9	37.8	34.6	29.5	34.1	24.7	34.8
	Ratio	2.08	1.58	1.78	1.80	2.06	1.60	1.78	1.94	1.83 (0.19)

OSSI, oscillating steady-state imaging; GRE, gradient echo imaging; tSNR, temporal signal-to-noise ratio.

When averaging tSNR over an ROI that is away from artifacts, the tSNR ratio of OSSI to GRE is generally greater than 2.

Fig. 2.9 is a preliminary demonstration of 3D activation results in visual cortex. OSSI and GRE acquisitions give comparable activation maps even through the OSSI data were undersampled. For OSSI, the number of activated voxels = 705 and the average tSNR = 57.2. For GRE, the number of activated voxels = 883 and the average tSNR = 62.4.

2.5 Discussion

This chapter describes a fundamentally new approach to fMRI acquisition that uses a novel oscillating steady-state source of signal that is very large and also sensitive to the blood oxygenation, thereby offering the potential for high SNR fMRI. The proposed quadratic phase progression in conjunction with balanced gradients produces this new steady state. As with other steady-state imaging methods, the OSSI method has large signals because it reuses rather than spoils the magnetization. The oscillating steady-state signals available prior to gradient dephasing contain typically more than twice the average signal amplitude of spoiled signals. We have also noted that this pulse sequence with its quadratic phase sequence is very sensitive to off-resonance. Indeed, a frequency dependent phase dispersal is important for generating the T_2'- or T_2^*-contrast that makes it suitable for fMRI. In our experiments, we found T_2'-weighting of approximately 15 ms at the time of excitation pulse. Additional T_2' weighting can be obtained with increased TE as shown in Supporting Information

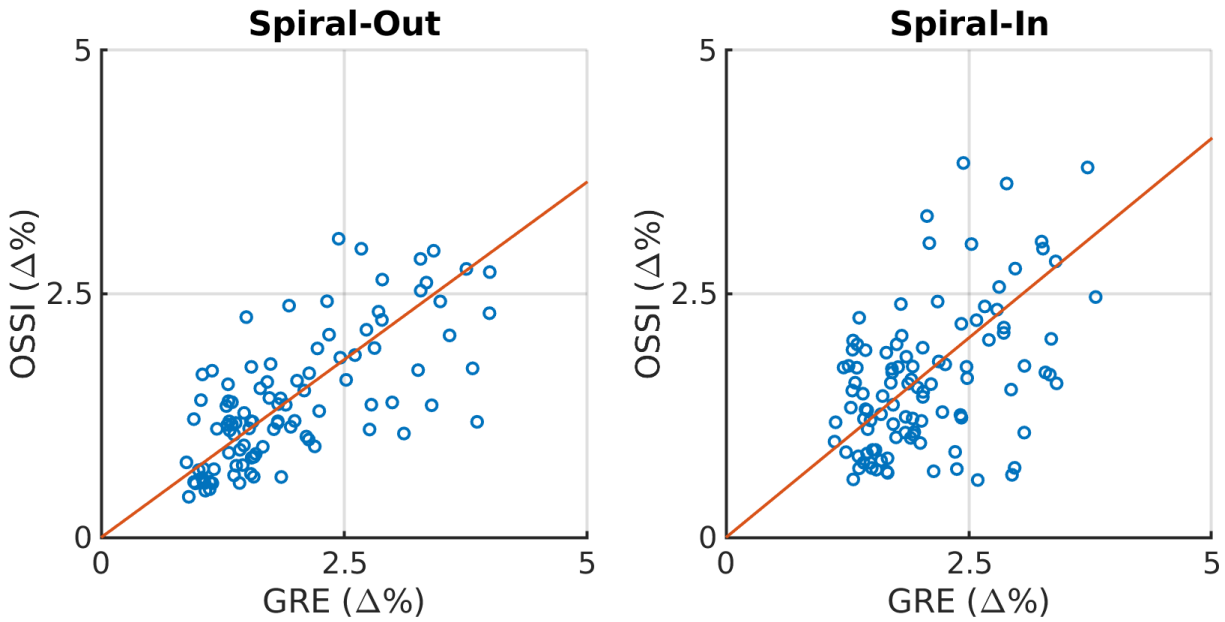

Figure 2.8: Percent signal change of OSSI vs. GRE for active voxels in Fig. 2.6 and Fig. 2.7 where the percentage signal change was below 4% in both methods (spiral out TEs: OSSI = 2.7 ms, GRE = 23 ms; spiral in: OSSI = 11.6 ms, GRE = 33 ms). These figures demonstrate a high correlation between the methods, indicating the potential utility of OSSI as an alternative to GRE fMRI. The slope of the line was fit via Model II regression.

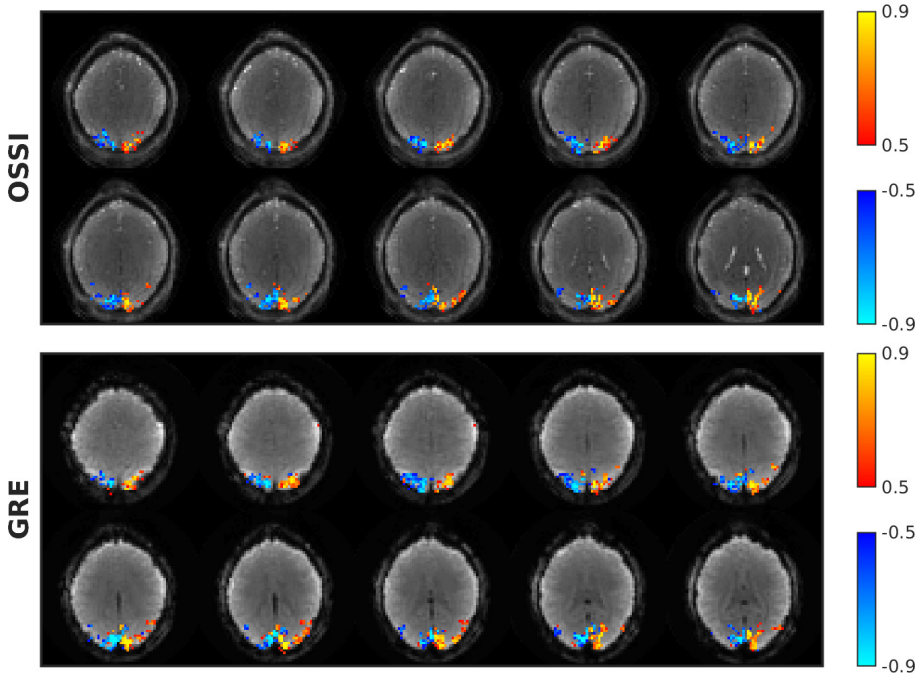

Figure 2.9: Functional MRI of 10 slices drawn from volumetric 3D OSSI acquisition (volume TR = 1.8 s, TE = 2.2 ms, matrix size = 64 through undersampling in-plane) and 2D multi-slice GRE (TR = 1.8 s, TE = 23 ms, matrix size = 64) showing similar activation patterns in visual cortex.

Fig. 2.12.

OSSI signals oscillate with a periodicity of n_cTR, however, the oscillations are highly reproducible, and by combining n_c time points generates stable time courses required for fMRI analysis. As demonstrated in the high-resolution visual stimulation fMRI study, the OSSI approach improves tSNR by about 83% and the number of activated voxels was increased by about 84%, both relative to GRE imaging at the Ernst angle with the carefully matched spatial-temporal acquisition characteristics and effective TEs. The 2D human fMRI experiments used relatively high spatial resolution and thus were closer to thermal noise limit. The same data were subjected to low spatial resolution reconstructions with the results shown in the Supporting Information, Fig. 2.19 and Table 2.2. While the OSSI data still had SNR advantages, the SNR gain of OSSI was reduced relative to the high-resolution and more thermal noise limited cases. Similarly for the anecdotal low-resolution 3D human data that was likely to be physiological noise limited and for the low-resolution phantom data that is systematical noise limited [47], the SNR advantage is compromised.

Because we acquired GRE with a longer TE, there is a possible concern that the longer TR might alter temporal noise characterstics, so we compared the OSSI method to GRE with a 3× shorter GRE TR. As shown in Supporting Information Fig. 2.20 and Table 2.3, for the experimental conditions used (high spatial resolution, likely thermal noise limited regime), the shorter TR leads to similar functional results and tSNR values as GRE with longer TR. We also considered the possible use of other steady state methods, such as FISP/S1 SSFP and found that while it has more signal than GRE for short TRs, it does not have the increased T_2^* sensitivity of OSSI.

We note that further improvements in performance are possible and in fact, likely. For example, our simulations show that TR = 15 ms, n_c = 10, and FA = 10° is a good combination to get high SNR and functional MRI responses, but it is by no means optimal. The short readouts can limit SNR efficiency, so there are potential advantages to going to longer TRs and longer readouts. As shown in Fig. 2.3 and Supporting Information Fig. 2.10, multiple combinations of imaging parameters give a similar T_2^*-sensitivity and off-resonance sensitivity. There is a complex interplay between these sensitivity measures and the major imaging parameters including TR, n_c, FA, and TE (including TE locations from different readouts, e.g. spiral-out, spiral-in, or EPI with TE in the center). The RF (FA) inhomogeneity in the brain at 3T may influence the actual FA to use when acquiring slices at different parts of

the brain, which further complicates the optimization. We also note that the optimal FA appears to be small in comparison to many bSSFP applicaitons where FAs $> 30^\circ$ are common, which would indicate that RF heating is unlikely to be an issue with OSSI. Curiously, the optimal FAs are often not far from the Ernst angle, e.g. 8.3° for TR = 15 ms. The final optimization will require practical experience regarding which factors are most important for particular fMRI studies.

The sensitivity to frequency as noted above, will lead to substantial physiological noise, and in particular, artifacts and noise from respiration, which is known to lead to oscillations shifts in resonant frequency [48]. Fig. 2.18 presents residual time courses and spectra of OSSI and GRE at a non-active region, and the OSSI spectrum shows a prominent peak near respiration frequencies. We investigated the standard physiological noise removal technique RETROICOR [49] applied to individual temporal phases as well as the combined images, and also k-domain methods (RETROKCOR [50]) applied to individual temporal phases. We found only modest improvements in tSNR and activation maps when applying corrections over limited time windows and no improvements over longer windows [21]. This, we believe, is due to the complex and non-linear nature of the interaction between frequency and the temporal signal (see Fig. 2.2 (c, d), for example). In addition, the use of a 2D slice for the visual study makes it sensitive to inflow and pulsatility artifacts. Physiological noise correction is an active area of research [51] and will be the topic of a future manuscript. As such, no physiological noise corrections for OSSI were applied in the present work, but we believe that after correction, further tSNR and activation improvements close to the increases in signal strength will be possible.

Like most steady-state methods, the short TR largely prevents interleaving of slices, when combined with the time needed to reach steady state, dictates that OSSI methods are best suited to 3D acquisitions. Furthermore, the need to acquire volumetric images for each temporal phase implies that n_c times as many images are required for a study. Fortunately, the reproducible nature of oscillating signal may allow dramatic reductions in the acquisition time. For example, the use of sparse sampling in k-space and modeling of the oscillations using patch-tensor low-rank [52] or a dictionary based regularizer [53] can fully recover the missing data in the image reconstruction process. This again, is a topic of active research, and preliminary results suggest that larger than a 13-fold reduction in k-space is possible with minimal performance degradation. We have anecdotally demonstrated the ability to acquire

3D images, though without acceleration using the spatiotemporal models described here. We note that most 2D acquisitions would include acceleration using 2D simultaneous multi-slice imaging [54, 55], but also note that undersampling in 3D exploits roughly the same parallel imaging concepts [56]. So, we believe that similiar accelerations are possible for OSSI and the use of temporal modeling will help resolve the inefficiency of acquiring n_c images. The slow volume TR reduces temporal resolution, but does not reduce SNR due to averaging of signal and noise across the n_c temporal phases. As pointed out above, the short TR does limit the length of the readout which can reduce the SNR efficiency.

In prior work, bSSFP imaging for fMRI has taken advantage of different phenomena, for example, frequency shifts, changes in T_2 associated with changes in blood oxygenation, or changes due to inhomogeneous effects and diffusion around small vessels [28, 29]. In this work, we argue that the OSSI signal changes are due to more traditional, size-scale invariant changes in T_2^* or T_2' of the tissues, again in response to changes in blood oxygenation. We argue that this sensitivity is due to frequency sensitivity of OSSI signal that leads to frequency-dependent phase variations as shown in the simulations of Fig. 2.1 (d). The percent signal plots in Fig. 2.8 and Fig. 2.16 clearly show a very linear relationship (average p-value for the slope = 0.01 using standard linear regression) of OSSI and GRE percent signal changes, which would be consistent with a similar signal change mechanism between the two methods. We note that further work is necessary to fully elucidate the mechanism, including the effects of diffusion around vessels. The simulation and percent signal change analysis are both consistent with the OSSI signal being inherently T_2^* or T_2' weighted, specifically OSSI leads to an additional T_2'-weighting of approximately 15 ms for the parameters used (TR = 15 ms, $n_c = 10$, FA = 10°).

The analysis of percent change signal in OSSI and GRE excluded voxels with a percent change greater than 4% in at least one of the methods. Above 4%, the signal change for OSSI seemed to flatten and the relationship was no-longer suitable for linear regression. These very high GRE percent changes, which likely represent vascular signals as shown in Fig. 2.17, have had a lower signal change in OSSI perhaps due to flow-related signal changes. If so, this partial suppression of vascular signals could be seen as a desirable feature as it will improve functional localization.

There are a number of unstudied phenomena we wish to address in the future. Long T_2-species like cerebrospinal fluid in the ventricles are very bright in OSSI, but

when combined with cardiac pulsatility lead to low tSNR as seen in the first and third rows of Fig. 2.13. Part of the high variability may arise from the in-flow effects associated with the 2D acquisition and may be partially resolved by 3D imaging. Pulsatile effects and in-flow phenomena with vessels require further investigation. The short TR makes implementation of fat suppression more challenging, however, the relaxation and spectral characteristics of lipids seem to lead to relatively low signal intensity and limited artifacts in the images. Still, the signal characteristics of lipids, as well as the possible use of slab-selective spectral spatial pulses, should be investigated. As with most fMRI studies, detection and bulk correction of head motion will be needed. In this case, we will also need to consider any impact on the steady-state signal due to head motion.

Another interesting question is what occurs in the presence of large magnetic fields gradients near regions of large susceptibility differences in the brain, for example, the orbitofrontal cortex. Such gradients might have a similar impact as applying unbalanced gradients, leading to signal spoiling and a reduction of the additional T_2'-weighting of 15 ms common to OSSI. The signal may gracefully transition to a spoiled GRE signal with relatively short TE. This phenomenon is closely related to partial spoiling described by Ganter [57], except that very small phase increments with large gradients are used in Ganter's paper, while here we have large phase increments between RF pulses but partial gradient spoiling. We are also interested in other possible applications of the OSSI signal. Frequency sensitivity may be useful in applications where frequency tracking is needed, for example, in tracking temperature-dependent frequency changes in therapeutic ultrasound.

2.6 Conclusion

The OSSI approach departs from traditional acquisition approaches by exploiting a novel T_2^*-weighted signal mechanism that produces large steady-state signals, and to our knowledge, has never been used before for fMRI. We show in both simulations and experimental data that the proposed approach has a similar contrast mechanism and percent signal change as GRE and leads to a substantial increase in signal strength and tSNR with matched spatial-temporal resolutions and effective TE, thereby enabling detection of 84% greater volumes of functional activity. The SNR advantages were shown for a specific case of single slice fMRI using a short

TR, and extensions to volumetric acquisition and implementation of physiological noise corrections will be critical for general application. Still, this approach offers the prospect of high-resolution fMRI without the need for higher magnetic field strength systems.

2.7 Supporting Information

The supplemental material presents Oscillating Steady-State Imaging (OSSI) simulation and human data results.

Simulations consist of acquisition parameter optimization for spiral-in readouts, OSSI to GRE T_2^*-sensitivity comparison, and how OSSI T_2^*-weighting changes with increased TE. Human data results include activation maps, tSNR maps, z-maps, histograms of all 8 visual experiments, additional percent signal change plots, maps showing vascular activations, residual time courses, low spatial resolution reconstructions, and comparison to GRE TR = 50 ms.

2.7.1 Simulations

Fig. 2.10 presents spiral-in acquisition parameter optimization results. OSSI to GRE T_2^*-sensitivity comparison as a function of TR is shown in Fig. 2.11. OSSI T_2^*-weighting increases almost linearly with increased TE as given in Fig. 2.12.

2.7.2 Human Data

2.7.2.1 All Visual Experiments

Fig. 2.13 presents activation maps and tSNR maps for all visual fMRI experiments. For each experiment, the OSSI acquisition provides larger activation regions and higher tSNR compared to the standard GRE approach. Fig. 2.14 shows the corresponding z-maps, and Fig. 2.15 histograms compare OSSI and GRE voxel counts over a z-threshold. The relationships between OSSI and GRE percent signal changes of subject 2-5 are in Fig. 2.16. Fig. 2.17 shows the potential vasculature nature for signals where percent signal changes were large and thus excluded from effective TE analysis. Fig. 2.18 contains example residual time courses and spectra averaged over a large ROI away from activations comparing noise patterns of OSSI and GRE.

2.7.2.2 Low Spatial Resolution Reconstructions

Human data shown in Fig. 2.13 were reconstructed with a limited k-space (64/FOV) to obtain images with a lower spatial resolution. The activation maps and tSNR maps in Fig. 2.19 and quantitative measurements in Table 2.2 demonstrates a reduced SNR advantage of OSSI to GRE at lower resolutions.

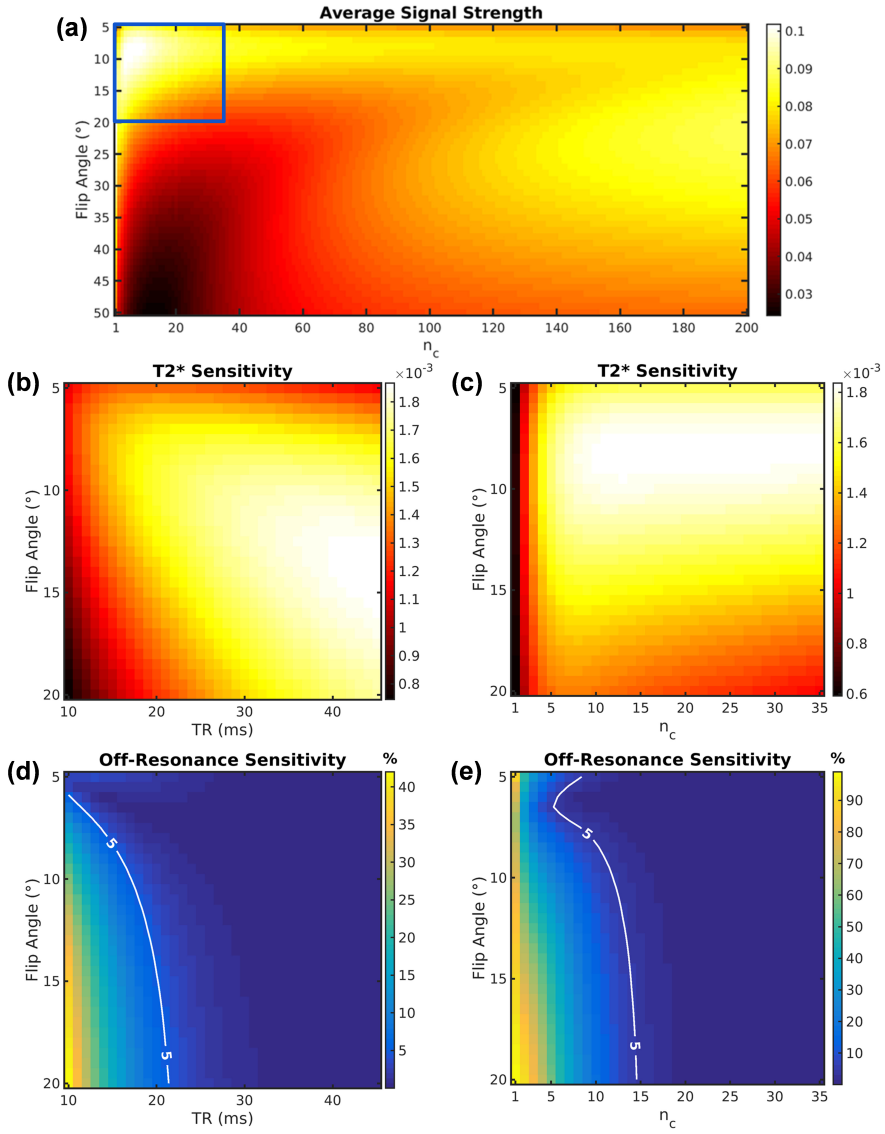

Figure 2.10: Simulation of acquisition parameters for spiral-in readouts (TE = TR - 1.6 ms). (a) to (c) are in units of $M_0 = 1$.
(a) shows the RMS combined magnitude signal as a function of n_c and flip angle for a fixed TR of 15 ms. We focus on the region denoted by the blue square for OSSI fMRI acquisition parameter optimization, and the results are given in (b) to (e). (b) shows how T_2^* sensitivity ($S_{activated} - S_{rest}$) varies with TR and flip angle for a fixed $n_c = 10$. The signal is normalized by $\sqrt{(TR - c)/TR} \approx \sqrt{T_{A/D}}$ with $c = 5$ ms for SNR efficiency. (c) shows how T_2^* sensitivity varies with n_c and flip angle for TR = 15 ms. (d) gives off-resonance sensitivity at different TR and flip angles for $n_c = 10$. (e) gives off-resonance sensitivity at different n_c and flip angles for TR = 15 ms.

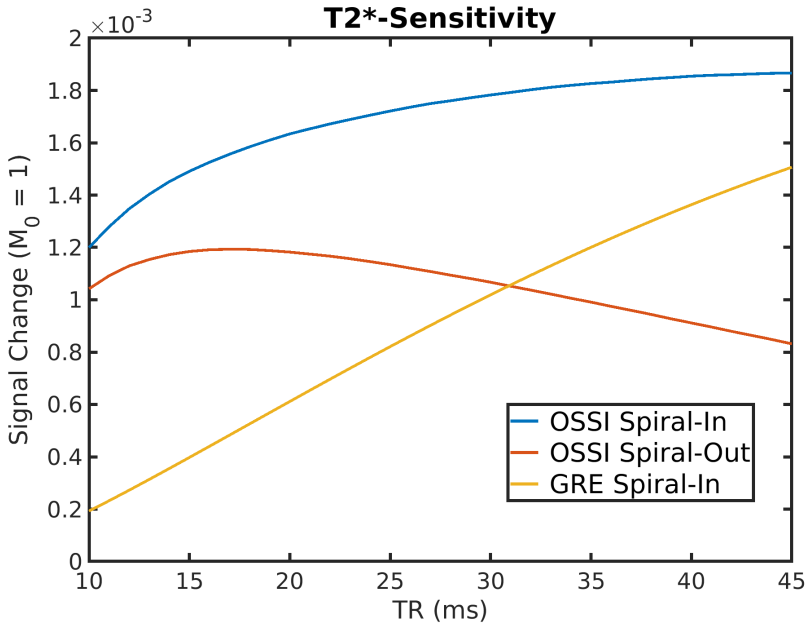

Figure 2.11: T_2^*-sensitivity ($S_{activated}$ – S_{rest} in units of M_0) changes with varying TR for GRE spiral-in (TE = TR - 1.6 ms), OSSI spiral-out (TE = 1.6 ms), and OSSI spiral-in (TE = TR - 1.6 ms). The signals are normalized by $\sqrt{(TR-c)/TR} \approx \sqrt{T_{A/D}}$ with $c = 5$ ms for SNR efficiency and are maximized over flip angle for each method.

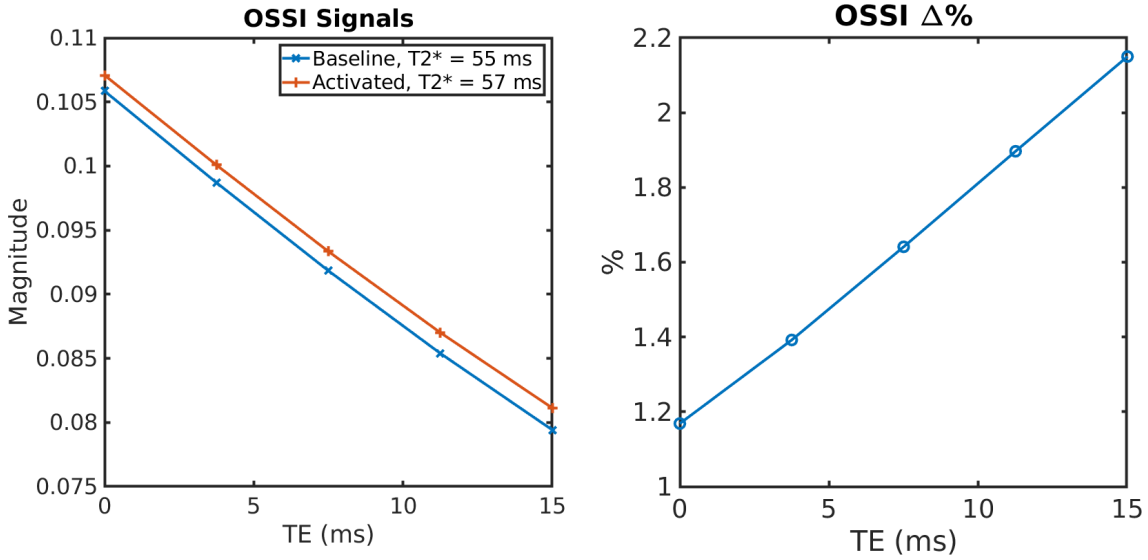

Figure 2.12: Simulated OSSI T_2^*-weighting and percent signal increase almost linearly with increased TE for TR = 15 ms, $n_c = 10$, and flip angle = 10°.

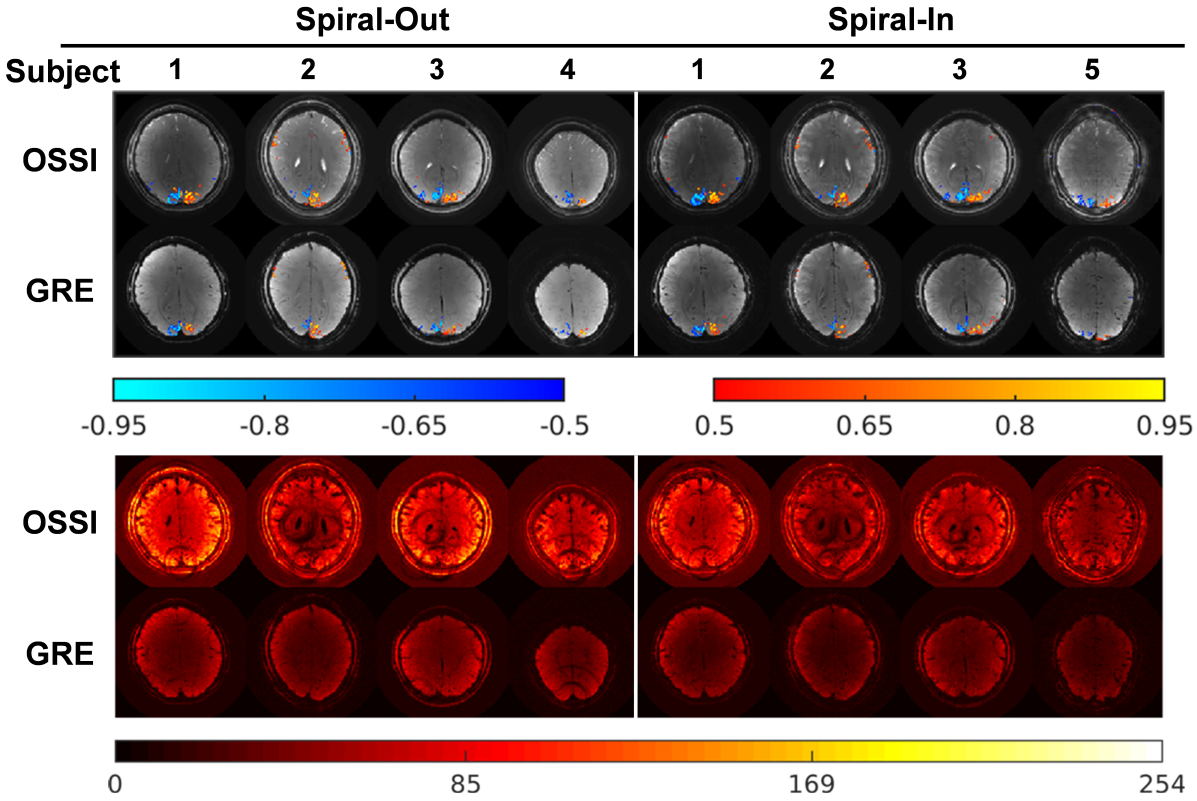

Figure 2.13: Comparison of OSSI and GRE activation maps and tSNR maps for all 5 subjects.

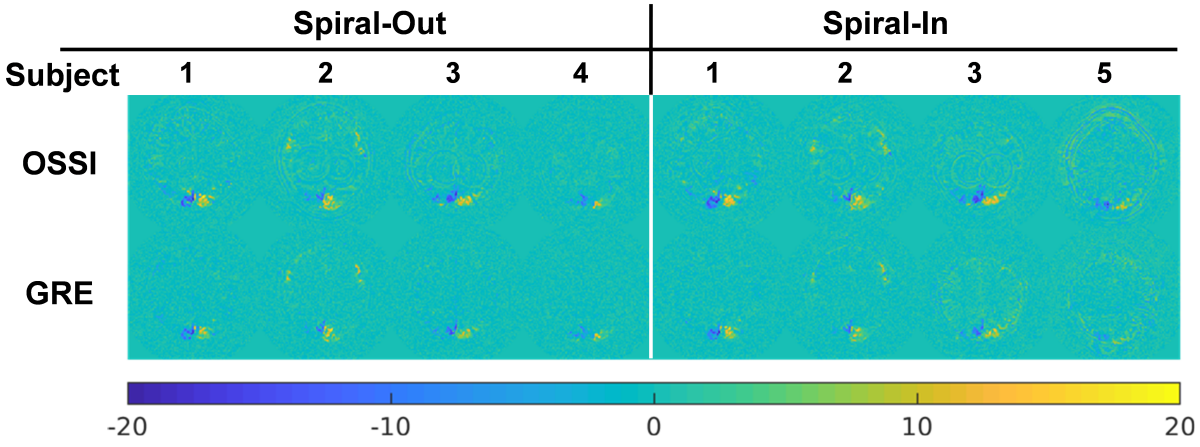

Figure 2.14: Z-maps of all the experiments.

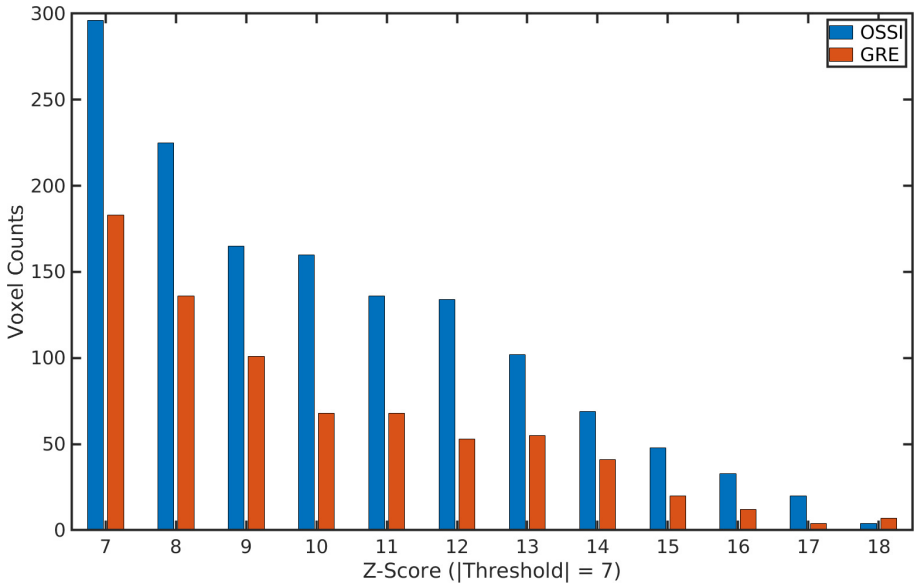

Figure 2.15: Histograms of voxel counts over z-score threshold = ±7, which corresponds to correlation = ±0.5 for the GRE TR = 150 ms case.

Table 2.2: Quantitative results including number of activated voxels and average tSNR from low spatial resolution reconstructions.

Low-Resolution		**Spiral-Out**				**Spiral-In**				
Subject ID		1	2	3	4	1	2	3	5	Mean (SD)
# Activated Voxels	OSSI	124	90	118	51	129	97	134	98	105
	GRE	89	62	88	53	92	72	116	97	84
	Ratio	1.39	1.45	1.34	0.96	1.40	1.35	1.16	1.01	1.26 (0.19)
Average tSNR	OSSI	138.3	78.9	118.1	94.9	109.9	66.4	88.9	65.6	95.1
	GRE	68.7	60.6	72.6	60.0	58.0	50.8	55.9	36.2	57.8
	Ratio	2.01	1.3	1.63	1.58	1.89	1.31	1.59	1.81	1.64 (0.26)

OSSI, oscillating steady-state imaging; GRE, gradient echo imaging; tSNR, temporal signal-to-noise ratio.

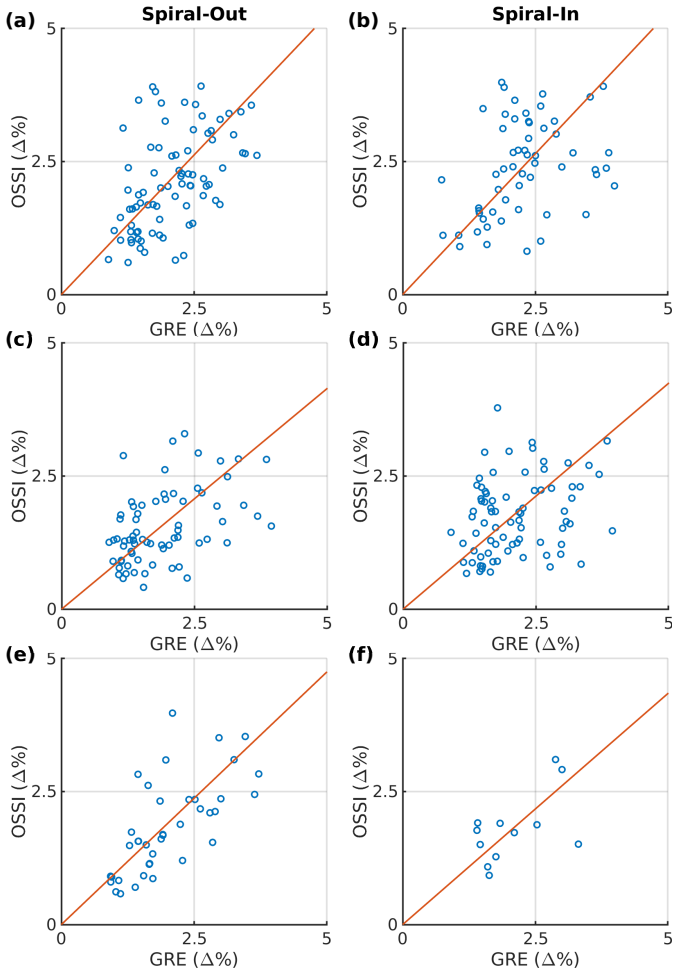

Figure 2.16: Percent signal change of OSSI vs. GRE for active voxels for subjects 2-5 where the percentage signal change was below 4% in both methods. Actual OSSI TE is 2.7 ms for spiral-out and is 11.6 ms for spiral-in.
These figures demonstrate a high correlation between the methods, indicating the potential utility of OSSI as an alternative to GRE fMRI. The slope of the line was fit via Model II regression.
(a) subject 2 spiral-out acquisition, GRE TE = 20 ms, slope = 1.05, and OSSI TE_{eff} = 21 ms.
(b) subject 2 spiral-in acquisition, GRE TE = 30 ms, slope = 1.06, and OSSI TE_{eff} = 31.7 ms.
(c) subject 3 spiral-out acquisition, GRE TE = 17.5 ms, slope = 0.83, and OSSI TE_{eff} = 14.5 ms.
(d) subject 3 spiral-in acquisition, GRE TE = 27.5 ms, slope = 0.85, and OSSI TE_{eff} = 23.2 ms.
(e) subject 4 spiral-out acquisition, GRE TE = 20 ms, slope = 0.95, and OSSI TE_{eff} = 19 ms.
(f) subject 5 spiral-in acquisition, GRE TE = 30 ms, slope = 0.87, and OSSI TE_{eff} = 26.2 ms.

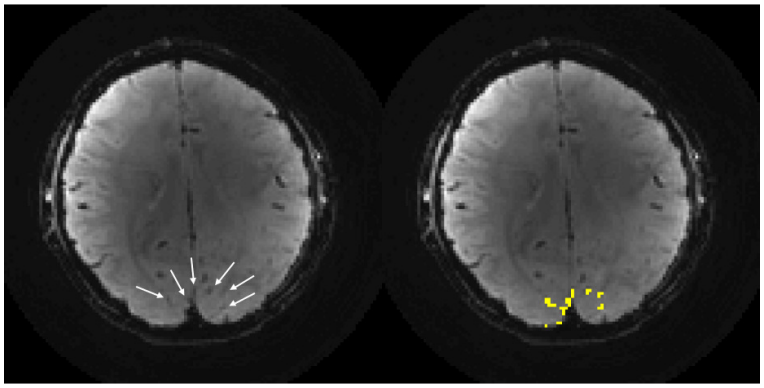

Figure 2.17: GRE background image with vasculature (left) and the activated voxels with $> 4\%$ percent signal changes overlaid to the GRE background image (right).

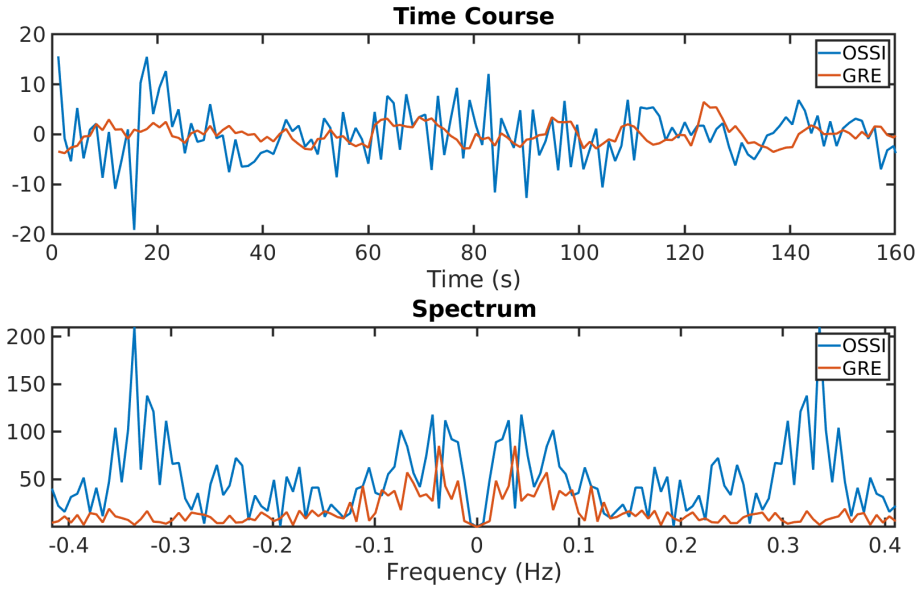

Figure 2.18: The residual time courses and spectra averaged over a larger ROI (20×20 voxels) away from the active regions after mean and drift removal. The large ROI eliminates the effect of thermal noise. The OSSI spectrum has higher physiological noise due, in part, to larger signals, but the presence of a prominent peak near respiration frequencies demonstrates potential greater sensitivity of physiological noise. The phyisological noise may cause the tSNR improvement to be less than that predicted from signal strength alone.

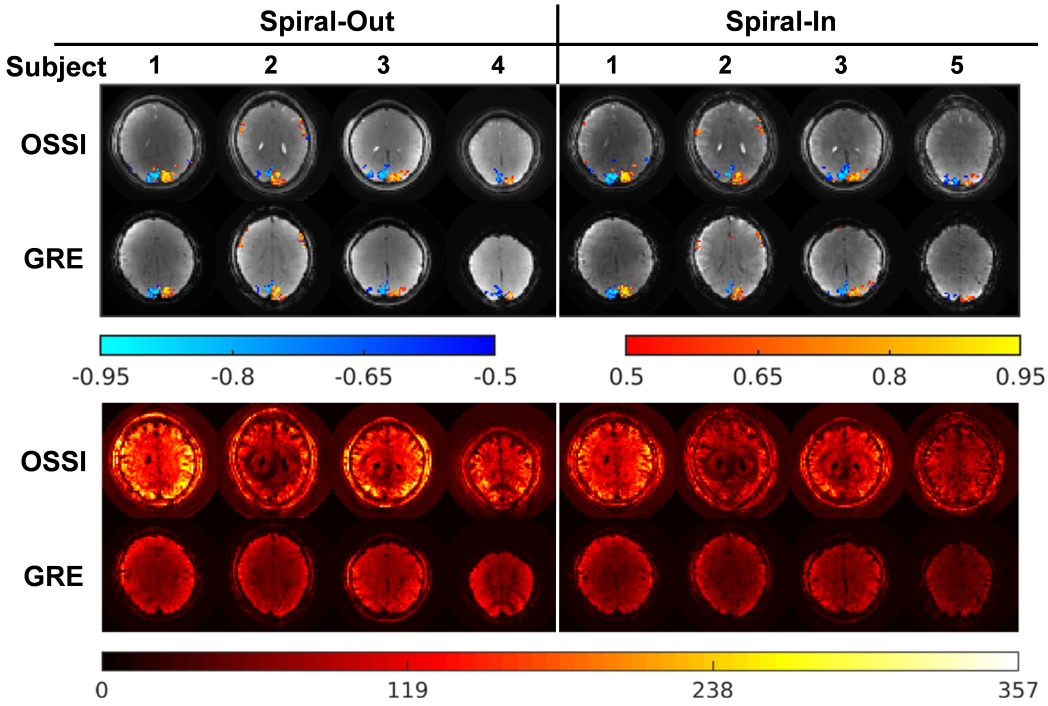

Figure 2.19: Comparison of OSSI and GRE activation maps and tSNR maps for all the experiments reconstructed at a lower spatial resolution.

2.7.2.3 Comparison to GRE TR = 50 ms

We further compared OSSI to GRE TR = 50 ms with 3× more time points. It is shown in Fig. 2.20 and Table 2.3 that GRE TR = 50 ms or 150 ms for each interleave give similar functional results and tSNR values for the thermal noise limited experimental conditions.

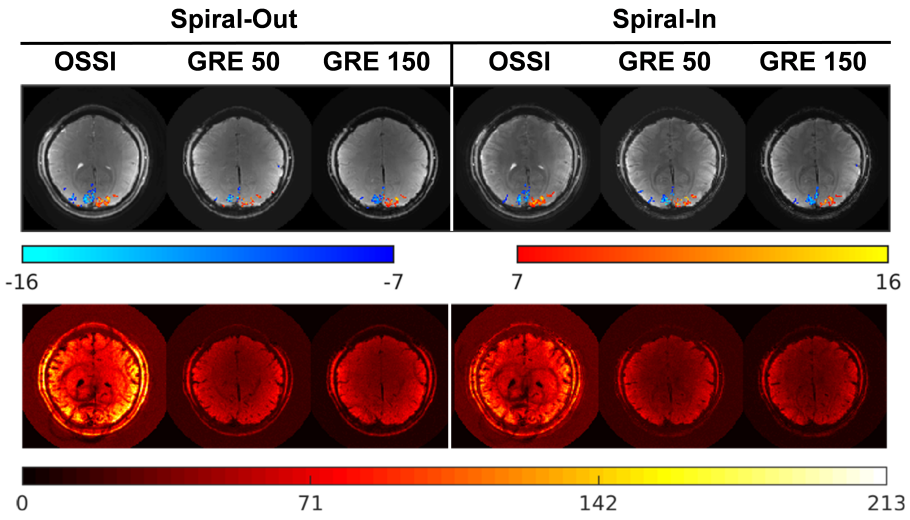

Figure 2.20: Z-maps and tSNR maps of OSSI, GRE TR = 50 ms, and GRE TR = 150 ms for both spiral-out and spiral-in acquisitions. The z-score threshold = ±7 and corresponds to correlation = ±0.5 for the GRE TR = 150 ms case. For GRE TR = 50 ms, averaged images of every 3 time points are used for tSNR calculation.

Table 2.3: Quantitative measures including number of voxels beyond a z-score threshold of ±7 and average tSNR within the brain.

	Spiral-Out			Spiral-In		
	OSSI	GRE TR 50 ms	GRE TR 150 ms	OSSI	GRE TR 50 ms	GRE TR 150 ms
# Activated Voxels	182	120	125	194	145	128
Average tSNR	74.4	41.1	41.9	60.5	36.3	34.0

OSSI, oscillating steady-state imaging; GRE, gradient echo imaging; tSNR, temporal signal-to-noise ratio.

CHAPTER III

High-Resolution Oscillating Steady-State fMRI using Patch-Tensor Low-Rank Reconstruction

The goals of fMRI acquisition include high spatial and temporal resolutions with a high signal to noise ratio (SNR). Oscillating Steady-State Imaging (OSSI) is a new fMRI acquisition method that provides large oscillating signals with the potential for high SNR, but does so at the expense of spatial and temporal resolutions. The unique oscillation pattern of OSSI images makes it well suited for high-dimensional modeling. We propose a patch-tensor low-rank model to exploit the local spatial-temporal low-rankness of OSSI images. We also develop a practical sparse sampling scheme with improved sampling incoherence for OSSI. With an alternating direction method of multipliers (ADMM) based algorithm, we improve OSSI spatial and temporal resolutions with a factor of 12 acquisition acceleration and 1.3 mm isotropic spatial resolution in prospectively undersampled experiments. The proposed model yields high temporal SNR with more activation than other low-rank methods. Compared to the standard gradient echo (GRE) imaging with the same spatial-temporal resolution, 3D OSSI tensor model reconstruction demonstrates 2 times higher temporal SNR with 2 times more functional activation. [1]

3.1 Introduction

Functional magnetic resonance imaging (fMRI) measures neural activity based on blood-oxygenation-level-dependent (BOLD) contrast and the hemodynamic correlations [59] by acquiring a time series of T_2^*-weighted brain images. BOLD signal

[1] This chapter was published in [19, 52, 58].

change from fMRI images acquired with the standard gradient echo (GRE) imaging is small and can be easily buried in noise. Furthermore, as signal to noise ratio (SNR) is proportional to voxel size and functional units of the brain are on the order of 1 mm or smaller, high SNR is critical for high-resolution and high-quality fMRI. However, current methods for SNR improvements are limited: multi-coil head arrays suffer from diminished returns for deep brain structures, and high magnetic field systems are costly. This chapter focuses on Oscillating Steady-State Imaging (OSSI) [16], a new fMRI acquisition method that has the potential to provide 2 times higher SNR than the standard GRE approach.

OSSI combines balanced gradients and a quadratic RF phase progression with large phase increments, and leads to a combination of high SNR of the balanced steady state and T_2^*-weighting of GRE imaging. The quadratic RF phase cycling is $\phi(n) = \pi n^2/n_c$, where n is the RF index and n_c is the cycle length. For $n_c = 1$, $\Delta\phi$ between RF pulses is 180°, which is balanced steady-state free precession (bSSFP). For $n_c \geq 120$ with very small $\Delta\phi$, the mechanism leads to bSSFP-like contrast [34]. OSSI acquisitions use $1 < n_c < 120$ that produce large and oscillating signals. Specifically, by selecting a short repetition time (TR) with $n_c = 10$, OSSI demonstrates a similar T_2^*-weighted contrast mechanism as GRE with additional T_2'-weighting of about 15 ms immediately after the RF pulse. Details on how the SNR and T_2^*-sensitivity vary with n_c and other acquisition parameters can be found in [16].

The OSSI signal oscillates with a periodicity dictated by the quadratic RF phase cycling, and OSSI images have a periodic oscillation pattern that repeats every n_c images as illustrated in Figs. 3.1, 3.9 and 3.10. Thus, one must acquire and combine n_c as many images to get images that are free of oscillations and suitable for fMRI analysis. With standard reconstruction methods, this need would compromise temporal resolution by a factor of n_c, and the short TR requirement necessary for steady-state imaging (e.g., TR = 15 ms) limits the time for traversing k-space and thus limits the single-shot spatial resolution. We aspire to improve the spatial and temporal resolutions by designing a sparse sampling scheme and an accurate reconstruction method.

Past works on reconstructing fMRI time series use models such as low-rank [60], low-rank and sparse [61], and low-rank plus Fourier domain sparsity [62, 10] that impose low-rankness and/or sparsity on matrices of the vectorized space dimension and time. We found them insufficient for OSSI, as the oscillations in OSSI images

make them neither low-rank nor sparse along the time dimension. To simultaneously exploit redundancy in the oscillation pattern of OSSI and the repeated acquisition for fMRI time courses, we structure OSSI images to have two time dimensions and develop a patch-based tensor model.

Based on the n-rank definition [63] and tensor nuclear norm [64] for tensor competition [64, 65], global tensor low-rank or low-rank plus sparse reconstruction models have been applied to dynamic MRI via space $x \times$ space $y \times$ time [66], cardiac MRI via space $\times$ time $\times$ cardiac phases [67], and quantitative cardiovascular magnetic resonance multitasking with multiple time dimensions [68].

Instead of tensor nuclear norm, global tensor low-rank models have also been explored via Tucker decomposition or higher-order SVD (HOSVD) [63, 69] for dynamic MRI with sparse core tensors [70], high-dimensional MR imaging with sparsity constraints and tensor subspace estimated from navigator data [71], multi-dimensional dynamic phosphorus-31 magnetic resonance spectroscopy and imaging [72], and electron paramagnetic resonance oxygen imaging [73] with specialized sparse sampling strategies. Furthermore, the CANDECOMP/PARAFAC (CP) decomposition [63] was exploited for multi-contrast dynamic cardiac MRI denoising [74] and for tensor completion with designed regular sub-Nyquist sampling with applications for fMRI acceleration [75].

Previous patch-wise tensor low-rank models impose low-rank constraints on spatial submatrices of the tensor unfoldings [76, 77], select patches with both local and non-local similarities and exploit patch-tensor low-rankness using HOSVD for multi-contrast MRI reconstruction [78], or compare CP and Tucker decompositions for local and global low-rank tensor denoising [74]. Because both CP and Tucker decompositions require selection of tensor ranks, our work focuses on tensor nuclear norm minimization that avoids explicit selection of tensor ranks, and structures local patch-tensors to exploit the local and high-dimensional spatial-temporal low-rankness. We further design a sparse sampling scheme that prospectively undersamples the data with a 12-fold acceleration for 2D and a 10-fold acceleration for 3D. The proposed model provides high-resolution reconstructions with high temporal SNR (tSNR) and more functional activation than global tensor or matrix low-rank models.

Patch-tensor low-rank (patch-tensor LR) reconstruction and the sparse sampling schemes are new for fMRI, and the application to OSSI fMRI data is also new. Compared to standard GRE imaging, the proposed OSSI tensor model demonstrates

a factor of 2 tSNR improvement for fMRI with 2 times larger functional activation.

The chapter is organized as follows. Section II presents notations and definitions for tensors. Section III proposes the patch-tensor model and optimization algorithm. Section IV develops the incoherent undersampling and describes the experimental setup for OSSI fMRI studies. Section V demonstrates the improved functional performance using the proposed approach compared to other reconstruction and acquisition methods. Section VI discusses future directions, and Section VII concludes the chapter.

3.2 Background and Notation

A tensor is a multidimensional array [63]. We denote tensors according to their dimensions. One-dimensional tensors or vectors are denoted by bold lowercase letters, e.g., $\mathbf{x}$, and tensors of dimension two or higher are denoted by bold capital letters, e.g., $\mathbf{X}$. Scalars are denoted by italic letters, e.g., x.

The inner product of two tensors $\mathbf{X}, \mathbf{Y} \in \mathbb{C}^{I_1 \times I_2 \times \cdots \times I_N}$ is defined as the sum of the element-wise products [69],

$$\langle \mathbf{X}, \mathbf{Y} \rangle = \sum_{i_1=1}^{I_1} \sum_{i_2=1}^{I_2} \cdots \sum_{i_N=1}^{I_N} y^*_{i_1 i_2 \cdots i_N} x_{i_1 i_2 \cdots i_N},$$

where $*$ denotes the complex conjugate. Naturally, the norm of tensor $\mathbf{X}$ is $\|\mathbf{X}\| = \sqrt{\langle \mathbf{X}, \mathbf{X} \rangle}$.

The process of reforming a tensor to matrices by reordering the vectors of the tensor is known as matricization or unfolding. Each dimension of a tensor is known as a mode, and the number of modes is known as the tensor's order or number of dimensions. After unfolding, the tensor becomes matrices of different modes, and the number of these matrices equals the number of dimensions. Figure 3.2 illustrates unfolding a three-dimensional tensor to three matrices. The mode-n unfolding of tensor $\mathbf{X}$ is denoted by $\mathbf{X}_{(n)}$, accordingly, refolding the mode-n matrix back to $\mathbf{X}$ is $\textsc{Refold}_n\left(\mathbf{X}_{(n)}\right)$. As seen in [63] and [69], different papers may use different permutations of the vectors to get the unfoldings; the specific order is unimportant as long as it is consistent.

The n-rank of $\mathbf{X}$ is the column rank of $\mathbf{X}_{(n)}$ and is denoted by $\text{rank}\left(\mathbf{X}_{(n)}\right) = r_n$. Therefore, $\mathbf{X}$ is a rank-$(r_1, r_2, \ldots, r_N)$ tensor.

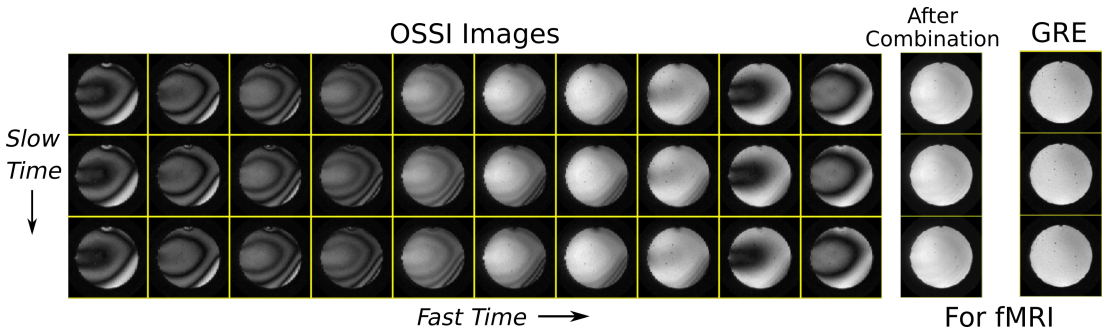

Figure 3.1: OSSI images with periodic oscillation patterns are structured along "fast time" and "slow time" dimensions. Every $n_c = 10$ fast time images can be 2-norm combined to generate fMRI images that are free of oscillations and have T_2^*-sensitivity comparable to standard GRE imaging.

3.3 Reconstruction Methods

This section introduces the patch-tensor LR model based reconstruction problem, the optimization algorithm, important implementation details, and other reconstruction methods for comparison.

3.3.1 Tensor Model Problem Formulation

fMRI involves acquiring a time series of images to track brain activity. In OSSI fMRI, the images periodically oscillate with every n_c time points along with the regular fMRI time course as shown in Fig. 3.1. Typically, we combine every n_c consecutive and non-overlapping images with root sum squared (2-norm) to get uniform images for fMRI analysis [16]. To simultaneously exploit the redundancy in OSSI oscillatory patterns and the repetition along fMRI time series, we structure OSSI fMRI images into two time dimensions. The fast oscillation dimension is called "fast time", and the fMRI time dimension is called "slow time".

To improve both spatial and temporal resolutions for OSSI fMRI, and to model the reproducibility in both fast and slow time dimensions, we propose a tensor low-rank model for the undersampled reconstruction. The tensor dimensions include vectorized space, fast time $= n_c$, and slow time. Since the exact form of the oscillations is resonant frequency dependent and resonant frequency usually varies slowly across space, low-rankness involving the fast oscillations is a local feature (more similarities among neighboring pixels than between non-local pixels or over the whole image).

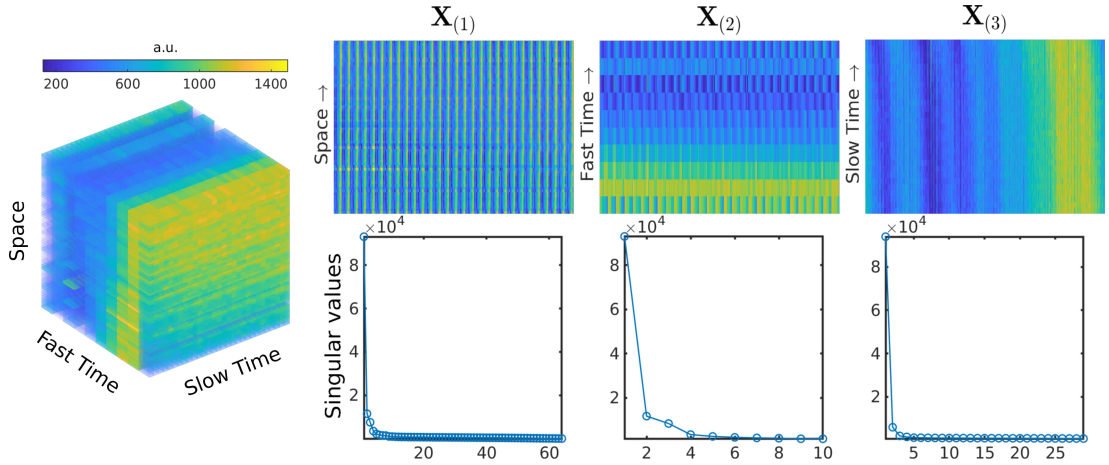

Figure 3.2: A 3D patch-tensor (left), its three matrix unfoldings of different modes (top right), and the singular values of the unfoldings demonstrating the patch-tensor low-rank (bottom right).

Furthermore, due to the complexity of functional activity, imposing low-rankness on temporal blocks instead of the whole fMRI time series improves the modeling accuracy. Therefore, we propose a patch-tensor LR model with limited spatial and temporal extent, and impose low-rankness on all the unfoldings of the patch-tensor.

The whole fMRI time series is broken into non-overlapping time blocks. For each block, we reshape 3D (space x × space y × time t) or 4D (space x × space y × space z × time t) OSSI images into 4D ($x \times y \times$ fast time $n_c \times$ slow time t_s) or 5D ($x \times y \times z \times$ fast time $n_c \times$ slow time t_s) tensors. We partition the 4D or 5D tensors into patches, and vectorize all the spatial dimensions to form 3D low-rank patch-tensors (vectorized space $s_p \times n_c \times t_s$). Figure 3.2 visualizes an in vivo 3D patch-tensor, its three unfoldings, and the corresponding singular values demonstrating the low-rankness of the unfoldings. The patch-tensor is from the center of a brain with no activation, and Fig. 3.13(a) plots the corresponding log-scale singular values. Figure 3.13(b) presents low-rank unfoldings of a different patch-tensor in an activated region.

The proposed patch-tensor LR model based reconstruction problem with non-overlapping patches is

$$\arg\min_{\mathbf{x}} \sum_{m=1}^{M} \sum_{i=1}^{3} \lambda_i \operatorname{rank}\left(\mathcal{P}_{mi}(\mathbf{X})\right) + \frac{1}{2}\|\mathcal{A}(\mathbf{X}) - \mathbf{y}\|_2^2, \tag{3.1}$$

where $\mathbf{X} \in \mathbb{C}^{x \times y\,(\times z) \times t}$ is a complex OSSI fMRI time block to be reconstructed. Linear operator $\mathcal{P}(\cdot)$ partitions and reshapes its input into M locally low-rank patch-tensors with $\mathcal{P}_m(\mathbf{X}) \in \mathbb{C}^{s_p \times n_c \times t_s}$, $m = 1, \ldots, M$. $\mathcal{P}_{mi}(\mathbf{X}) = \mathcal{P}_m(\mathbf{X})_{(i)}$ denotes the mode-i unfolding of the mth tensor patch $\mathcal{P}_m(\mathbf{X})$. λ_i is the regularization parameter for low-rankness of the mode-i unfolding. Linear operator $\mathcal{A}$ represents the MRI physics; it consists of coil sensitivities and the non-uniform Fourier transform (NUFFT) including undersampling. $\mathbf{y}$ denotes sparsely sampled k-space measurements.

We focus on the following convex relaxation of (3.1):

$$\arg\min_{\mathbf{X}} \sum_{m=1}^{M} \sum_{i=1}^{3} \lambda_i \|\mathcal{P}_{mi}(\mathbf{X})\|_* + \frac{1}{2}\|\mathcal{A}(\mathbf{X}) - \mathbf{y}\|_2^2. \tag{3.2}$$

This formulation encourages low-rankness of all the patch-tensor unfoldings by minimizing the sum of their singular values. Meanwhile, the data fidelity term encourages correspondence between the images and the acquired k-space samples.

3.3.2 Optimization Algorithm

The regularizers in the unconstrained cost function (3.2) can be handled via the alternating direction method of multipliers (ADMM) [79, 65] applied to the equivalent constrained optimization problem:

$$\begin{aligned} &\arg\min_{\mathbf{Z}} \ \min_{\{\mathbf{X}_i\}} \sum_{m=1}^{M} \sum_{i=1}^{3} \lambda_i \|\mathcal{P}_{mi}(\mathbf{X}_i)\|_* + \frac{1}{2}\|\mathcal{A}(\mathbf{Z}) - \mathbf{y}\|_2^2 \\ &\text{subject to } \mathbf{X}_i = \mathbf{Z}, \ i = 1, 2, 3, \end{aligned} \tag{3.3}$$

with $\mathbf{X}_i \in \mathbb{C}^{x \times y\,(\times z) \times t}$, $i = 1, 2, 3$ constrained to be equal to $\mathbf{Z} \in \mathbb{C}^{x \times y\,(\times z) \times t}$. The scaled form of the corresponding augmented Lagrangian is

$$\begin{aligned} \mathcal{L}\left(\{\mathbf{X}_i\}, \mathbf{Z}, \{\mathbf{U}_i\}\right) &= \sum_{m=1}^{M} \sum_{i=1}^{3} \lambda_i \|\mathcal{P}_{mi}(\mathbf{X}_i)\|_* \\ &+ \frac{1}{2}\|\mathcal{A}(\mathbf{Z}) - \mathbf{y}\|_2^2 + \frac{\rho}{2} \sum_{i=1}^{3} \|\mathbf{X}_i - \mathbf{Z} + \mathbf{U}_i\|^2 - \frac{\rho}{2} \sum_{i=1}^{3} \|\mathbf{U}_i\|^2. \end{aligned} \tag{3.4}$$

We update the variables $\{\mathbf{X}_i\}$, $\mathbf{Z}$ and scaled dual variables $\{\mathbf{U}_i\}$ sequentially, holding the other variables fixed.

For non-overlapping patch-tensors, the update step for each patch of $\{\mathbf{X}_i\}_{i=1}^3$ is:

$$\mathcal{P}_m(\mathbf{X}_i^{k+1}) = \underset{\mathcal{P}_m(\mathbf{X}_i)}{\arg\min}\ \mathcal{L}_{mi}\left(\mathcal{P}_m(\mathbf{X}_i), \mathbf{Z}^k, \mathbf{U}_i^k\right) \tag{3.5}$$

for $m = 1, \ldots, M$ and $i = 1, \ldots, 3$ at iteration $k+1$, where

$$\begin{aligned}\mathcal{L}_{mi} &= \lambda_i \|\mathcal{P}_{mi}(\mathbf{X}_i)\|_* + \frac{\rho}{2}\|\mathcal{P}_m(\mathbf{X}_i) - \mathcal{P}_m(\mathbf{Z}^k - \mathbf{U}_i^k)\|^2 \\ &= \lambda_i \|\mathcal{P}_{mi}(\mathbf{X}_i)\|_* + \frac{\rho}{2}\|\mathcal{P}_{mi}(\mathbf{X}_i) - \mathcal{P}_{mi}\big(\mathbf{Z}^k - \mathbf{U}_i^k\big)\|_F^2.\end{aligned} \tag{3.6}$$

Because $\mathcal{P}_{mi}(\mathbf{X}_i)$ and $\mathcal{P}_{mi}\big(\mathbf{Z}^k - \mathbf{U}_i^k\big)$ are matrices, patch update $\mathcal{P}_{mi}\big(\mathbf{X}_i^{k+1}\big)$ is easily obtained with a singular value soft-thresholding operator $\mathrm{SVT}(\cdot)$ with threshold λ_i/ρ,

$$\begin{aligned}\mathcal{P}_{mi}\big(\mathbf{X}_i^{k+1}\big) &= \underset{\mathcal{P}_{mi}(\mathbf{X}_i)}{\arg\min}\ \mathcal{L}_{mi}\left(\mathcal{P}_{mi}(\mathbf{X}_i), \mathbf{Z}^k, \mathbf{U}_i^k\right) \\ &= \mathrm{SVT}_{\lambda_i/\rho}\left(\mathcal{P}_{mi}\big(\mathbf{Z}^k - \mathbf{U}_i^k\big)\right).\end{aligned} \tag{3.7}$$

Therefore, the update for the patches of $\{\mathbf{X}_i\}$ becomes

$$\mathcal{P}_m(\mathbf{X}_i^{k+1}) = \textsc{Refold}_i\left(\mathcal{P}_{mi}\big(\mathbf{X}_i^{k+1}\big)\right). \tag{3.8}$$

We parallelize this step over all the unfoldings and patches.

The $\mathbf{Z}$ update simplifies to:

$$\begin{aligned}\mathbf{Z}^{k+1} =& \arg\min_{\mathbf{Z}}\ \mathcal{L}\left(\{\mathbf{X}_i^{k+1}\}, \mathbf{Z}, \{\mathbf{U}_i^k\}\right) \\ =& \arg\min_{\mathbf{Z}}\ \Bigg(\frac{1}{2}\|\mathcal{A}(\mathbf{Z}) - \mathbf{y}\|_2^2 \\ &+ \frac{\rho}{2}\sum_{i=1}^{3}\|\mathbf{Z} - \big(\mathbf{X}_i^{k+1} + \mathbf{U}_i^k\big)\|^2\Bigg).\end{aligned} \tag{3.9}$$

We use the conjugate gradient method for this least-squares minimization.

The scaled dual variables $\{\mathbf{U}_i\}_{i=1}^3$ are updated in the usual ADMM way by

$$\mathbf{U}_i^{k+1} = \mathbf{U}_i^k + \mathbf{X}_i^{k+1} - \mathbf{Z}^{k+1}. \tag{3.10}$$

3.3.3 Practical Considerations

3.3.3.1 Random Cycle Spinning

The singular value soft-thresholding operation for non-overlapping patch-tensors leads to blocking artifacts at the boundaries of the patches. Using overlapping patches would be computationally intensive, so instead we apply random cycle spinning in every iteration as in [80, 81]. We perform a randomly chosen circular shift along each dimension of the input tensor before partitioning and reshaping, and unshift the tensor back after updating and placing the patch-tensors together. Accordingly, the actual update for the patches of each $\mathbf{X}_i$ is

$$\begin{aligned} &\mathcal{P}_m\big(\textsc{Shift}\big(\mathbf{X}_i^{k+1}\big)\big) = \\ &\qquad \textsc{Refold}_i\big(\mathrm{SVT}_{\lambda_i/\rho}\big(\mathcal{P}_{mi}\big(\textsc{Shift}\big(\mathbf{Z}^k - \mathbf{U}_i^k\big)\big)\big)\big)\,. \end{aligned} \tag{3.11}$$

3.3.3.2 Overlapping Time Blocks

We reconstruct each fMRI time block separately to lighten the memory burden, so random cycle spinning only removes patch boundary artifacts within each block. To further reduce potential artifacts at the temporal boundaries of the blocks, we reconstruct overlapping time blocks and discard additional time points near the boundaries for all the methods. Figure 3.17 illustrates how the ranges and discarded portions of the time blocks are selected.

3.3.3.3 ADMM Implementation Details

We scale the k-space data to have maximum magnitude of 1 before applying ADMM. With this normalization, simply setting the regularization parameters $\lambda_1 = \lambda_2 = 1$ works well. Because $\mathbf{X}_{(3)}$ has lower rank than $\mathbf{X}_{(1)}$ and $\mathbf{X}_{(2)}$ as shown in Fig. 3.2, we choose $\lambda_3 = 2$ to provide more weighting to the low-rankness of $\mathbf{X}_{(3)}$.

For ADMM penalty parameter ρ, we investigated a range of ρ values and found $\rho = 121$ empirically to be a good initialization. Furthermore, for our application, using varying penalty parameter or increasing ρ after a number of inner iterations contributes to a faster convergence. After T inner iterations updating variables $\{\mathbf{X}_i\}$, $\mathbf{Z}$,

and $\{\mathbf{U}_i\}$, the following updates are performed in the outer iteration:

$$\begin{aligned} \rho &\mapsto r\rho \\ \mathbf{U}_i &\mapsto \mathbf{U}_i/r. \end{aligned} \tag{3.12}$$

We chose rate $r = 3$, and rescale the scaled dual variable $\mathbf{U}_i$ after updating ρ. This scheme is adapted from [79, 65]. Algorithm 1 summarizes the method.

Algorithm 1 Patch-tensor low-rank reconstruction algorithm

Input: $\mathcal{A}$, $\mathbf{y}$, $\{\lambda_i\} = [1\,1\,2]$, $\rho = 121$, $r = 3$, $S = 2$, $T = 11$
Output: OSSI images $\mathbf{Z}^{k+1}$

```
for s = 0, ..., S − 1 do
    for t = 0, ..., T − 1 do
        k = s ∗ T + t
        Update Z^{k+1} using (3.9)
        for i = 1, 2, 3 do
            Update X_i^{k+1} using (3.11)
            U_i^{k+1} = U_i^k + X_i^{k+1} − Z^{k+1}
        end for
    end for
    Update ρ and each U_i using (3.12)
end for
return Z^{k+1}
```

3.3.4 Other Reconstruction Approaches

We compare the proposed reconstruction method to matrix local low-rank (MLLR) [82], global tensor low-rank (GTLR), patch-tensor low-rank plus sparse (patch-tensor L+S), and conjugate gradient SENSE [42, 43] with an edge-preserving regularizer (regularized CG-SENSE).

MLLR imposes low-rank constraints on space $\times$ time matrices by vectorizing image patches for the spatial dimension. The cost function for MLLR is the same as setting $i = 1$ in (3.2). GTLR enforces low-rankness on all the unfoldings of the tensor of size space $xy \times n_c \times t_s$ without taking patches. The cost function is the same as (3.2) with $M = 1$ and without spatial partitioning. GTLR reconstructs fMRI time blocks and is global in spatial sense but not in temporal sense. It is less convenient for computation to impose low-rankness on a temporal global tensor.

The optimization problem for patch-tensor L+S is

$$\arg\min_{\mathbf{L},\mathbf{S}} \frac{1}{2}\|\mathcal{A}(\mathbf{L}+\mathbf{S})-\mathbf{y}\|_2^2 + \sum_{m=1}^{M}\sum_{i=1}^{3}\lambda_i\|\mathcal{P}_{mi}(\mathbf{L})\|_* + \mu\|\Phi(\mathbf{S})\|_1,$$

where $\mathbf{L},\mathbf{S}\in\mathbb{C}^{x\times y\times t}$ denote the image components to be reconstructed and Φ denotes 2D Fourier transform along both fast and slow time dimensions to enhance the Fourier domain sparsity of the sparsity component $\mathbf{S}$. The low-rank component $\mathbf{L}$ has the same regularization as in (3.2), and λ_i and μ are regularization parameters.

The optimization problem for regularized CG-SENSE is

$$\arg\min_{\mathbf{X}} \frac{1}{2}\|\mathcal{A}(\mathbf{X})-\mathbf{y}\|_2^2 + \sum_{j=1}^{J}\psi\left([\mathbf{C}\mathbf{X}]_j\right),$$

where $\mathbf{X}\in\mathbb{C}^{xy}$ denotes one vectorized image of the time series, $\mathbf{C}\in\mathbb{R}^{J\times xy}$ is the 2D spatial finite difference matrix with $J=2xy$, and ψ is the Huber potential function.

We used ADMM to perform the MLLR, GTLR, and patch-tensor L+S reconstructions. The ADMM parameters for patch-tensor L+S were the same as (3.12) for patch-tensor LR. The CG update in the ADMM inner iterations and the regularized CG-SENSE reconstruction were implemented with the Michigan Image Reconstruction Toolbox [44].

3.4 Acquisition Methods

Each oscillating state (index n) of OSSI was acquired with quadratic RF phases $\phi(n)=\pi n^2/n_c$, cycle length $n_c=10$, TR = 15 ms, and flip angle = 10° for the desired SNR and T_2^*-sensitivity [16]. The short TR of 15 ms limits the readout, and $n_c=10$ compromises temporal resolution. Hence, sparse sampling is important for improving OSSI spatial and temporal resolutions.

This section develops practical sparse sampling schemes with increased sampling incoherence for OSSI, and describes human fMRI studies. We collected 2D "mostly sampled" with retrospective undersampling, 2D prospectively undersampled, and 3D prospectively undersampled data. With FOV = 220 mm, slice thickness = 2.5 mm, and matrix size = 168×168, the spatial resolution = $1.3\times1.3\times2.5$ mm^3 for all experiments.

3.4.1 Variable-Density Spiral Sampling Trajectory

We focus on variable-density (VD) spiral trajectories that travel quickly through k-space. The sampling density of VD spirals varies at different k-space radii. By dense sampling in the center of k-space where the MR energy concentrates and sparse sampling at outer k-space, VD spirals can reduce imaging time and off-resonance blur [83, 84] compared to uniform-density (UD) spirals. We design VD spirals based on [85, 86] with uniform density and over-sampling in the k-space center, and then linearly decrease the sampling density as the spirals approach the outer part of k-space. The trajectory is parameterized by (n_i, a, b, d), where n_i = number of interleaves, a = effective FOV (in mm) at k-space center, b = effective FOV at the edge of k-space, and d denotes the number of central k-space points with uniform sampling density determined by a.

We used (n_i, a, b, d) = (9, 310, 110, 300) for the retrospective sampling pattern with spiral-out readouts. The effective FOV for $n_i = 9$ interleaves was $a = 310$ mm at the center of k-space for the first $d = 300$ sampling points, then decreased linearly to $b = 110$ mm at the edge of k-space. The readout length for each interleave was 8.3 ms. The k-space of each image can be mostly covered with all the 9 interleaves. However, due to the variable-density nature of the trajectories, the 9-interleave trajectory was still undersampled by approximately a factor of 1.5, and we refer to this sampling pattern as "mostly sampled". We chose $a = 300$ mm and $b = 80$ mm for prospective undersampling with spiral-in readouts to increase T_2^*-sensitivity, and the readout length was 7.4 ms.

We took 1 interleave out of $n_i = 9$ VD spirals as the undersampled trajectory. Compared to a UD spiral with the same FOV and matrix size, the single-shot undersampled trajectory provided a factor of 12 acceleration in-plane as presented in Fig. 3.3 (a). We selected the VD spiral parameters for a good balance between the undersampling factor and reconstruction performance.

3.4.2 Incoherent Sampling for Time Dimensions and 3D

The proposed spiral trajectory provides aggressive undersampling in-plane and would introduce reconstruction artifacts if used without regularization. As we are using a tensor model with two time dimensions for the undetermined reconstruction problem, we prefer the sampling pattern to be incoherently varying along the two

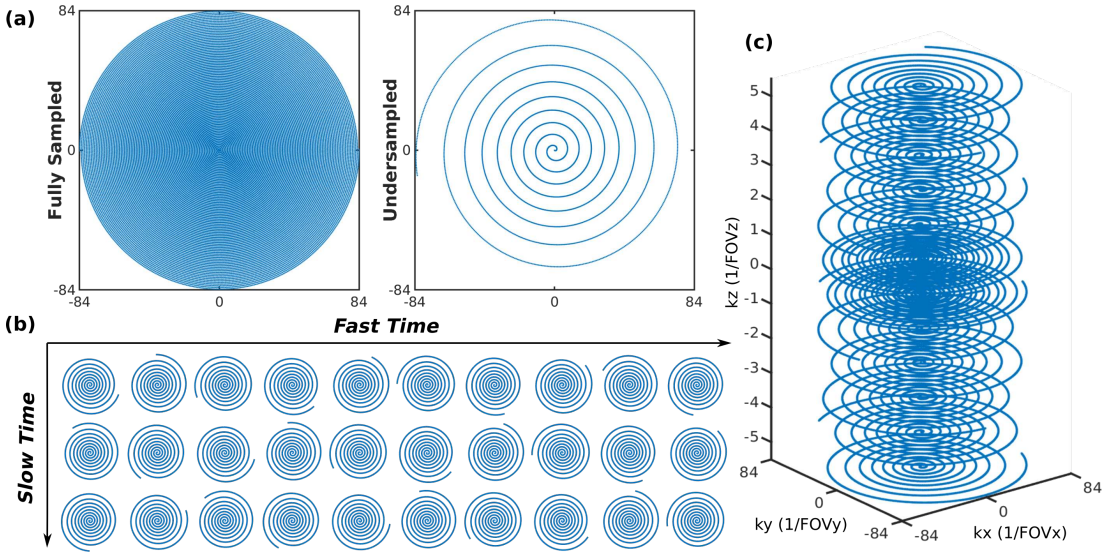

Figure 3.3: (a) Compared to the fully sampled trajectory, the designed single-shot variable-density spiral trajectory for each time frame or k_z plane enables a 12-fold acquisition acceleration. (b) Prospective 2D undersampling pattern with the incoherent rotations between fast time (the oscillation dimension) and slow time (the fMRI time dimension). (c) 3D undersampled stack-of-spirals providing a 10-fold acceleration with one spiral for the outer k_z planes, two spirals for the two central k_z planes, and golden-angle rotations between k_z planes.

dimensions for artifact reduction [87]. Therefore, we rotate the VD spiral using a golden-angle based approach for each temporal frame to avoid overlapping trajectories in both fast and slow time dimensions.

We define an interleave index $k = 0, \ldots, K-1$ for a time series of OSSI images with K interleaves in total. For 2D retrospective sampling with multi-shot acquisition, the rotation angle for each interleave k was

$$ga \cdot k + 2 \cdot ga \cdot \lfloor k/n_c/n_i \rfloor \,, \tag{3.13}$$

where $ga = 111.246^\circ$ is the golden angle, $n_c = 10$ is the size of fast time dimension, n_i is the number of interleaves, and $\lfloor \cdot \rfloor$ denotes the floor function. The acquisition for the interleaves first looped through OSSI oscillation states 1 to n_c, then looped through multi-shot 1 to n_i, and after that proceeded to the next slow time point.

For 2D prospective undersampling, only 1 VD interleave was collected for each image, and the rotation angle was

$$ga \cdot k + ga \cdot \lfloor k/n_c \rfloor \,. \tag{3.14}$$

The index k looped through OSSI fast time oscillations for every slow time point. Figure 3.3 (b) presents the prospective sampling pattern. The baseline rotation was determined by the golden angle. The second terms in (3.13) and (3.14) were designed specifically to increase sampling incoherence along slow time as shown in Figs. 3.14 and 3.15 for prospective undersampling and retrospective undersampling, respectively.

For 3D prospective undersampling, we used a stack of VD spirals with 2-shot acquisition at the 2 central k_z planes and single-shot acquisition at other k_z locations as in Fig. 3.3 (c), providing a 10-fold acceleration compared to the fully sampled k-space. Rotations in (3.14) were applied, where k looped through OSSI oscillations, then k_z planes, and finally the slow time points.

Because of the increased sampling incoherence in the two time dimensions, the angular dimension of k-space can be mostly covered with sampling trajectories of 9 or 10 consecutive time frames. We used this feature and combined k-space data of every 10 slow time points to compute data-shared initialization for reconstruction, which helped decrease the number of CG iterations and computation time.

3.4.3 Human fMRI Studies

We implemented the OSSI pulse sequence and the proposed sampling scheme using GE's standard pulse programming environment EPIC. All the data were collected on a 3T GE MR750 scanner (GE Healthcare, Waukesha, WI) with a 32-channel head coil (Nova Medical, Wilmington, MA) using the proposed retrospective and prospective undersampling schemes. Prospectively undersampled OSSI studies were further compared to standard GRE fMRI with matched spatial-temporal resolution.

The human studies were carried out under IRB approval. The fMRI task was a left vs. right reversing-checkerboard visual stimulus of 210 s with 10 s rest, 5 cycles of left or right stimulus of 20 s (20 s L/20 s R $\times$ 5 cycles).

2D OSSI used an oblique slice passing through the visual cortex. The 2D mostly sampled data were acquired with multi-shot VD spirals with number of interleaves n_i = 9, volume TR = 1.35 s (TR$\cdot n_c \cdot n_i$), and spiral-out TE = 2.7 ms. The rotation angles between interleaves and time frames were determined by (3.13). The number of time frames (both fast time n_c and slow time) was 1490 with 10 s discarded acquisition to ensure the steady state. The retrospectively undersampled data only contained the first VD interleave of every 9 interleaves.

The 2D prospectively undersampled data were collected with single-shot VD spirals ($n_i = 1$) with volume TR = 150 ms (TR $\cdot\, n_c$) and spiral-in TE = 11.7 ms. The rotation angles of the spirals were selected by (3.14). The number of fast time frames was 13340 with 10 s discarded acquisition. As every n_c images were 2-norm combined for fMRI analysis, the temporal resolution for the prospectively undersampled data was 150 ms. 2D GRE fMRI images with the same spatial resolution and temporal resolution of 150 ms as OSSI were also acquired for comparison. Specifically, GRE imaging used multi-shot spiral acquisition with $n_i = 3$, TR = 50 ms, Ernst flip angle = 16°, and spiral-in TE = 30 ms. Each interleave was VD spiral with (n_i, a, b, d) = (3, 240, 120, 300) and readout length = 21.9 ms.

For 3D imaging, an oblique slab was selected. Prospectively undersampled OSSI was compared to GRE imaging with matched spatial resolution and matched temporal resolution of 2.1 s. The number of 3D volumes was 96 for the 200 s task. For OSSI, the number of k_z planes $n_z = 12$, volume TR = 2.1 s (TR$\cdot n_c \cdot n_z$), and spiral-in TE = 10.3 ms. For GRE, multi-slice TR = 700 ms with 14 slices, multi-shot acquisition with $n_i = 3$, spiral-in TE = 30 ms, Ernst flip angle = 16°, and same VD spiral trajectories for each slice as in 2D GRE imaging were used.

For calculation of coil sensitivity maps, we collected images with a standard spin-warp sequence at TR = 50 ms, TE = 6.3 ms, and Ernst flip angle = 16°. The 32-channel coil images were compressed to 16 virtual coils for 2D and 24 virtual coils for 3D via PCA [88], and coil sensitivity maps were calculated using ESPIRiT [40, 41]. We also created coil-combined images for extraction of the brain region using the Brain Extraction Tool [39].

3.4.4 Performance Evaluation

The reconstruction and functional performances were evaluated with normalized root-mean-square difference (NRMSD) for retrospectively undersampled data, activation maps, and tSNR maps.

The retrospectively undersampled reconstruction $\hat{\mathbf{X}}$ was compared to $\mathbf{X}_{\text{ref}}$ reconstruction from "mostly sampled" data by regularized CG-SENSE, using the metric $\text{NRMSD} = \|\mathbf{X}_{\text{ref}} - \hat{\mathbf{X}}\|/\|\mathbf{X}_{\text{ref}}\|$.

Every $n_c = 10$ reconstructed images of OSSI were combined via 2-norm for functional analysis. The data from the first cycle (40 s) of the task were discarded to avoid the modeling error in the initial rest period. To reduce scanner drift effects, we detrended the data using the first 4 discrete cosine transform basis functions for both OSSI combined and GRE fMRI images.

The background of the activation map was the mean of reconstructed fMRI images. The activated regions were determined by correlation coefficients above a 0.45 threshold. Correlation coefficients were defined by correlating the fMRI time course for each voxel with the task-related reference waveform, and the reference waveform was given by convolving the task with the canonical hemodynamic response function [45]. The tSNR maps were generated by dividing the time course mean by the standard deviation of the time course residual (without the mean and the task) for each voxel. NMRSD within the brain (excluding the scalp and skull) from reconstructed images, number of activated voxels at the lower third of the brain (where the visual activation concentrates), and averaged tSNR within the brain were calculated for quantitative evaluations.

3.5 Reconstruction and Results

This section compares OSSI undersampled reconstructions using the proposed tensor model and other low-rank related approaches. 3D OSSI reconstruction is further compared to multi-slice GRE to demonstrate the SNR advantage of OSSI.

3.5.1 Regularization Parameter Adjustment

To ensure that different reconstructions have similar spatial-temporal resolutions, we compared the local impulse responses [89, 90] of the reconstruction methods. Specifically, we added an impulse perturbation $\varepsilon\mathcal{A}\left(\delta_{j,t}\right)$ to the undersampled k-space data $\mathbf{y}$ and reconstructed the perturbed data with different models. We selected j and t to be in the spatial and temporal center of the time block being reconstructed, respectively, and we chose $\varepsilon = 1$ (about 10% of the OSSI signal magnitude). Accordingly, the local impulse response is $h(j,t) = \left(\mathcal{B}\left(\varepsilon\mathcal{A}\left(\delta_{j,t}\right) + \mathbf{y}\right) - \mathcal{B}(\mathbf{y})\right)/\varepsilon$, where $\mathcal{B}(\cdot)$ denotes a reconstruction method.

Profiles of the impulse response along spatial dimension and temporal dimensions can help assess the spatial-temporal sharpness of the reconstructions for $\mathcal{B} \neq \mathcal{A}^{-1}$. As shown in Fig. 3.16, we selected regularization parameters to ensure that impulse responses of different reconstructions had similar peaks and were close to the magnitude for the regularized CG-SENSE reconstruction. Based on the ratios for the λ_i values in (3.2), the final 2D reconstruction parameters were $\{\lambda_i\} = [1\,1\,2] * 0.4$ for patch-tensor LR, $\lambda_3 = 1.6$ for MLLR, $\{\lambda_i\} = [1\,1\,2] * 4$ for GTLR, $\{\lambda_i\} = [1\,1\,2] * 0.3$ and $\mu = 3$ for patch-tensor L+S.

Furthermore, with carefully adjusted regularization parameters, reconstructing overlapping time blocks or non-overlapping time blocks for the fMRI time series led to similar results, as demonstrated by example time courses and spectra of the patch-tensor LR reconstruction in Fig. 3.18.

3.5.2 Retrospective and Prospective 2D Reconstructions

OSSI 2D retrospectively and prospectively undersampled data were reconstructed using the proposed method and the comparison methods. OSSI 2D mostly sampled data were reconstructed using regularized CG-SENSE. For the proposed retrospectively undersampled reconstructions, the number of time points before combination = 330 for every overlapping time block, and the patch-tensor size = $64\,(8*8) \times 10 \times 33$.

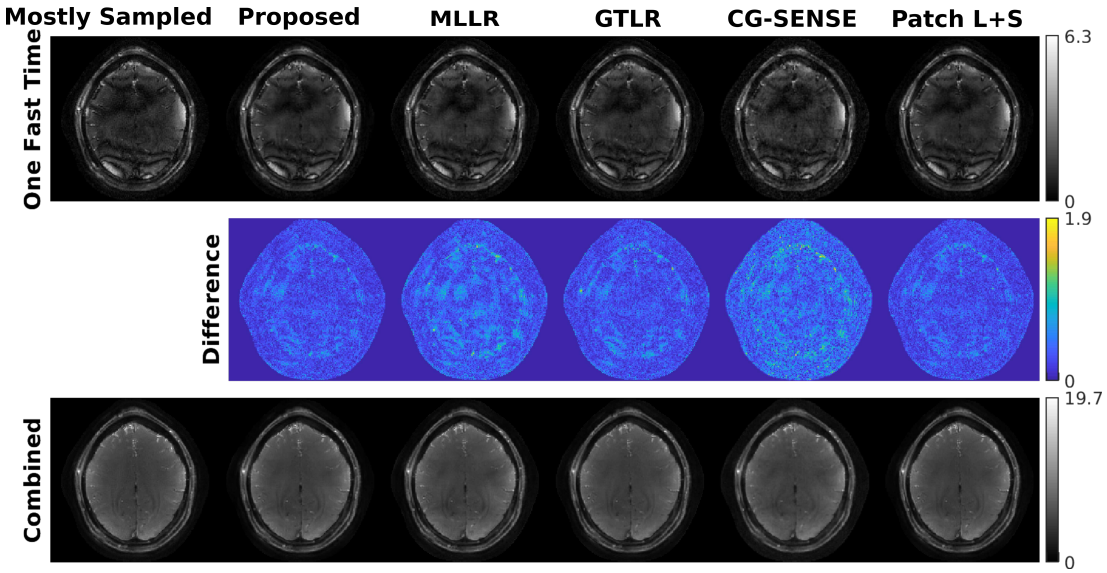

Figure 3.4: Fast time images from the retrospectively undersampled reconstructions are compared to the mostly sampled results. The proposed approach outperforms other methods with less noisy fast time images, less structure in the difference maps before combination, and high-resolution 2-norm combined images.

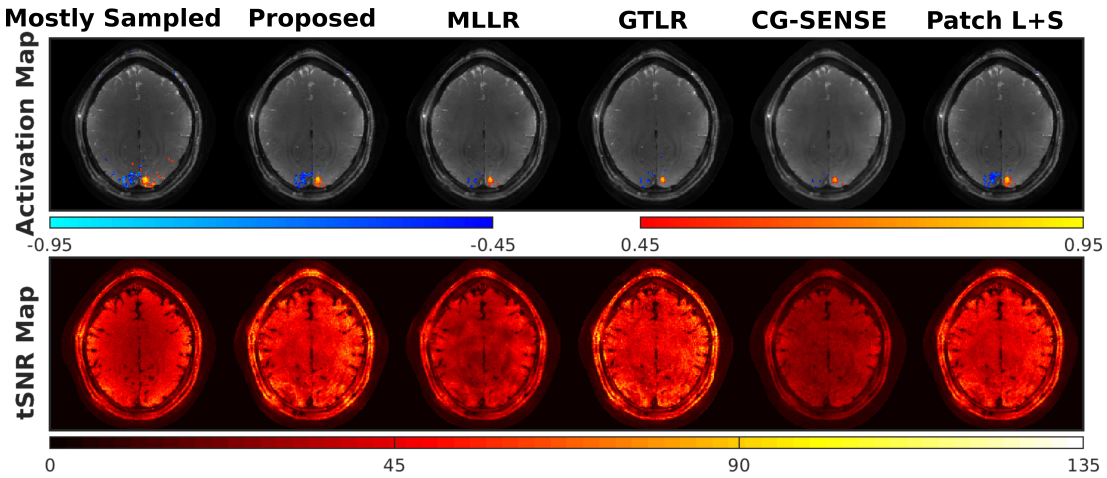

Figure 3.5: Activation maps and temporal SNR maps from retrospectively undersampled reconstructions. A contiguity (cluster-size) threshold of 2 was applied for the activated regions. The proposed model provides more functional activation than other approaches with high temporal SNR, and shows similar results as the patch-tensor low-rank plus sparse model.

Table 3.1: Quantitative comparisons of OSSI retrospectively undersampled reconstructions

	Mostly Sampled	Proposed	MLLR	GTLR	CG-SENSE	Patch L+S
NRMSD Before Comb	-	0.17	0.22	0.18	0.25	0.17
NRMSD After Comb	-	0.05	0.06	0.07	0.07	0.06
# Activated Voxels	229	168	73	68	46	153
Average tSNR	37.1	43.6	32.4	44.1	25.6	41.1

Similarly for prospectively undersampled data, the number of time points = 420 for each overlapping time block, and the patch-tensor size = $64\,(8*8)\times 10\times 42$. We used $S = 2$ outer iterations, $T = 11$ inner iterations for ADMM, and 4 iterations for the CG update of $\mathbf{Z}$. The number of iterations for regularized CG-SENSE reconstruction was 19. All the OSSI reconstructions were initialized with data-shared images.

Figure 3.4 shows reconstructions from mostly sampled data, the proposed patch-tensor LR, MLLR, GTLR, regularized CG-SENSE, and patch-tensor L+S models. The fast time image reconstructed using the proposed approach is less noisy compared to the mostly sampled reference and other reconstructions. The oscillatory patterns and the high-resolution details of the fMRI image (after 2-norm combination of the fast time images) are also well preserved. The difference maps after combination is presented in Fig. 3.19.

Figure 3.5 gives functional results including activation maps and tSNR maps. The proposed model enables high-resolution fMRI with larger activated regions than other undersampled reconstructions, and maintains the SNR advantage of OSSI with tSNR values that are comparable to the mostly sampled reconstruction. patch-tensor LR regularization and the patch-tensor L+S model present similar results, suggesting that L+S decomposition and Fourier sparsity along the two time dimensions were not critical given the patch-tensor modeling of the data.

The quality of the retrospectively undersampled reconstructions was further assessed with ROC analysis. ROC curves for the activation maps of different reconstruction approaches were compared with mostly sampled activation at the lower third of

the brain as ground truth. Figure 3.20 shows that the proposed approach leads to the largest area under the ROC curve.

Figure 3.6 presents prospectively undersampled reconstructions. Compared to OSSI regularized CG-SENSE reconstruction and standard GRE fMRI, the proposed approach yields more functional activity, less noisy time courses, and higher tSNR with the largely improved spatial and temporal resolutions. Other qualitative and quantitative comparisons for 2D prospectively undersampled reconstructions are in Fig. 3.23 and Table 3.3.

Table 3.1 summarizes quantities from different reconstructions including NRMSD for the whole dataset before and after fast time combination, number of activated voxels, and average tSNR within the brain. The proposed patch-tensor modeling outperforms other reconstruction methods with more functional activation and a high average tSNR.

Reconstruction comparisons of a different subject are presented in Figs. 3.26, 3.27, 3.28, and Table 3.6 for retrospectively undersampled data, and Fig. 3.29 and Table 3.6 for prospectively undersampled data.

3.5.3 3D OSSI to GRE Comparison

The 3D OSSI prospectively undersampled data were reconstructed using the proposed model with number of time points before combination = 120 for each non-overlapping time block. The patch-tensor size = $108\,(6 * 6 * 3) \times 10 \times 12$, and $\{\lambda_i\} = [1\,1\,2]$. Number of ADMM outer iterations $S = 2$, inner iterations $T = 11$, and number of CG iterations = 7 for every $\mathbf{Z}$ update. We used data-shared images to initialize each $\mathbf{X}_i$ and $\mathbf{Z}$. The multi-slice GRE data were reconstructed with regularized CG-SENSE with 19 CG iterations for each slice.

Figure 3.7 shows the activation maps of 3D OSSI and multi-slice GRE. The proposed tensor model almost fully recovers the high-resolution structures of the OSSI images with a factor of 10 acquisition acceleration, and presents larger activated regions than multi-slice Ernst angle GRE.

Figure 3.8 shows the 3D tSNR maps, where OSSI provides higher average tSNR than GRE. The OSSI acquisition combined with the proposed undersampling design and tensor model reconstruction enable high-resolution and high SNR fMRI.

Quantitatively as presented in Table 3.2, the proposed 3D OSSI tensor reconstruction improves the amount of functional activity and average tSNR within the brain

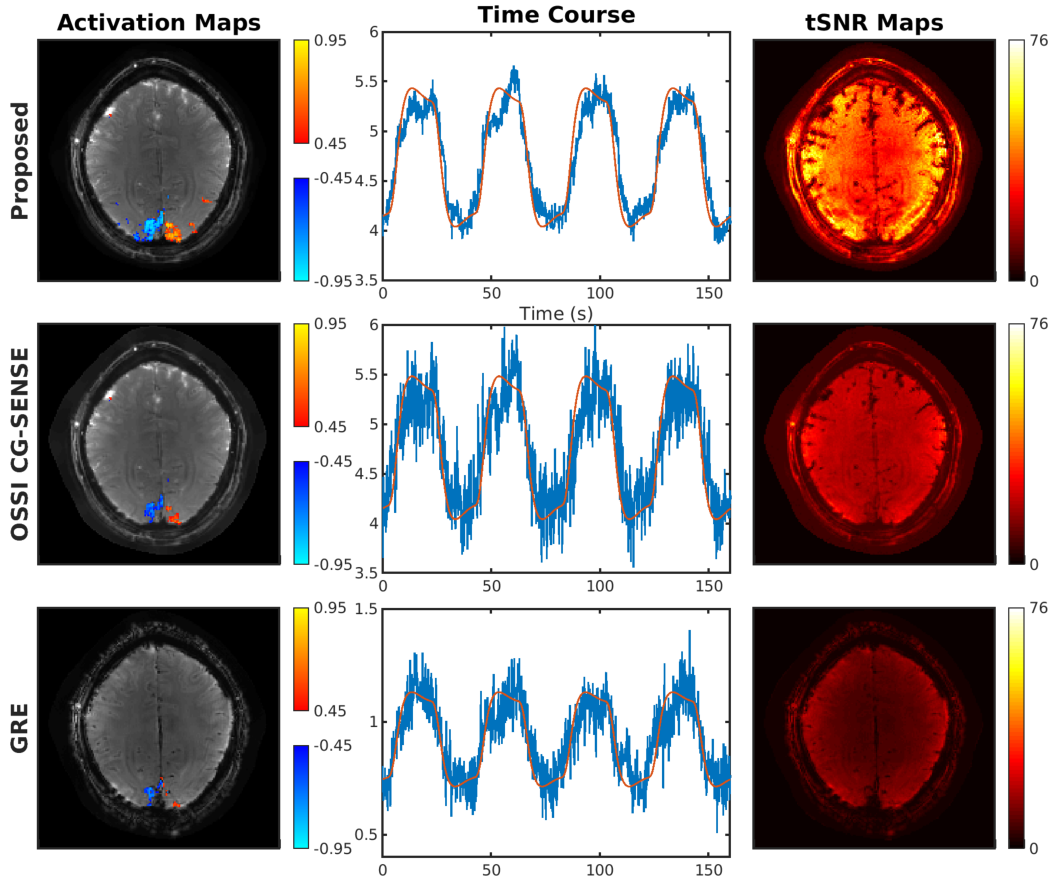

Figure 3.6: OSSI tensor model prospectively undersampled reconstruction demonstrating high-resolution and high SNR fMRI with high-resolution background and larger activated regions for the activation map, less noisy time course (red curve showing the reference waveform), and higher SNR for the temporal SNR map.

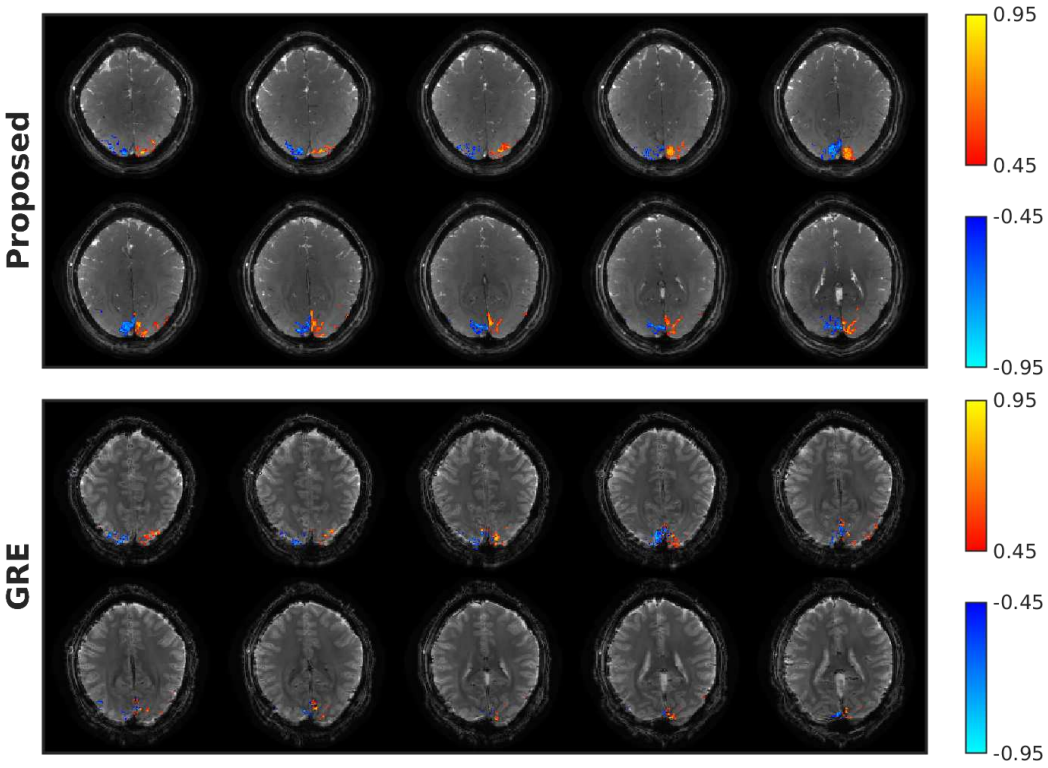

Figure 3.7: 3D OSSI (prospectively undersampled) and GRE activation maps of the central 10 slices. A contiguity (cluster-size) threshold of 2 was applied for the activated regions. With matched spatial and temporal resolutions, 3D OSSI acquired and reconstructed using the proposed method presents 2 times more activated voxels compared to multi-slice Ernst angle GRE imaging at TE = 30 ms.

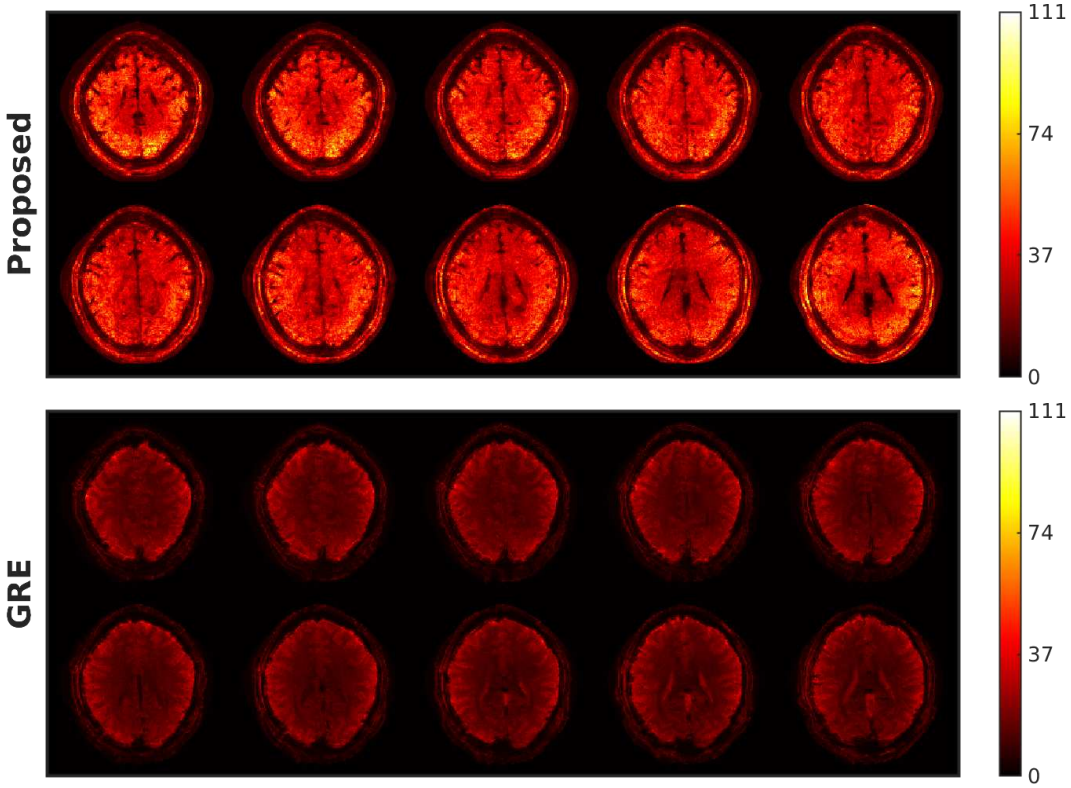

Figure 3.8: 3D OSSI (prospectively undersampled) and GRE temporal SNR maps of the central 10 slices. At the same spatial-temporal resolution, 3D OSSI acquired and reconstructed using the proposed method presents at least 2 times higher temporal SNR than standard multi-slice GRE imaging.

Table 3.2: Functional performances of proposed OSSI prospectively undersampled reconstruction and standard GRE imaging

	# Activated Voxels		Average tSNR	
	2D	3D	2D	3D
OSSI	322	2150	32.8	34.7
GRE	83	947	9.8	15.9
Ratio	3.9	2.3	3.3	2.2

by a factor of 2 more than standard GRE imaging at matched spatial and temporal resolutions.

3.6 Discussion

To our knowledge, the patch-tensor LR model is new for fMRI data. Reshaping and partitioning the data to patch-tensors facilitates exploiting high-dimensional structures, and considering all the unfoldings of the tensors better uses spatial-temporal low-rankness. Therefore, the model is flexible and adaptive to other high-dimensional image reconstruction problems that satisfy the patch-tensor LR constraints. Local models may be more valid than assuming low-rankness of the whole dataset.

Other reconstruction methods such as MLLR account for the locality of low-rank representations while treating the time dimension as a whole. GTLR separates the fast and slow time dimensions but enforces the low-rankness globally on the images. The proposed patch-tensor LR model combines the advantages of both methods by exploiting local low-rankness with two time dimensions, and improved the reconstruction and functional performances.

Another feature of the work is an incoherent sparse sampling scheme formed by properly rotating VD spirals along fast time and slow time. The angular dimension of the k-space can be mostly covered with different frames, and the trajectory is well accommodated with the spatial-temporal regularizers used here. Moreover, we noticed that for 3D undersampling, increasing number of interleaves in the central k_z planes greatly improves the amount of functional activation recovered and reduces

false positives. The sampling pattern is practical, and the prospective undersampling is easy to implement.

We selected and vectorized patches of spatial size 8×8 (2D) or $6 \times 6 \times 3$ (3D) based on the empirical reconstruction performance. The choice of spatial patch size is still an open question. At one extreme, the spatially global GTLR preserves little activation for 2D retrospectively undersampled reconstruction as presented in Fig. 3.5 and Table 3.1, but performs similar to the proposed method for 2D prospective undersampling as in Fig. 3.23 and Table 3.3. In both cases, GTLR used temporal patches.

We investigated multi-scale low-rank decomposition [81] with multi-scale patch-tensors of the OSSI images to explore the idea that different parts of the data may have different density and different low-rankness; however, it provided limited performance improvement and made the reconstruction more time-consuming. We also tested a 4D patch-tensor LR model with two spatial dimensions and two temporal dimensions. The cost function is the same as (3.2) without vectorizing spatial dimensions in $\mathcal{P}_m$. That model gave similar results as the 3D patch-tensor LR approach, making it well suited for potential applications such as GRE fMRI. The comparison results of the new models including functional maps, ROC curves, and quantitative evaluations are in Figs. 3.24, 3.25, and Table 3.4.

We imposed low-rankness on all the unfoldings of all the patch-tensors. However, some unfoldings of some patches are not very low-rank, especially for the second unfolding that is greatly affected by the nonlinear fast time oscillations. Therefore, nonlinear mapping approaches such as kernel methods or neural networks, that map the fast time data to a low-dimensional linear subspace [91], may further improve the model capacity, which might also help optimize combination of the OSSI fast time images instead of combing with 2-norm to yield band-free post-combined images. Because OSSI images are not very sparse in the Fourier domain, as shown in Figs. 3.11 and 3.12, the patch-tensor L+S reconstruction results in a very small sparse component seen in Fig. 3.22. Therefore, future work on adaptive sparsity [92] might be beneficial.

Because low-rank approaches might cause spatial-temporal smoothing that makes tSNR comparisons less compelling, we assessed and matched the amount of regularization for fast time image reconstructions based on their impulse responses. To evaluate spatial resolutions of the fMRI dynamics for different reconstructions after

combination, we compared spatial autocorrelations of the different correlation maps (at the center of the brain without activation). Figure 3.21 demonstrates that the proposed approach has similar autocorrelation profiles as the mostly sampled reconstruction and preserves fMRI spatial resolution. We also compared ROC curves of different approaches with varying activation thresholds; these curves are invariant to the degrees of freedom for performance evaluation. The effective degrees of freedom calculation for the nonlinear reconstructions will be explored in the future as in [93].

The proposed sparse sampling uses fast VD spirals with designed rotations along the two time dimensions to increase sampling incoherence for the spatial-temporal models. However, the sampling incoherence from VD spirals is limited by the shape of the spiral, and the non-Cartesian nature requires NUFFT that needs more computation than FFT for Cartesian sampling. More importantly, designing the sampling pattern according to reconstruction models can improve the performance [94, 95], so we will further explore joint optimization of the sampling pattern and the reconstruction model.

3.7 Conclusion

We proposed a novel fMRI reconstruction method based on patch-tensor low-rank for the oscillating nature of OSSI images. We also introduced an incoherent variable-density sampling pattern that is easy to implement, and retrospectively and prospectively undersampled the multi-coil data with less than 10% of the fully sampled k-space. By exploiting the inherent high-dimensional structure and local spatial-temporal low-rankness of OSSI images, the proposed model was able to recover high-resolution images and preserve functional signals compared to matrix local low-rank and tensor low-rank methods. It further enabled 3D high SNR fMRI with 2 times more functional activity and 2 times higher tSNR compared to standard GRE imaging.

3.8 Supporting Information

This supplemental material presents: (1) OSSI signal properties including example OSSI images and time courses before and after Fourier transform, and tensor low-rankness for patch-tensors at different regions of the brain; (2) the incoherent trajectory rotation schemes for both retrospective and prospective undersampling; (3) reconstruction details including effects of overlapping time blocks and regularization parameter selection based on impulse perturbation; (4) reconstruction comparisons for 2D retrospective and prospective undersampling; (5) other reconstruction methods including 4D patch-tensor low-rank and multi-scale tensor low-rank; (6) reconstruction results of a different subject.

3.8.1 OSSI Signal Properties

This section presents in-vivo OSSI images and time courses, and demonstrates local low-rankness of OSSI fMRI time-series. Fig. 3.9 shows 2 cycles of OSSI fast time images with periodic oscillation patterns. Fig. 3.10 provides example time courses from non-activated and activated ROIs of the OSSI images. Fig. 3.11 gives 1D Fourier transformed (along fast time) results for the complex time series corresponding to the images in Fig. 3.9, and Fig. 3.12 presents the Fourier transformed time courses of Fig. 3.10. OSSI images are not very sparse before or after Fourier transform due to the nonlinear oscillations. Fig. 3.13 gives log-scale singular value plots of non-activated and activated 3D patch-tensors from an OSSI fMRI time block.

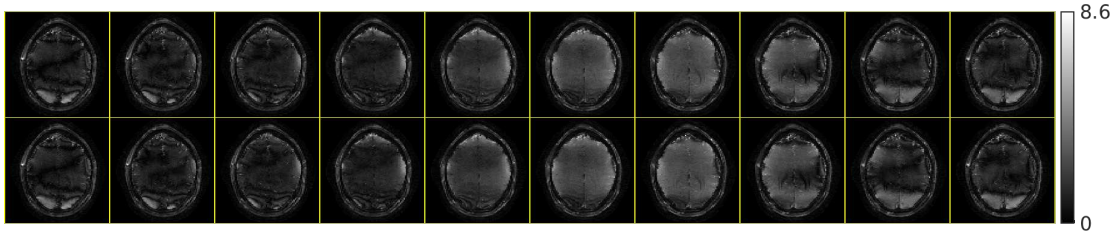

Figure 3.9: Example OSSI fast time magnitude images for 2 cycles of the periodic oscillations.

3.8.2 Incoherent Sampling Pattern

This section illustrates how the proposed spiral rotations help increase temporal incoherence for OSSI acquisition. For prospective undersampling, the baseline

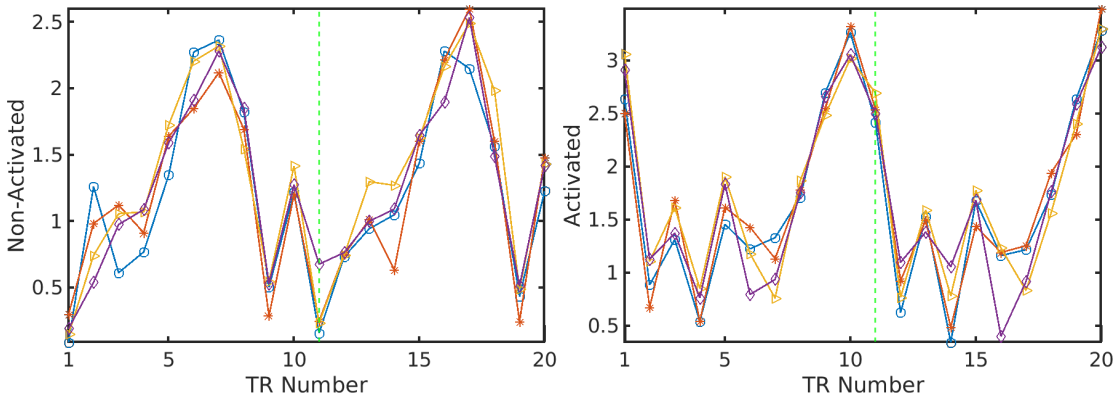

Figure 3.10: OSSI fast-time time courses (magnitudes) of 4 different voxels within a brain region that is not activated (left) or activated (right). The signal oscillation pattern repeats every $n_c = 10$ TRs, as indicated by the vertical green dashed line.

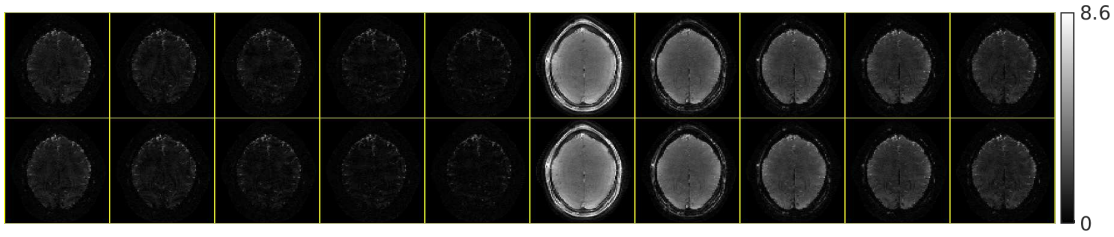

Figure 3.11: Results after taking 1D Fourier transform along fast time of the OSSI images shown in Fig. 3.9. Magnitude is shown and temporal frequency 0 is in "middle" (6th image from left). OSSI fast time images are not very sparse in the Fourier domain.

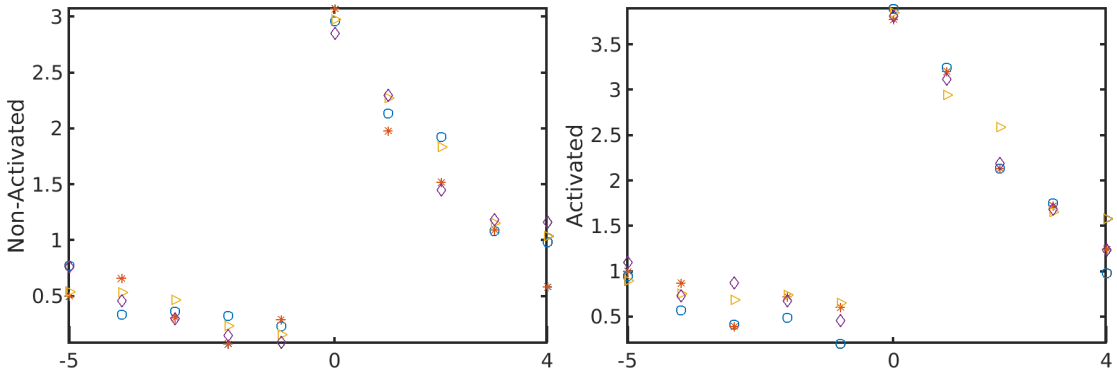

Figure 3.12: Results after taking 1D Fourier transform along fast time (every $n_c = 10$ TRs) of the OSSI time courses in Fig. 3.10. Magnitude of one cycle is shown and temporal frequency 0 is in "middle". OSSI fast time signals are not very sparse in the Fourier domain.

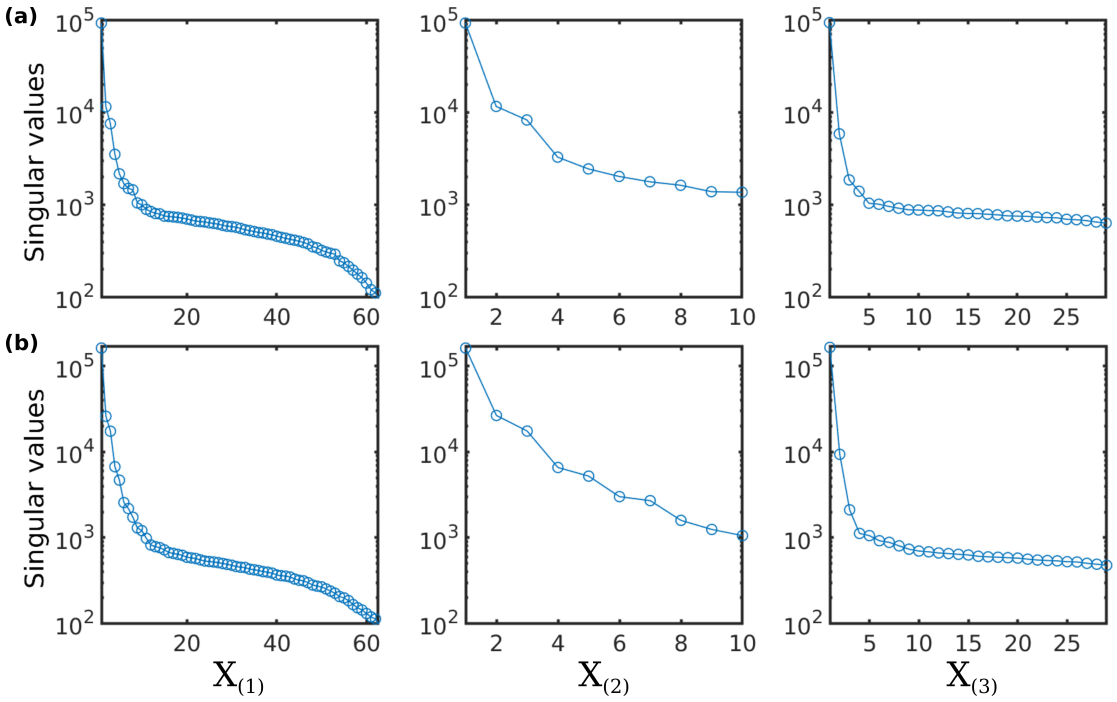

Figure 3.13: Log-scale singular value plots for all 3 unfoldings of a 3D patch-tensor (a) at the center of the brain with no activation (b) at the activation region. For both activated and non-activated patch-tensors, the unfoldings show a similar pattern that $X_{(3)}$ has lower rank than $X_{(1)}$ and $X_{(2)}$.

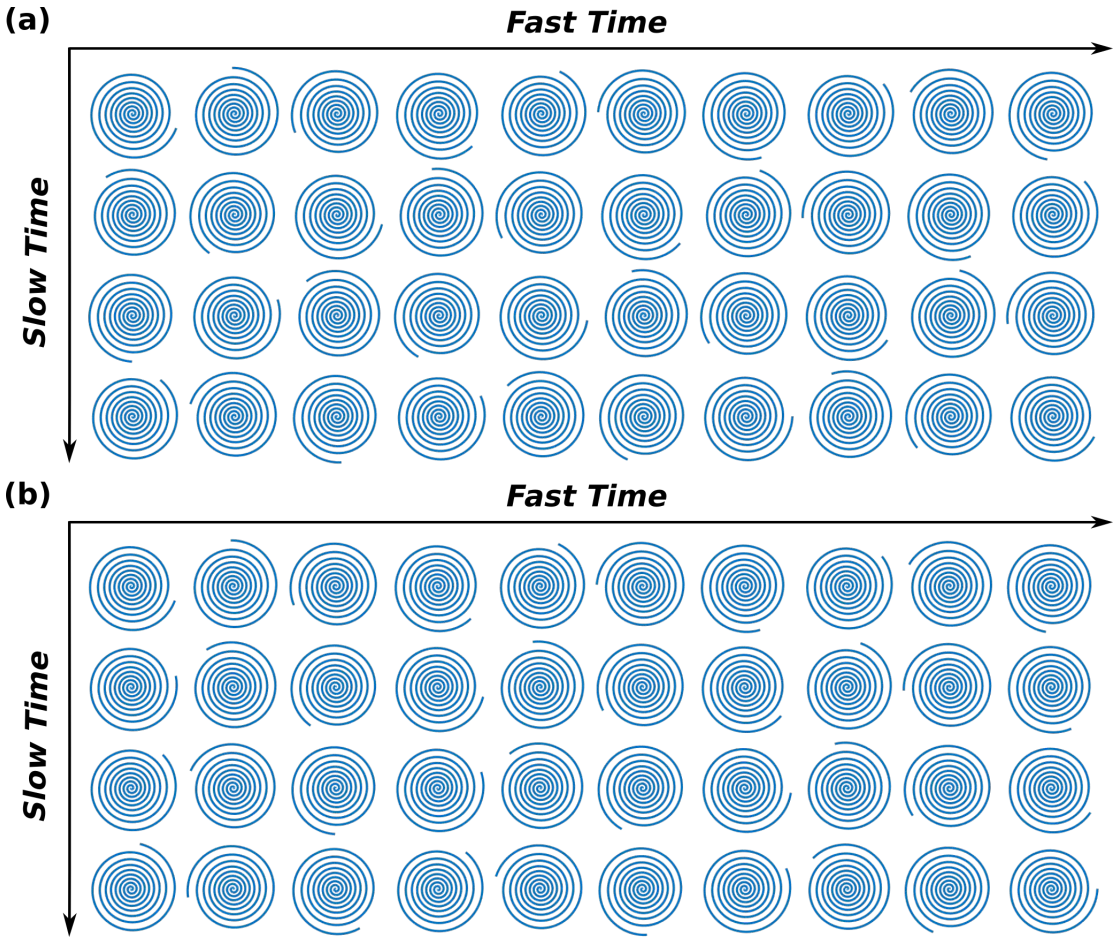

Figure 3.14: Demonstration of the incoherent rotations for 2D prospective undersampling. The proposed scheme of $ga \cdot k + ga \cdot \lfloor k/n_c \rfloor$ in (a) increases the sampling incoherence along slow time compared to a baseline rotation scheme of $ga \cdot k$ in (b).

rotation of $ga \cdot k$ for frame k leads to an angle difference of $10ga \bmod 360° = 32°$ between consecutive slow time points. With the additional angle of $ga \cdot \lfloor k/n_c \rfloor$, the angle difference becomes $11ga \bmod 360° = 144°$, which increases sampling incoherence along slow time as compared in Fig. 3.14. Similarly for retrospective undersampling, the angle difference between undersampled slow time points changes from $90ga \bmod 360° = -68°$ to $92ga \bmod 360° = 155°$ with improved incoherence as in Fig. 3.15.

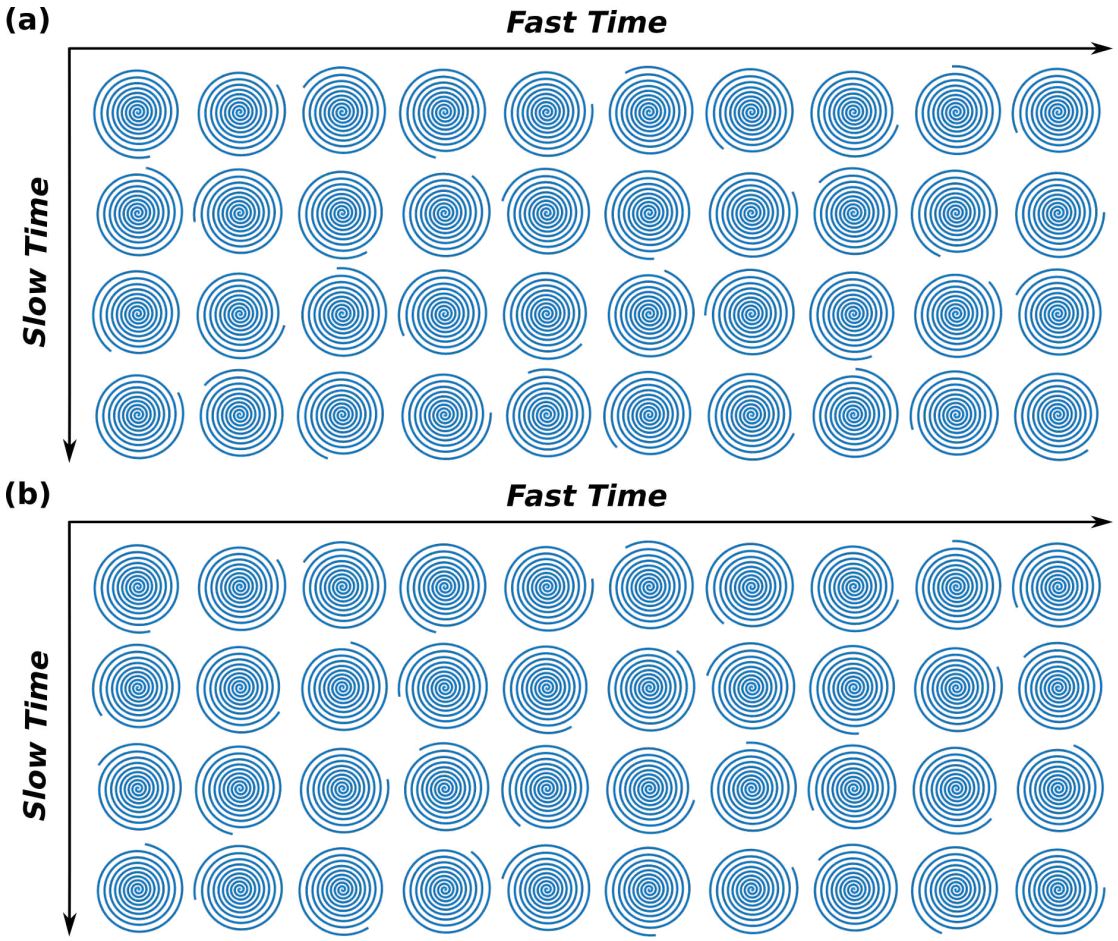

Figure 3.15: Demonstration of the incoherent rotations for 2D retrospective undersampling. The proposed scheme of $ga \cdot k + 2 \cdot ga \cdot \lfloor k/n_c/n_i \rfloor$ in (a) increases the sampling incoherence along slow time compared to a baseline rotation scheme of $ga \cdot k$ in (b).

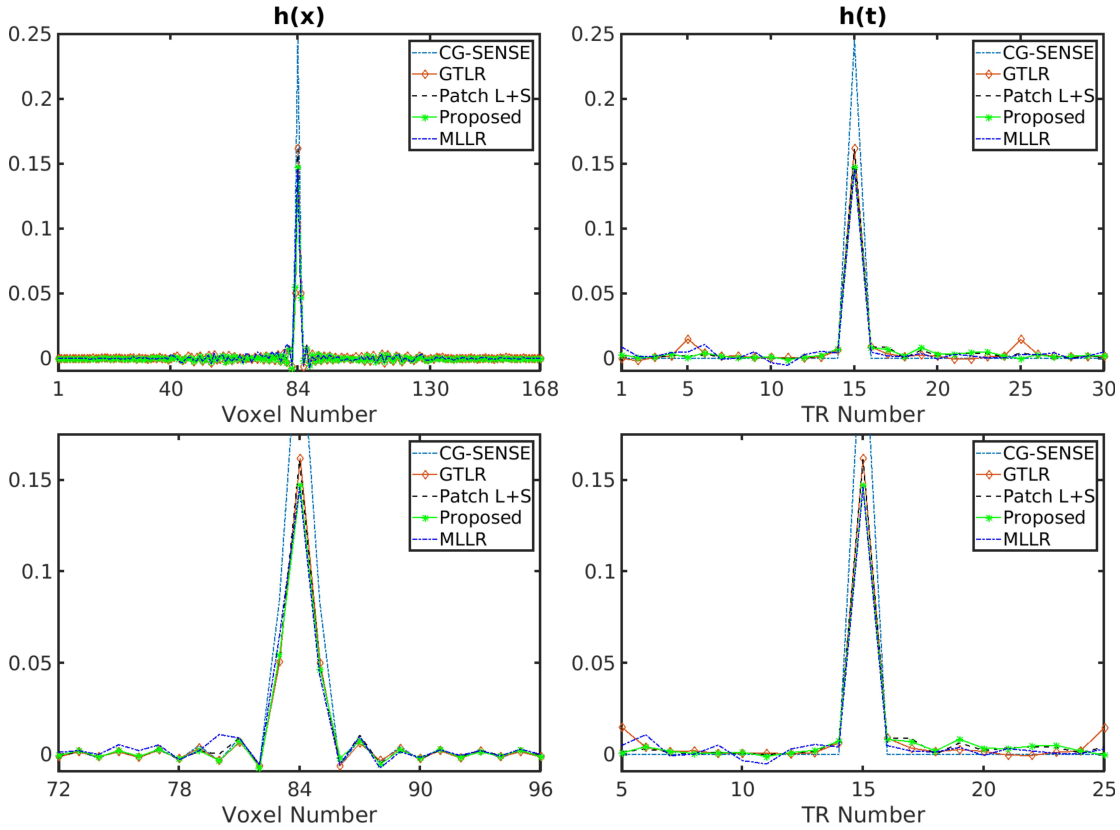

Figure 3.16: Impulse responses of different reconstructions along spatial dimension (left) and temporal dimension (right). Enlarging the central part of the impulse responses (bottom left and right) shows that impulse responses for different reconstruction models are of similar magnitudes and preserve spatial and temporal resolution with relatively small tails. Because the perturbation of $\delta(j,t)$ added to the image domain is real, and the imaginary parts of the impulse responses are small enough to be neglected, the real parts of the impulse responses are shown.

3.8.3 Reconstruction Adjustment

This section presents practical adjustments to the reconstruction methods including local impulse responses for regularization parameter selection and structuring overlapping time blocks for the OSSI fMRI time course.

3.8.3.1 Regularization Parameter Selection

The local impulse response profiles in Fig. 3.16 demonstrate that we have tuned the different reconstruction methods so that they are regularizing the data by similar amounts without excessive spatial or temporal smoothing.

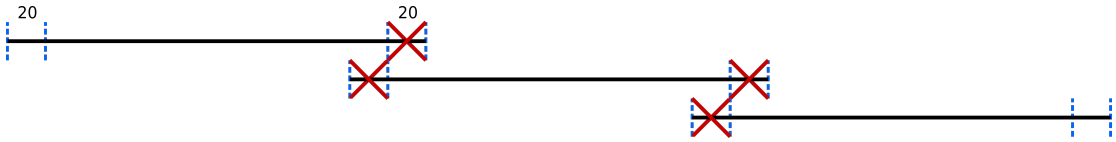

Figure 3.17: The OSSI fMRI time course is broken into overlapping time blocks of about 300 time points (denoted by black horizontal lines) for reconstruction. The overlapping portion of 20 time points at both ends of the time blocks (denoted by red crosses) are discarded after reconstruction except for the beginning and ending portions of the whole time series.

3.8.3.2 Overlapping Time Blocks

Fig. 3.17 illustrates ranges of overlapping time blocks and the formation of the entire reconstructed time course after discarding the overlapping portions. Fig. 3.18 compares activated time courses and spectra from reconstructions using non-overlapping time blocks or overlapping time blocks. With carefully adjusted regularization parameters, reconstructing overlapping blocks or non-overlapping blocks led to similar results.

3.8.4 Comparison and Results

This section presents additional reconstruction results for 2D retrospectively and prospectively undersampled data.

3.8.4.1 2D Retrospectively Undersampling

Fig. 3.19 shows difference maps of 2-norm combined reconstructions compared to the mostly sampled case. ROC curves for the activation maps of different reconstruction approaches in Fig. 3.20 shows that the proposed approach leads to the largest area under the ROC curve (AUC). Mostly sampled activation at the lower third of the brain was used as ground truth, and the activation threshold ranges from -0.1 to 0.99 with a 0.001 spacing. Fig. 3.21 presents autocorrelations of the correlation maps for different reconstructions. It verifies that the proposed approach preserves spatial resolution for fMRI. Fig. 3.22 shows the low-rank and sparse components (10 fast time points) of the patch-tensor low-rank plus sparse reconstruction. The sparse component is small and contains little information.

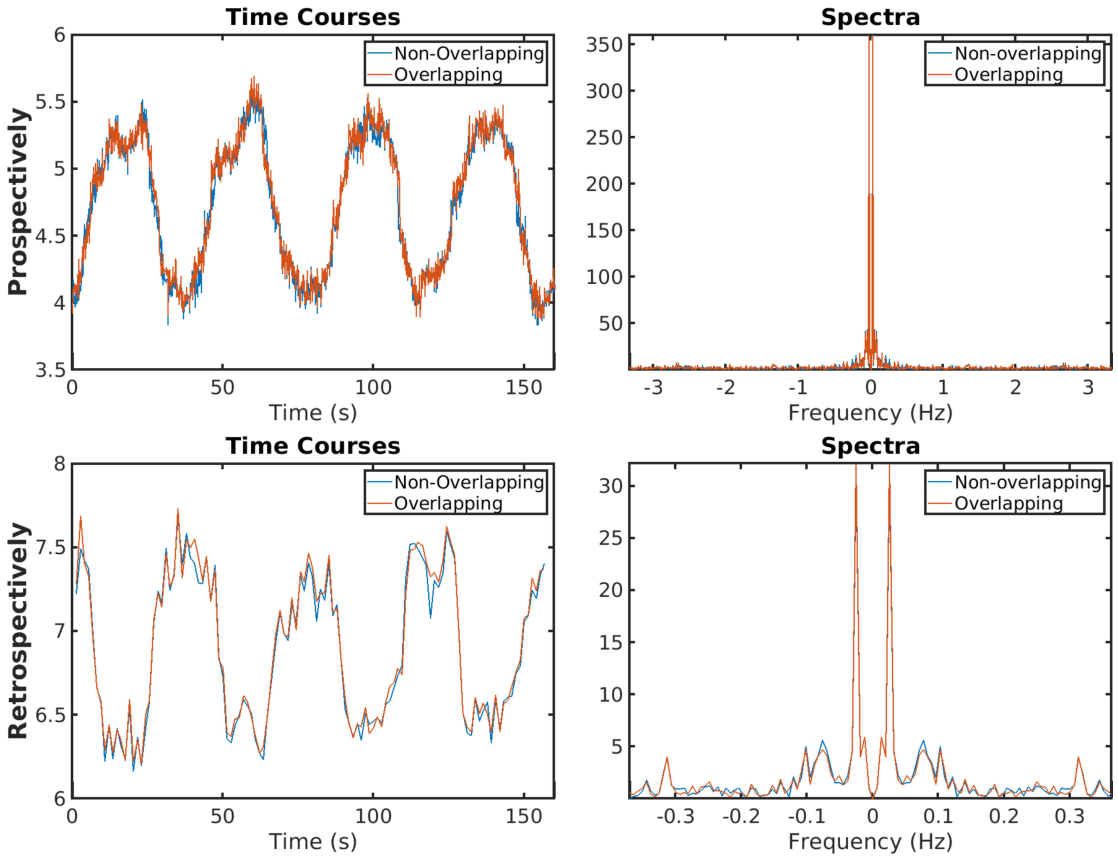

Figure 3.18: For both prospectively and retrospectively undersampled data, reconstructing overlapping time blocks or non-overlapping time of the whole OSSI fMRI time course leads to very similar time courses and spectra.

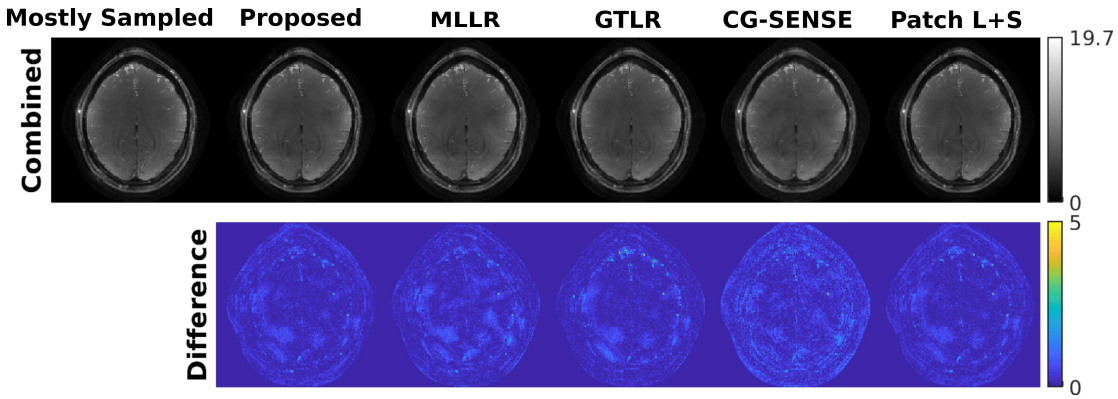

Figure 3.19: Reconstructed images and difference maps (compared to the mostly sampled reconstruction) of different models after 2-norm combination. The proposed approach presents less residual in the difference map.

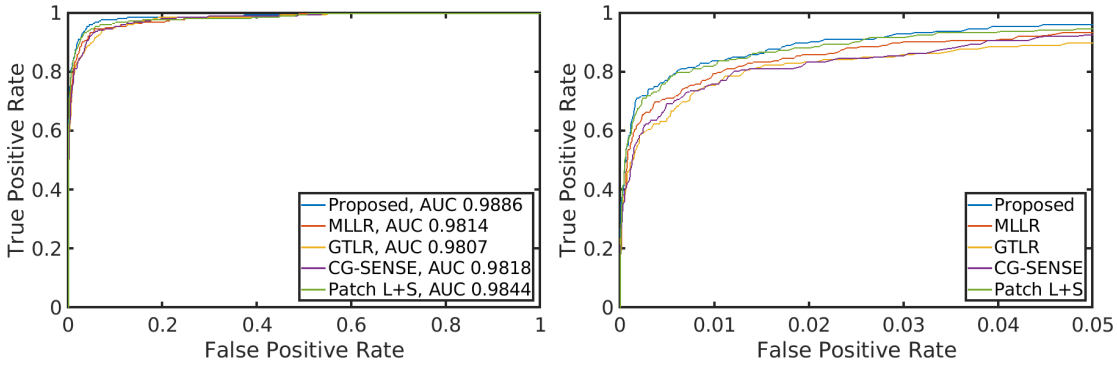

Figure 3.20: ROC curves of different reconstruction approaches with mostly sampled activation at the lower third of the brain as ground truth. The proposed method outperforms other approaches with the largest area under the ROC curve (left). The ROC curve of the proposed approach is also the closest to the top left corner, especially for the reasonable range with false positive rate less than 0.05 (right).

Table 3.3: Quantitative comparisons of OSSI 2D prospectively undersampled reconstructions

	Proposed	MLLR	GTLR	CG-SENSE	Patch L+S	GRE
# Activated Voxels	322	233	311	149	324	83
Average tSNR	32.8	25.6	32.1	18.2	32.4	9.8

3.8.4.2 2D Prospectively Undersampling

Fig. 3.23 and Table 3.3 give qualitative and quantitative results for 2D prospectively undersampled data reconstructed using patch-tensor LR, MLLR, GTLR, CG-SENSE, and patch-tensor L+S approaches with comparison to GRE fMRI. The patch-tensor LR, GTLR, and patch-tensor L+S models result in similar performances. The 2D prospectively undersampled data have better temporal resolution (by a factor of 9) than the 2D retrospectively undersampled data, which helps improve the quality of the data-shared initialization and thus the reconstructions.

3.8.5 4D Patch-Tensor and Multi-Scale Patch-Tensor Low-Rank Models

This section focuses on comparisons to other models including 4D patch-tensor low-rank and multi-scale patch-tensor low-rank. Instead of vectorizing the spatial

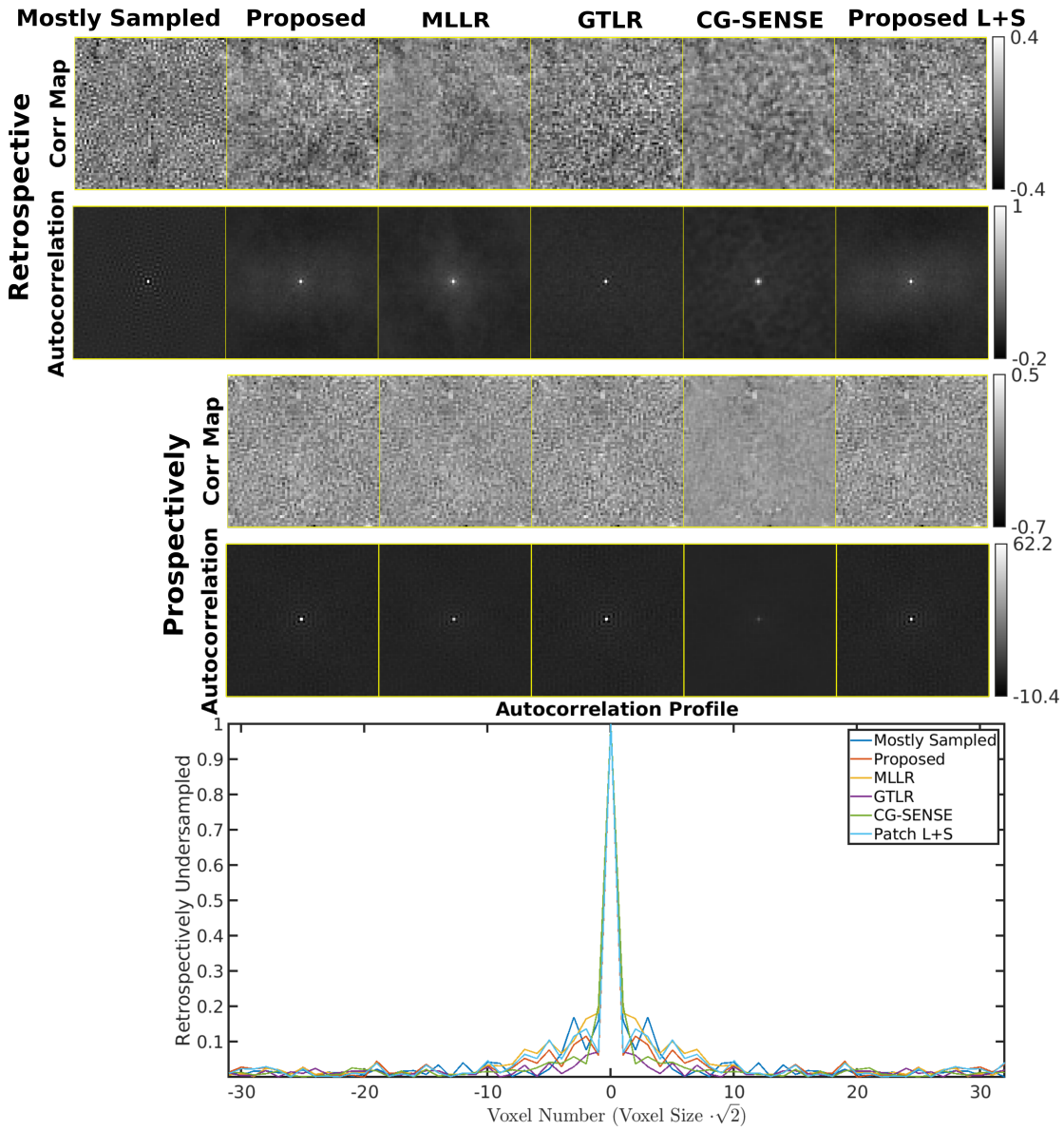

Figure 3.21: Correlation maps and normalized autocorrelations of the correlation map for the different reconstructions at the center of the brain without activation. The proposed model results in similar autocorrelation profiles along diagonal as the mostly sampled reconstruction.

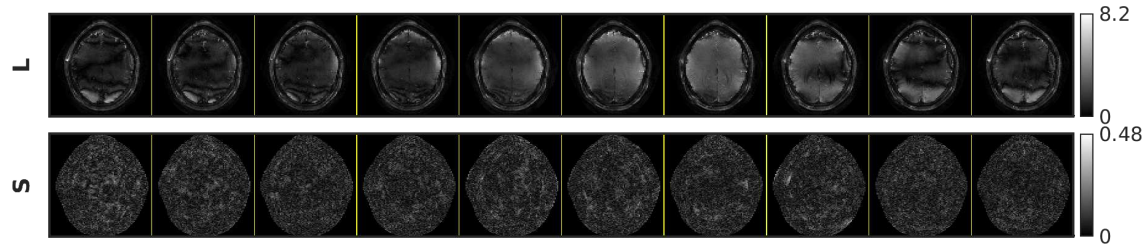

Figure 3.22: The low-rank and sparse components (first 10 fast time points) of the patch-tensor low-rank plus sparse reconstruction with 2D retrospectively undersampled data. The sparse component is very small and contain limited structural information.

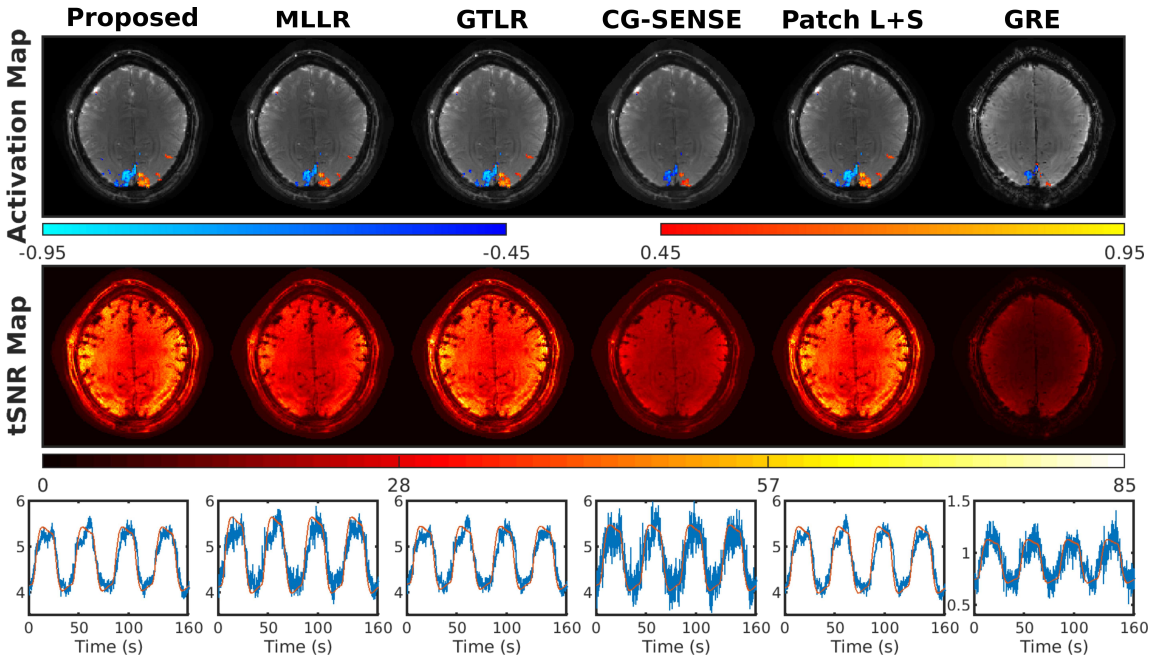

Figure 3.23: Activation maps, temporal SNR maps, and time courses in the activated regions from prospectively undersampled reconstructions and GRE fMRI. A contiguity threshold of 2 was applied for the activation maps. The patch-tensor low-rank, global tensor low-rank, and patch-tensor low-rank plus sparse reconstructions outperform other approaches with more functional activation and cleaner time courses.

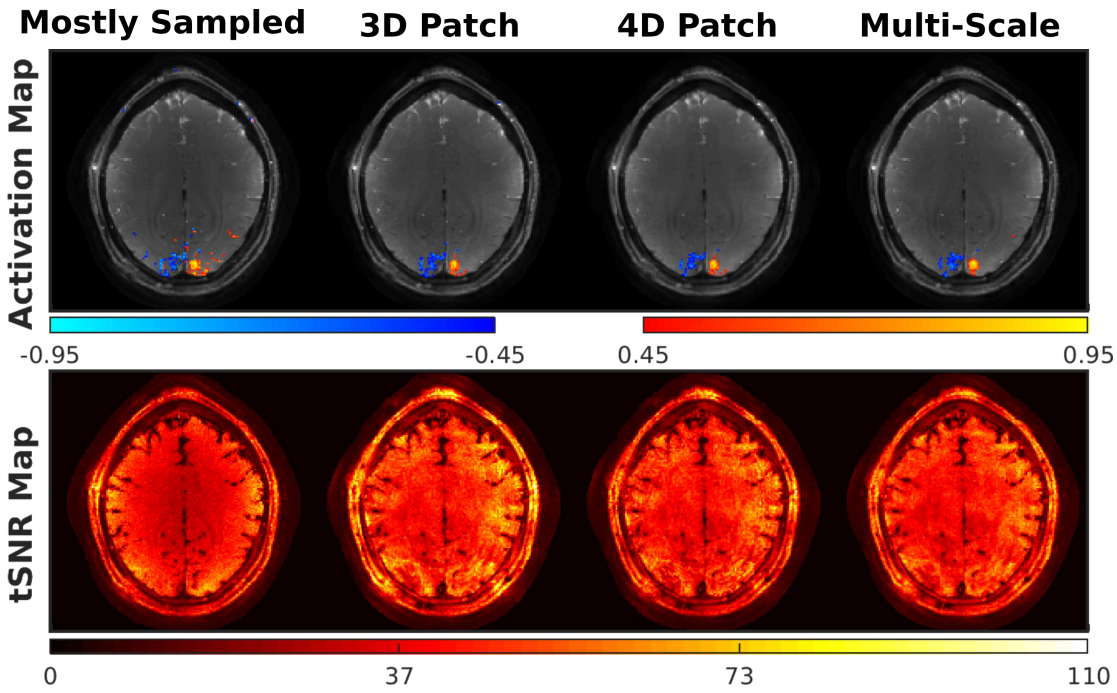

Figure 3.24: Activation maps and temporal SNR maps from retrospectively undersampled data and reconstruction models including the proposed 3D patch-tensor low-rank, 4D patch-tensor low-rank, and multi-scale tensor low-rank. A contiguity threshold of 2 was applied for the activated regions. All three approaches perform well with similar amounts of activation and temporal SNR.

Table 3.4: Quantitative comparisons of other OSSI 2D retrospectively undersampled reconstructions

	Mostly Sampled	3D Patch	4D Patch	Multi-Scale
NRMSD Before Comb	-	0.17	0.19	0.17
NRMSD After Comb	-	0.05	0.06	0.05
# Activated Voxels	229	168	145	146
Average tSNR	37.1	43.6	41.4	41.2

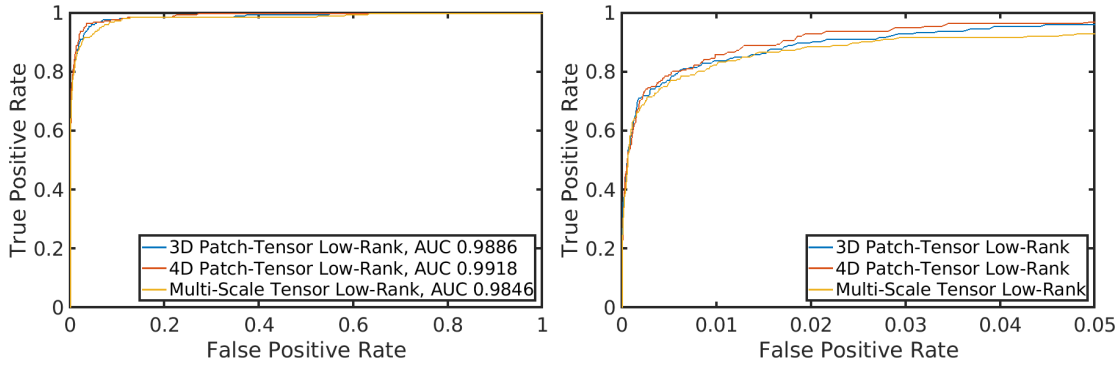

Figure 3.25: ROC curves of different reconstruction models including the proposed 3D patch-tensor low-rank, 4D patch-tensor low-rank, and multi-scale tensor low-rank. The activation of the mostly sampled data at the lower third of the brain is used as ground truth. All three models perform well with large areas under the ROC curve (left), and the ROC curve of the 4D patch-tensor low-rank model is slightly closer to the top left corner than other approaches, especially for the reasonable range with false positive rate less than 0.05 (right).

dimensions as for the proposed 3D patch-tensor low-rank, 4D (or 5D for 3D OSSI fMRI with 2 time dimensions) patch-tensor low-rank model keeps all the spatial dimensions of the tensor for imposing low-rank constrains. The cost function is the same as equation (2) without vectorization of spatial dimensions in $\mathcal{P}_m$. The cost function for the multi-scale low-rank model we tested can be expressed as

$$\arg\min_{\mathbf{x}} \sum_{n=1}^{3}\sum_{m=1}^{M_n}\sum_{i=1}^{3} \lambda_i \left\|\mathcal{P}_m(\mathbf{X}_n)_{(i)}\right\|_* + \frac{1}{2}\left\|\mathcal{A}\left(\sum\nolimits_{n=1}^{3}\mathbf{X}_n\right)-\mathbf{y}\right\|_2^2, \tag{3.15}$$

where $\mathbf{X}_n$ is composed of scale-n patch-tensors. Specifically, we imposed tensor low-rank on patches of different spatial dimension 4×4, 8, and 14. Here, $\mathcal{P}(\cdot)$ partitions and reshapes the input into M_n low-rank patch-tensors for different scale n. The regularization parameters for the new models were also selected based on their impulse responses with similar magnitudes to the 3D patch-tensor LR model.

All three models are of similar reconstruction and functional performance. Fig. 3.24 provides activation maps and tSNR maps of 3D patch-tensor LR, 4D patch-tensor LR, and multi-scale patch-tensor LR with comparison to the mostly sampled reconstruction. Quantitative evaluations including NRMSD and functional activation are in Table 3.4. Fig. 3.25 shows the ROC curves for the models.

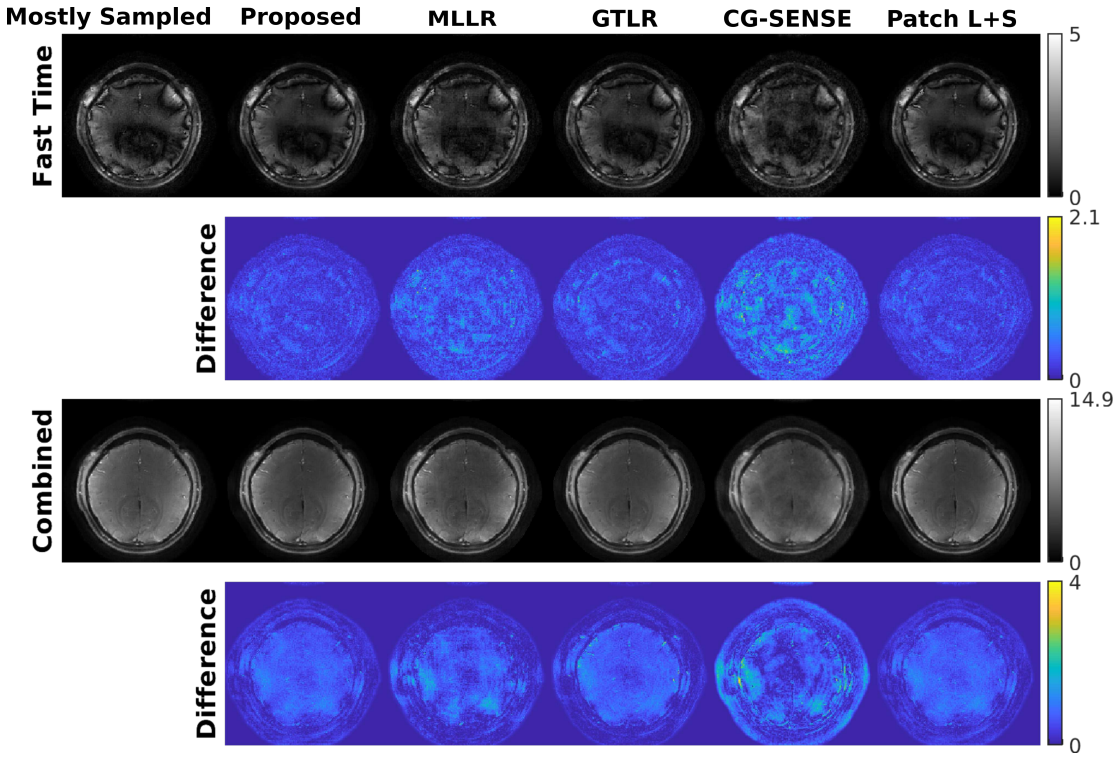

Figure 3.26: The retrospectively undersampled reconstructions of a different subject are compared to the mostly sampled results. The proposed approach outperforms other methods with less noisy fast time images and less structure in the difference maps before and after combination.

3.8.6 Other Subjects

This section presents 2D reconstruction results of a different subject. Both retrospectively and prospectively undersampled data were acquired with spiral-out trajectories. Retrospectively undersampled reconstruction results before and after 2-norm combination, and difference maps compared to the mostly sampled data are in Fig. 3.26. Fig. 3.27 presents functional activation maps and tSNR maps demonstrating that the proposed model outperforms other approaches with more activation. Table 3.5 summarises quantitative values of different reconstructions. Fig. 3.28 provides ROC curves of the activation maps. 2D prospectively undersampled reconstruction results including activation maps, tSNR maps, and example time courses are given in Fig. 3.29. Table 3.6 gives the corresponding quantitative evaluations.

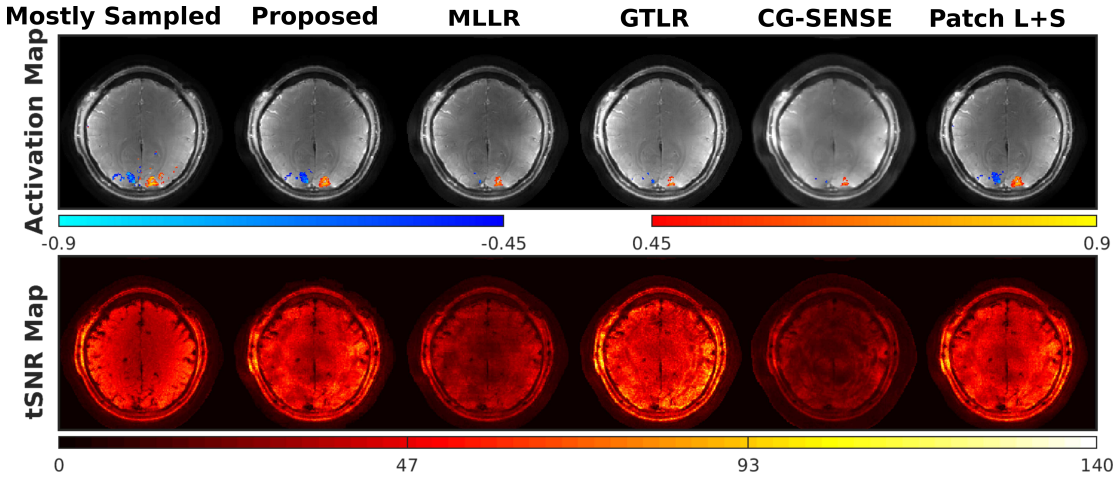

Figure 3.27: Activation maps and temporal SNR maps from retrospectively undersampled reconstructions of a different subject. A contiguity (cluster-size) threshold of 2 was applied for the activated regions. The proposed model provides more functional activation than other approaches and shows similar results as the patch-tensor low-rank plus sparse model.

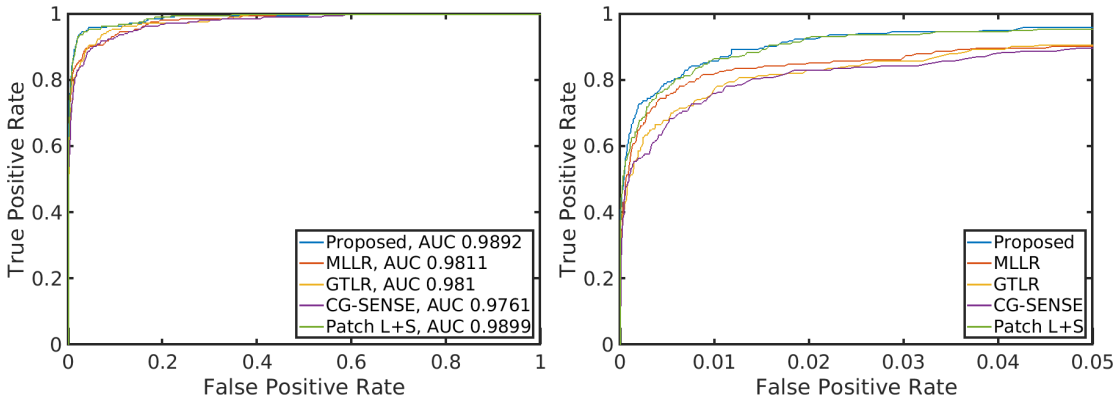

Figure 3.28: ROC curves for a different subject with mostly sampled activation at the lower third of the brain as ground truth. The proposed method outperforms other approaches with the largest area under the ROC curve (left). The ROC curve of the proposed approach is also the closest to the top left corner, especially for the reasonable range with false positive rate less than 0.05 (right).

Table 3.5: Retrospectively undersampled reconstructions of a different subject

	Mostly Sampled	Proposed	MLLR	GTLR	CG-SENSE	Patch L+S
NRMSD Before Comb	-	0.19	0.28	0.2	0.36	0.2
NRMSD After Comb	-	0.12	0.13	0.13	0.14	0.13
# Activated Voxels	225	166	52	48	34	164
Average tSNR	40.2	41	25.2	46.1	19	42.1

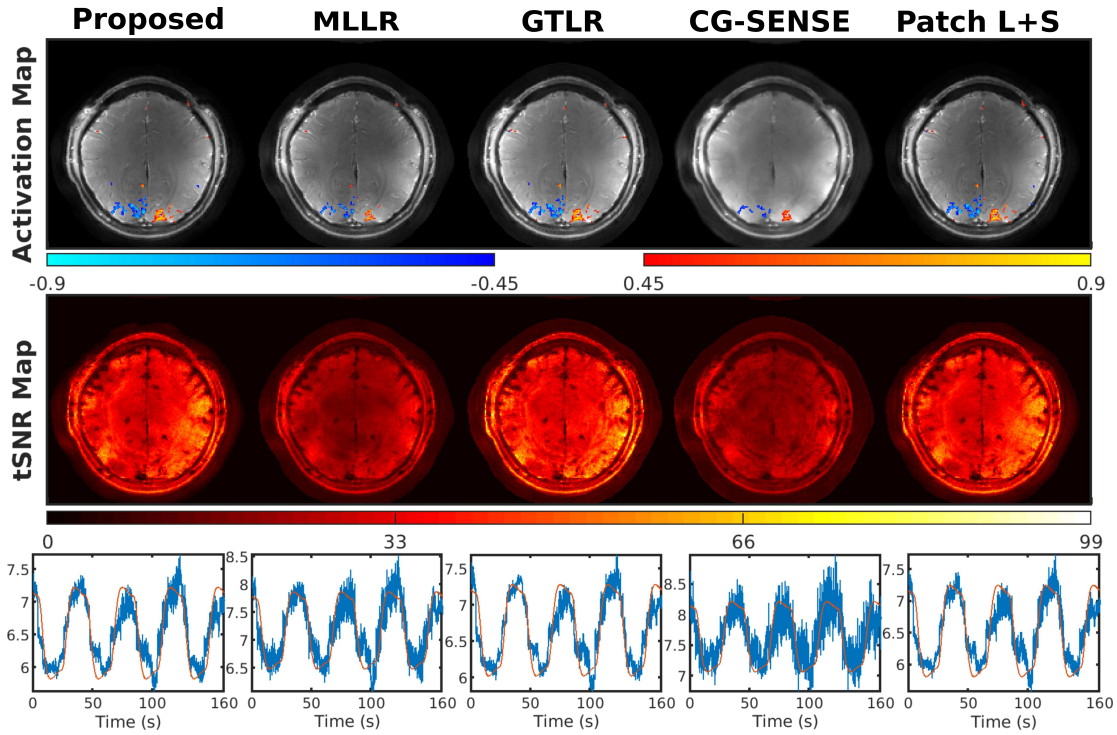

Figure 3.29: Activation maps, temporal SNR maps, and activated time courses from prospectively undersampled reconstructions of a different subject. A contiguity (cluster-size) threshold of 2 was applied for the activation maps. The patch-tensor low-rank, global tensor low-rank, and patch-tensor low-rank plus sparse reconstructions outperform other approaches with more functional activation and cleaner time courses.

Table 3.6: Prospectively undersampled reconstructions of a different subject

	Proposed	MLLR	GTLR	CG-SENSE	Patch L+S
# Activated Voxels	225	120	223	89	227
Average tSNR	33.5	21.1	34.9	20.6	34

CHAPTER IV

Manifold Model for High-Resolution fMRI Joint Reconstruction and Dynamic Quantification

In Chapter III, we exploited high-dimensional spatial-temporal similarities of OSSI fMRI time series using the patch-tensor low-rank model. The structured patch-tensor has one vectorized spatial dimension from a local patch and two time dimensions (fast and slow times). We noticed that due to the nonlinear oscillations in OSSI images, the unfolded matrix along fast time is not very low-rank compared to other unfoldings as presented in Fig. 3.2. This chapter focuses on OSSI fast time images, and aims to accurately model the nonlinearity of fast time signals with a manifold model. We compare the proposed manifold model to a subspace model that imposes matrix low-rankness on fast time images with global spatial and fast time dimensions.

OSSI is a recent fMRI acquisition method that exploits a large and oscillating signal, and can provide high SNR fMRI. However, the oscillatory nature of the signal leads to an increased number of acquisitions. To improve temporal resolution and accurately model the nonlinearity of OSSI signals, we build the MR physics for OSSI signal generation as a regularizer for the undersampled reconstruction rather than using subspace models that are not well suited for the data. Our proposed physics-based manifold model turns the disadvantages of OSSI acquisition into advantages and enables joint reconstruction and quantification. OSSI manifold model (OSSIMM) outperforms subspace models and reconstructs high-resolution fMRI images with a factor of 12 acceleration and without spatial or temporal resolution smoothing. Furthermore, OSSIMM can dynamically quantify important physics parameters, including R_2^* maps, with a temporal resolution of 150 ms. [1]

[1] This chapter is based on [20, 53, 96].

4.1 Introduction

Functional magnetic resonance imaging (fMRI) is an important tool for brain research and diagnosis. In its most common form, it detects functional activation by acquiring a time-series of MR images with blood-oxygen-level-dependent (BOLD) contrast [97]. However, the BOLD effect has a relatively low signal-to-noise ratio (SNR) [98], and the SNR further decreases with improved spatial resolution. Because the functional units (cortical columns) of the brain are on the order of 1 mm, high resolution with high SNR is critical for some fMRI experiments. This chapter focuses on Oscillating Steady-State Imaging (OSSI), a recent fMRI acquisition approach that provides higher SNR signals than standard gradient-echo (GRE) imaging [16].

The SNR advantage of OSSI comes at a price of spatial and temporal resolutions. OSSI acquisition requires a quadratic RF phase cycling with cycle length n_c (e.g., $n_c = 10$). The corresponding OSSI signal oscillates with a periodicity of $n_c \cdot$ TR, and the frequency-dependent oscillations result in oscillatory patterns in OSSI images. Therefore, every image in a regular fMRI time course is acquired n_c times with different phase increments in OSSI, and combining the n_c images eliminates oscillations for fMRI analysis. Acquiring n_c times more images compromises temporal resolution, and the short TR necessary for OSSI acquisition can limit single-shot spatial resolution.

To improve the spatial-temporal resolution, we previously used a patch-tensor low-rank model for the sparsely undersampled reconstruction [52]. While low-rank regularization fits data to linear subspaces, OSSI images are not very low-rank because of the nonlinear oscillations [53]. Instead of imposing low-rankness and/or sparsity that may or may not suit the data, this chapter proposes a nonlinear dimension reduction approach for OSSI reconstruction that uses a MR physics-based manifold as a regularizer, inspired by parameter map reconstruction methods for MR fingerprinting [99, 100].

As outlined in Fig. 4.1, the manifold model focuses on MR physics for OSSI signal generation. It represents n_c OSSI signal values per voxel by just 3 physical parameters, via Bloch equations. The nonlinear nature of the Bloch equations enables nonlinear representations of the data and nonlinear dimension reduction. We further introduce a near-manifold regularizer that encourages the reconstructed signal values to lie near the manifold. Compared to quantitative imaging works that enforce the reconstructed

images to be exactly equal to the physics-based representations [99, 100, 101, 102], the proposed near-manifold regularizer encourages the images to be near the manifold while also allowing for potential model mismatch.

Standard T_2^*-weighted magnitude images only assess relative signal changes due to BOLD effects and are not quantitative in terms of the blood oxygenation level, T_2^* or T_2' [103, 104, 105]. Quantifying T_2^* is important because of its sensitivity to iron concentration for disease monitoring [35]. By constructing a T_2' manifold based on BOLD-induced intravoxel dephasing, our work demonstrates the utility of the OSSI manifold model for dynamic quantification of T_2^*/R_2^*.

This chapter shows that the proposed T_2' manifold and near-manifold regularizer can jointly optimize OSSI images and quantitative maps. The manifold model enables high-resolution OSSI fMRI with 12-fold acquisition acceleration, outperforms low-rank regularization with more functional activation, and provides quantitative and dynamic assessment of tissue R_2^* maps and off-resonance f_0, with a temporal resolution of 150 ms.

4.2 OSSI Manifold Model (OSSIMM)

OSSI signal oscillates with a periodicity of n_cTR, and the OSSI fMRI time course contains n_c images for every image in a regular fMRI time series. We refer to the fast acquisition dimension of size n_c as "fast time" and the regular fMRI time dimension as "slow time" as presented in supplemental Fig. 4.10. OSSI fast time signals can have different shapes and change nonlinearly with respect to MR physics parameters, as illustrated in Fig. 4.2. To accurately model the nonlinear oscillations, we propose a MR-physics based manifold model for the undersampled reconstruction.

4.2.1 Physics-Based Manifold

In OSSI, the steady-state transverse magnetization of one isocromat at observation time t is

$$m_0\, \phi(t; T_1, T_2, f_0),$$

where $m_0 \in \mathbb{C}$ is the equilibrium magnetization, $\phi(\cdot) \in \mathbb{C}^{n_c}$ represents MR physics calculated by Bloch equations, T_1 and T_2 are tissue relaxation times, and f_0 denotes central off-resonance frequency from B_0 field inhomogeneity.

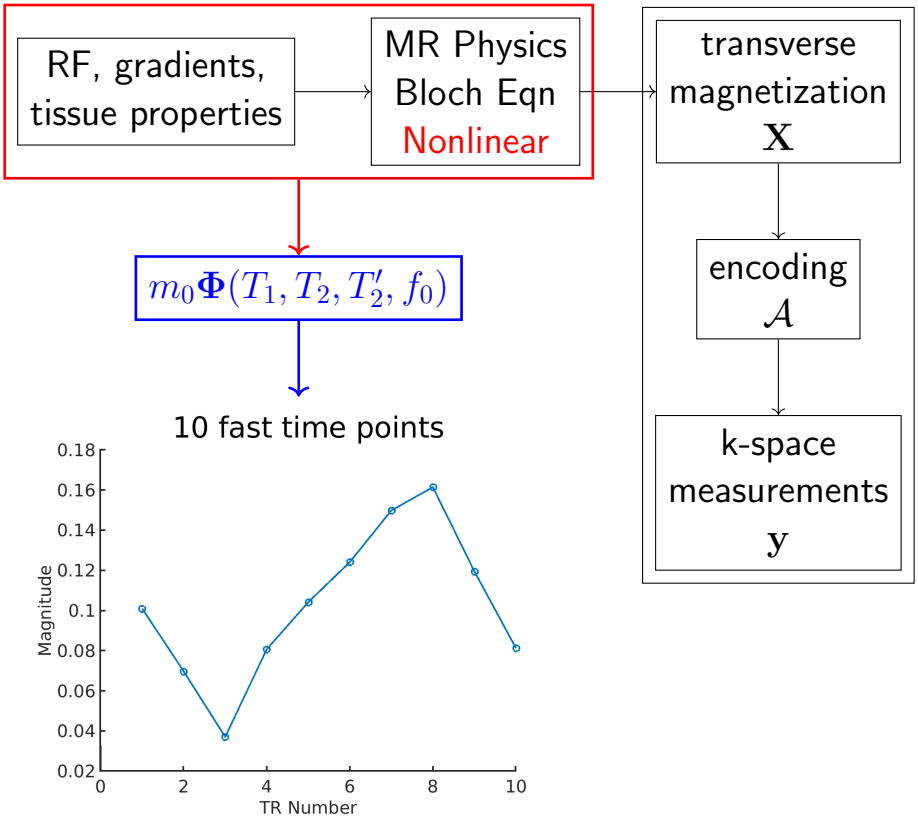

Figure 4.1: The proposed manifold model uses the MR physics for signal generation as a regularizer for the undersampled reconstruction.

T_2'-weighted OSSI signal in a voxel with an intra-voxel spreading of off-resonance frequencies f can be modeled as:

$$m_0\mathbf{\Phi}(t; T_1, T_2, T_2', f_0) = \int m_0\phi(t; T_1, T_2, f_0 + f)\, p(f; T_2')\, \mathrm{d}f\,. \tag{4.1}$$

The T_2' exponential decay corresponds to a Cauchy distribution for f with a probability density function (PDF) $p(f) = \gamma/\pi(\gamma^2 + f^2)$, and scale parameter $\gamma = 1/(2\pi T_2')$.

The isocromat signal at time $t > 0$ presents increased T_2 decay and increased off-resonance dephasing due to field inhomogeneity and BOLD-related field changes,

$$m_0\phi(t; T_1, T_2, f_0) = m_0\phi(t = 0; T_1, T_2, f_0)\, \mathrm{e}^{-t/T_2}\, \mathrm{e}^{-\imath 2\pi f_0 t}\,, \tag{4.2}$$

where $t = 0$ denotes the time right after the excitation.

As OSSI TR is relatively short (e.g., TR = 15 ms), we neglect the intravoxel dephasing during the readout and approximate the signal at $0 \leq t \leq \mathrm{TR}$ with the signal at the echo time TE. The T_2'-weighted signal becomes

$$m_0\mathbf{\Phi}(T_1, T_2, T_2', f_0) \approx \int m_0\phi(\mathrm{TE}; T_1, T_2, f_0 + f)\, \mathrm{e}^{-\mathrm{TE}/T_2}\, \mathrm{e}^{-\imath 2\pi(f_0+f)\mathrm{TE}}\, p(f; T_2')\, \mathrm{d}f\,. \tag{4.3}$$

Accordingly, T_2'-weighted OSSI fast time signals lie on the physics-based manifold:

$$\{m_0\mathbf{\Phi}(T_1, T_2, T_2', f_0) \in \mathbb{C}^{n_c} : m_0 \in \mathbb{C},\, T_1, T_2, T_2', f_0 \in \mathbb{R}\}, \tag{4.4}$$

The manifold maps a limited number of physics parameters to the n_c-dimensional oscillating signals via MR physics.

4.2.2 Near-Manifold Regularization

The physics-based manifold models the generation of MR signals, enables nonlinear dimension reduction, and can be an accurate prior for the undersampled reconstruction. Because the physics parameters are location dependent, and because OSSI signal values change drastically with varying parameters as shown in Fig. 4.2, we model the fast time signals in a voxel-by-voxel manner. Furthermore, to account for potential mismatches due to model simplifications and nonidealities in experiments (e.g., flip angle inhomogeneity), we propose a near-manifold regularizer that encour-

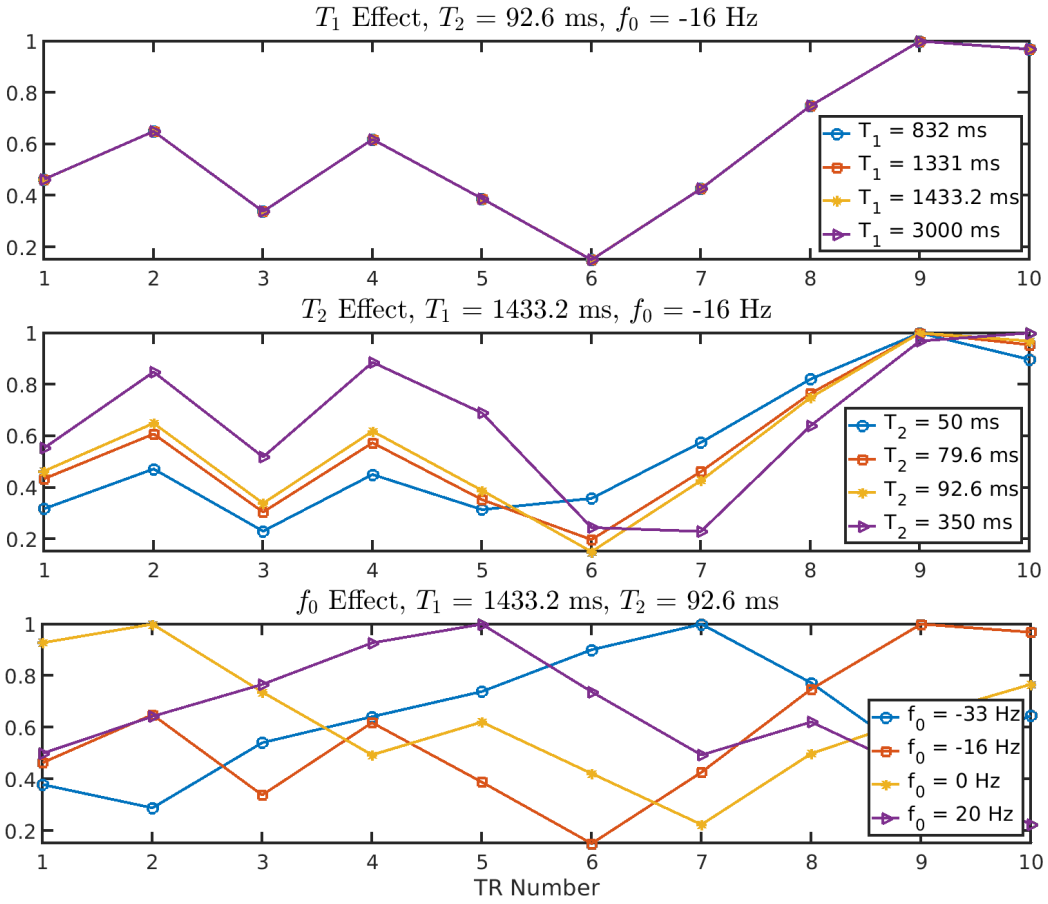

Figure 4.2: Normalized OSSI fast time signal magnitude for one isocromat with nonlinear oscillations determined by physics parameters T_2 and f_0. The change of T_1 only scales OSSI signal values.

ages the signal values in each voxel to be close to the manifold estimates but not necessarily exactly the same.

The proposed T_2' manifold-based image reconstruction problem uses the following optimization formulation:

$$\begin{aligned}\hat{\mathbf{X}} &= \arg\min_{\mathbf{X}} \tfrac{1}{2}\|\mathcal{A}(\mathbf{X}) - \mathbf{y}\|_2^2 + \beta \textstyle\sum_{n=1}^{N} \mathcal{R}\left(\mathbf{X}[n,:]\right), \\ \mathcal{R}(\mathbf{v}) &= \min_{m_0, T_2', f_0} \|\mathbf{v} - m_0 \mathbf{\Phi}(T_2', f_0; T_1, T_2)\|_2^2,\end{aligned} \tag{4.5}$$

where $\mathbf{X} \in \mathbb{C}^{N \times n_c}$ denotes n_c fast time images to be reconstructed. The vectorized spatial dimension N is N_{xy} for 2D OSSI fMRI. $\mathcal{A}(\cdot)$ is a linear operator consisting of coil sensitivities and the non-uniform Fourier transform including undersampling, $\mathbf{y}$ represents sparsely sampled k-space measurements. β is the regularization parameter. $\mathbf{v} \in \mathbb{C}^{n_c}$ is a vector of fast time signal values for each voxel in $\mathbf{X}$, $m_0\mathbf{\Phi}(T_2', f_0; T_1, T_2) \in \mathbb{C}^{n_c}$ denotes the manifold estimates. The regularizer minimizes the Euclidean distance between $\mathbf{v}$ and $m_0\mathbf{\Phi}(T_2', f_0; T_1, T_2)$. T_1 and T_2 are not directly estimated by the model. T_1 has a signal scaling effect that can be absorbed in m_0, as illustrated in Fig. 4.2. Section 4.3 describes the choices of baseline T_2 values for T_2^* estimation.

The voxel-wise parametric regularizer $\mathcal{R}(\mathbf{v})$ not only performs regularization for the ill-posed reconstruction problem, but also involves parameter estimation and can provide quantitative maps for T_2' and f_0.

4.2.3 Optimization Algorithm

To solve (4.5), we alternate between a regularization update and a data fidelity update for the reconstruction. The minimization of the voxel-wise parametric regularizer is a nonlinear least-square problem that we solve using the variable projection (VARPRO) method [106, 107]. Let $\theta = [T_2', f_0]$ denote the two nonlinear tissue parameters; the calculation of θ using VARPRO simplifies to

$$\hat{\theta} = \arg\max_{\theta} \frac{\left|\mathbf{\Phi}(\theta)'\mathbf{v}\right|^2}{\|\mathbf{\Phi}(\theta)\|_2^2}, \tag{4.6}$$

where $\mathbf{v} = \mathbf{X}[:, n] \in \mathbb{C}^{n_c}$. Instead of solving (4.6) for the explicit and sophisticated $\mathbf{\Phi}(\theta)$, we construct a dictionary consisting of discrete $\mathbf{\Phi}(\theta)$ realizations with varying θ parameters using Bloch simulations, and then perform grid search to find $\hat{\theta}$ for which

$\mathbf{\Phi}(\hat{\theta})$ best matches $\mathbf{v}$.

Updating m_0 is a least-squares problem with closed-from solution:

$$\hat{m}_0 = \frac{\mathbf{\Phi}(\hat{\theta})' \mathbf{v}}{\|\mathbf{\Phi}(\hat{\theta})\|_2^2}. \tag{4.7}$$

We parallelize the regularization update across different voxels.

The update step for $\mathbf{X}$ involves a quadratic least-squares problem that we solve using the conjugate gradient method as implemented in the Michigan Image Reconstruction Toolbox [44]. This data fidelity update is easily parallelized over different fast time images or different fast time images sets to speed up the fMRI time series reconstruction.

4.2.4 Comparison Method

We compare the manifold approach to a low-rank reconstruction approach that models the fast time signals using linear subspaces. The cost function for this low-rank comparison method is

$$\hat{\mathbf{X}} = \arg\min_{\mathbf{X}} \tfrac{1}{2}\|\mathcal{A}(\mathbf{X}) - \mathbf{y}\|_2^2 + \alpha\|\mathbf{X}\|_* \tag{4.8}$$

where $\mathbf{X} \in \mathbb{C}^{N \times n_c}$ represents every n_c fast time images, and α is the regularization parameter. We solve the optimization problem (4.8) using the proximal optimized gradient method (POGM) with adaptive restart [108, 109, 110].

4.3 Simulation Investigations

We generated OSSI signals via Bloch simulation using pulse-sequence parameters that matched the actual data acquisition. We used TR = 15 ms, TE = 2.7 ms (spiral-out trajectory), RF excitation pulse length = 1.6 ms, quadratic RF phase cycling with $\Phi(n) = \pi n^2/n_c$ for nth TR, $n_c = 10$, and flip angle = 10° [16].

4.3.1 OSSI Signals

The OSSI signal $\in \mathbb{C}^{n_c}$ for one isocromat is determined by physics parameters T_1, T_2, and f_0. Fig. 4.2 presents example OSSI isocromat signals (normalized by the

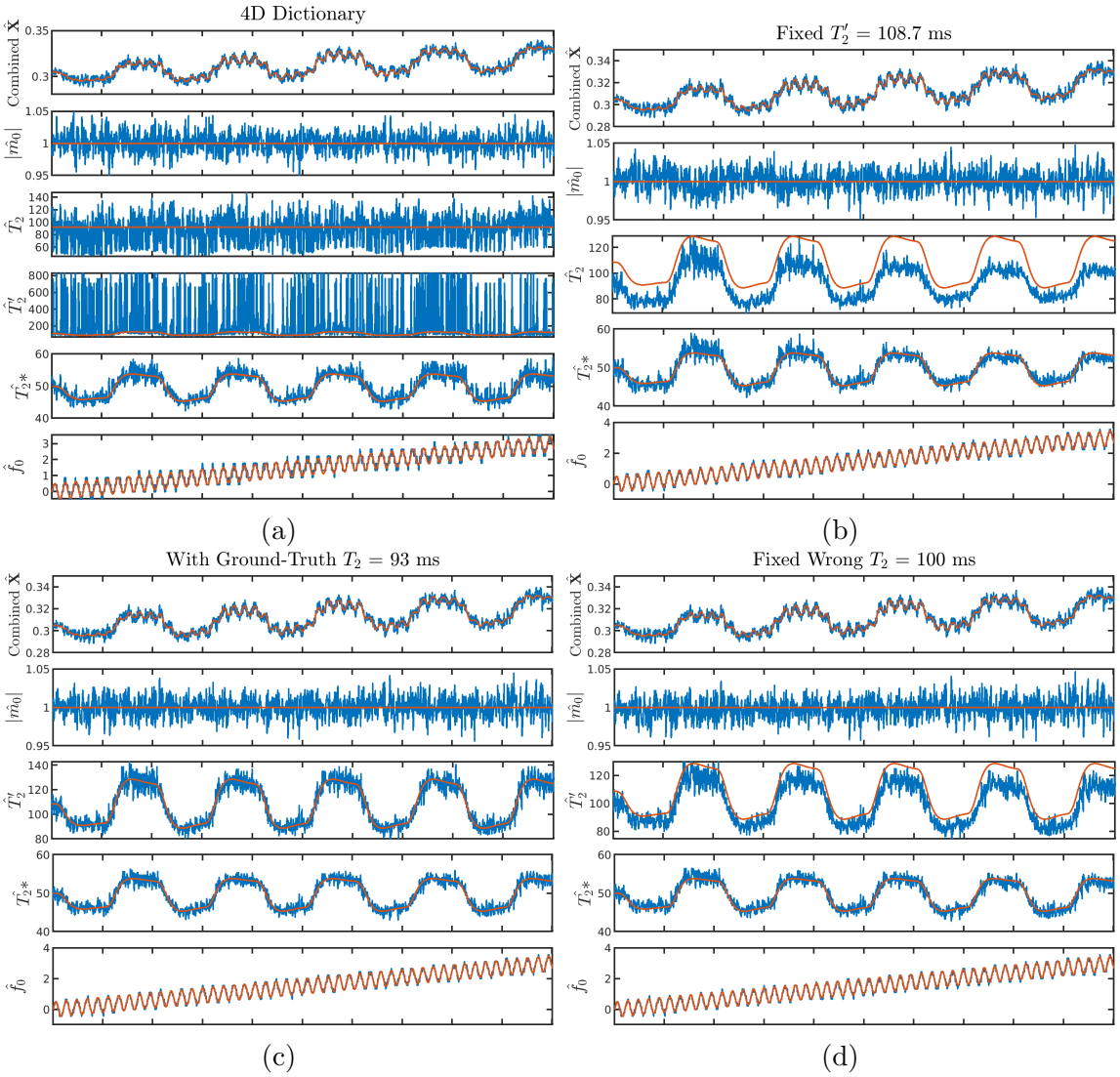

Figure 4.3: Quantification results for a simulated OSSI fMRI voxel using the manifold model with 4 different choices of the manifold. Because T_2 and T_2' effects to OSSI signals are correlated (Fig. 4.3a), and a T_2 manifold is not good enough for capturing BOLD-induced T_2' changes (Fig. 4.3b), we use a T_2' manifold for quantification. We can estimate T_2^* and T_2' with known T_2 values (Fig. 4.3c), or use a biased guess of T_2 for quantifying T_2^* (Fig. 4.3d).

maximum magnitude) with varying physics parameters selected based on gray matter relaxation parameters: $T_1 = 1400$ ms, $T_2 = 92.6$ ms [36]. As an approximation of (4.3), we simulated T_2'-weighted OSSI signal in a voxel with Riemann sum of numerous OSSI isocromat signals at different off-resonance frequencies. Specifically, we calculated a weighted sum of OSSI signals from 4000 isocromats at off-resonance frequency $f_0 + f$, where f uniformly ranged from -200 Hz to 200 Hz, and the weighting function was the PDF of the Cauchy distribution.

We further simulated a fMRI time course for one voxel with time-varying T_2' values. The T_2' waveform is the convolution of the canonical hemodynamic response function (HRF) [45] and the fMRI task waveform. Because fMRI percent signal change $\Delta\% \approx \Delta R_2' \cdot \mathrm{TE}_{\mathrm{eff}}$ [46] and OSSI $\mathrm{TE}_{\mathrm{eff}} = 17.5$ ms [16], we set $\Delta T_2' = 15.4$ ms to produce a typical percent signal change of 2%. The fMRI time course is also affected by scanner drift and respiration induced f_0 changes. We simulated f_0 with a linearly increasing scanner drift of about 1 Hz per minute and a sinusoidal waveform (magnitude of 0.5 Hz and period of 4.2 s) to model the respiratory changes. We also added complex Gaussian random noise for a typical temporal SNR (tSNR) value of 38 dB.

4.3.2 Dictionary Selection

We represented OSSI manifold using a signal dictionary, and each dictionary atom is a point on the manifold. Because T_2, T_2', and f_0 affect OSSI signals in different ways while T_1 has a scaling effect, we constructed a 4D dictionary by varying T_2, T_2', f_0, for $T_1 = 1400$ ms. The T_2 grids were in the 40 to 150 ms range with a 1 ms spacing. The T_2' grids were calculated by uniformly changing R_2^* from 12 to 38 Hz [111] with a step size of 0.1 Hz and a fixed T_2 of 92.6 ms. We set central off-resonance frequency f_0 to [-33.3,33.3] Hz with a 0.22 Hz spacing as OSSI signals are periodic with off-resonance frequency period = 1/TR = 66.7 Hz [16].

We reconstructed the functional signal and physics parameters from the simulated noisy fMRI time courses using the near-manifold regularizer in (4.5) and the 4D dictionary. The reconstructions were performed by (a) simultaneously estimating T_2 and T_2' using the 4D dictionary, (b) assuming T_2' is fixed and estimating T_2 using the 3D subset of the 4D dictionary based on the assumed T_2' value, (c) estimating T_2' with the actual T_2 value and the corresponding 3D dictionary, (d) assuming T_2 is fixed and estimating T_2' with a biased T_2 value and the corresponding 3D dictionary.

As shown in Fig. 4.3, because of the strong coupling between T_2 and T_2' values, it is infeasible to simultaneously estimate T_2 and T_2' (see Fig. 4.3a). Using a biased T_2' value for T_2 estimation (Fig. 4.3b) or a biased T_2 value for dynamic T_2' estimation (Fig. 4.3d) results in noticeable bias, whereas Fig. 4.3c presents accurate $\hat{T}_2'$ when the ground truth T_2 is provided. However, all the different estimation approaches lead to relatively good T_2^* estimates. Because m_0 and T_2^* estimates are more accurate in Figs. 4.3c and 4.3d, we propose to use assumed T_2 values or to measure accurate baseline T_2 maps to use for dynamic T_2^* quantification. The latter approach also provides T_2' estimates. Notably, the quality of the combined functional signals is insensitive to the choice of manifold for reconstruction.

4.4 Experiments

We collected resolution phantom data and human fMRI data to evaluate the potential of the manifold model for joint reconstruction and quantification. All the data were acquired with a 3T GE MR750 scanner (GE Healthcare, Waukesha, WI) and a 32-channel head coil (Nova Medical, Wilmington, MA).

4.4.1 Data Acquisition

OSSI acquisition parameters were the same as in Simulation Investigations with 10 s discarded data points to ensure the steady state. We selected a 2D oblique slice passing through the visual cortex with FOV = $220\times220\times2.5\,\text{mm}^3$, matrix size = $168\times168\times1$, and spatial resolution = $1.3\times1.3\times2.5\,\text{mm}^3$. For OSSI, both "mostly sampled" data (for retrospective undersampling) and prospectively undersampled data were acquired. The sampling trajectories were undersampled VD spirals with golden-angle based rotations between time frames as in [52]. The "mostly sampled" data used number of interleaves $n_i = 9$ VD spirals with approximately a 1.5 undersampling factor, and temporal resolution = 1.35 s = TR$\cdot n_c \cdot n_i$. The retrospective undersampling used the first interleave out of 9 for each time frame of the "mostly sampled" data. The prospective undersampling used $n_i = 1$ with temporal resolution = 150 ms = TR$\cdot n_c$ Both retrospective and prospective undersampling provided 12× acceleration.

For quantification evaluation, we acquired multi-echo GRE images to get standard estimations of f_0 and R_2^* values. GRE images were collected with a spin-warp sequence with TR = 100 ms, Ernst flip angle = 16°, and different TEs = 5.9, 13, 26, and 40

ms. R_2^* maps were estimated based on the exponential decay of T_2^*. The field map f_0 was estimated using fully sampled GRE images at TE = 30 and 32 ms [112]. For the phantom data, we additionally acquired spin-echo images with a spin-warp sequence at TR = 400 ms and different TEs = 20, 40, 60, and 80 ms to get $\hat{T}_2$ maps.

For coil sensitivity map calculation, we collected spin-warp images and generated ESPIRiT sensitivity [40, 41] after compressing the 32-channel coil images to 16 virtual coils using PCA [88]. The coil images were 2-norm combined for brain region extraction using the Brain Extraction Tool [39].

For human data, the functional task was a left vs. right reversing-checkerboard visual stimulus with 10 s rest followed by 5 cycles of left or right stimulus (20 s L/20 s R $\times$ 5 cycles). The 10 s resting-state data ensured the oscillating steady state and were discarded. The number of time frames (both fast time n_c and slow time) was 1490 for "mostly sampled" data and was 13340 for prospectively undersampled data.

4.4.2 Performance Evaluation

Every non-overlapping set of $n_c = 10$ fast time images were reconstructed and 2-norm combined for fMRI analysis. To avoid modeling error from the HRF of the initial rest period, the data for the first 40 s task block were discarded. The data were detrended using the first 4 discrete cosine transform basis functions to reduce effects of scanner drift.

We evaluated the functional performance of OSSIMM and comparison approaches using activation maps and tSNR maps. The backgrounds of activation maps were the mean of time-series of images. The activated regions of activation maps were determined by correlation coefficients above a 0.45 threshold. The correlation coefficients were generated by correlating the reference waveform (task and HRF related) with the fMRI time course for each voxel. For each voxel, dividing the mean of the time course by the standard deviation of the time course residual (mean and task removed) provided the tSNR map. We further calculated numbers of activated voxels at the bottom third of the brain (where the visual cortex is located) and the average tSNR values within the brain (after skull stripping).

For quantification, parameter estimations at regions with little or no signal are masked out. Specifically, we generated a mask with the first-echo GRE image (TE = 5.9 ms and after skull stripping) for signals larger than 10% of the signal magnitude and GRE $\hat{R}_2^* < 50$ Hz. Regions with GRE $\hat{R}_2^* > 50$ Hz are concentrated at the

edge of the brain as shown in Fig. 4.11. The quantitative accuracy of OSSI $\hat{R}_2^*$ was evaluated by RMSE with multi-echo GRE $\hat{R}_2^*$ as the standard. Because OSSI $\hat{f}_0$ estimates are in the range of [-33.3, 33.3] Hz, we mapped the GRE $\hat{f}_0$ to the same range for comparison.

4.5 Reconstruction, Quantification, and Results

The proposed OSSIMM method jointly reconstructed high-resolution images and quantitative maps using the near-manifold regularization. For both phantom and human experiments, we used the T_2' manifold with a fixed $T_2 = 100$ ms unless otherwise specified. After reconstructing fast time images with mostly sampled data (OSSI-Mostly), or other models such as low-rank (OSSI-LR) and regularized cgSENSE (OSSI-cgSENSE), we further estimated their corresponding parameter maps using the same manifold as in OSSIMM.

4.5.1 Implementation Details

We selected the regularization parameters based on the Lipschitz constant $\sigma(A)$ calculated with power iteration. We set the regularization parameter β in (4.5) to be a fraction of $\sigma(A)$ that the condition number of the cost function was about 10 to 20 and the performance of the functional maps are maximized. α in (4.8) was selected to enforce that the rank ≈ 4 for the fast time image sets.

In OSSIMM, we used 4 iterations of alternating minimization, and 2 iterations of conjugate gradient for the data fidelity update. We used 15 iterations of POGM for the LR reconstruction and 19 iterations of conjugate gradient for cgSENSE reconstruction and the mostly sampled data. We generated data-shared images as the initialization for the undersampled reconstructions by utilizing the sampling incoherence between fast and slow time [19] and combining k-space data of every 10 slow time points.

4.5.2 Results

For the phantom study, Fig. 4.4 and Fig. 4.12 present OSSI quantification results with a fixed T_2 of 100 ms and a known $\hat{T}_2$ map, respectively. OSSIMM quantifies parameters from retrospectively undersampled data, and results in similar maps as

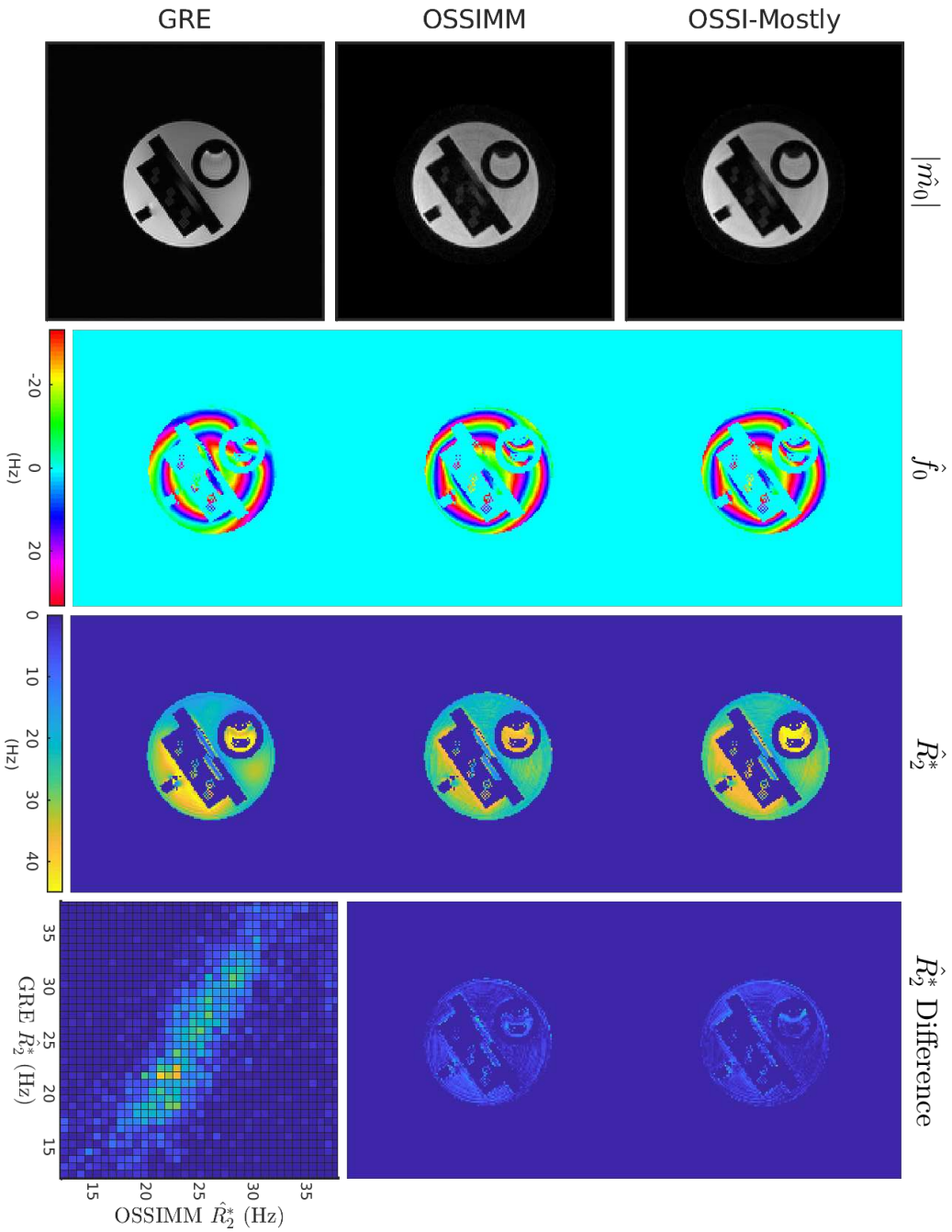

Figure 4.4: Phantom quantification of m_0, f_0, and R_2^* from mostly sampled OSSI data, retrospectively undersampled OSSI data (reconstructed and quantified using OSSIMM), and multi-echo GRE. The $\hat{m}_0$ estimates are on arbitrary scales. The GRE $\hat{R}_2^*$ map is used as the standard for difference map calculation. The $\hat{R}_2^*$ maps and $\hat{R}_2^*$ difference maps use the same color scale. The 2D histogram (bottom right) compares OSSIMM and GRE $\hat{R}_2^*$ within the 12-38 Hz range. OSSI $\hat{R}_2^*$ and GRE $\hat{R}_2^*$ demonstrates similar contrasts.

Table 4.1: Phantom quantification comparison of OSSI $\hat{R}_2^*$ to GRE with or without a known $\hat{T}_2$ map

	Fixed $T_2 = 100$ ms		Known $\hat{T}_2$ map	
	$\hat{R}_2^*$ RMSE (Hz)	Additional Mask	$\hat{R}_2^*$ RMSE (Hz)	Additional Mask
OSSI-Mostly	4.9	4.3	5.0	4.6
OSSIMM	5.5	4.6	5.3	4.5

mostly sampled reconstruction and multi-echo GRE. The 2D histogram demonstrates a close to a linear relationship between OSSI and GRE $\hat{R}_2^*$ values. As summarized in Table 4.1, OSSIMM with a known $\hat{T}_2$ map produces similar results as OSSIMM with a fixed T_2 value. Demonstrated by RMSE values with additional masking in Table 4.1, OSSI $\hat{R}_2^*$ RMSE improves by 0.5-1 Hz when a GRE $12 < \hat{R}_2^* < 38$ mask (within OSSIMM R_2^* dictionary range) is applied.

Figure 4.5 compares retrospectively undersampled reconstructions to the mostly sampled reference. OSSIMM reconstruction well preserves high-resolution structures in oscillatory fast time images and combined images, and leads to less residual in the difference map than LR and cgSENSE approaches.

Figure 4.6 presents prospectively undersampled reconstructions (temporal resolution = 150 ms) using OSSIMM, LR, and cgSENSE. OSSIMM demonstrates activation map with more activated voxels, time course with higher SNR, and sharper tSNR map than other methods. The functional maps from the mostly sampled reconstruction (temporal resolution = 1.35 s) are included in supplemental Fig. 4.13 for reference.

Figure 4.7 gives retrospectively undersampled and mostly sampled OSSI quantification results with comparison to multi-echo GRE. OSSIMM with 12× undersampling leads to $\hat{m}_0$, $\hat{f}_0$, and $\hat{R}_2^*$ estimates that are almost identical to the mostly sampled case and have finer structures than OSSI-LR. OSSIMM also provides comparable $\hat{R}_2^*$ maps to GRE and demonstrates a similar distribution of $\hat{R}_2^*$ values within the brain as GRE according to the 2D histogram. Because of field drift and respiratory changes between different scans, the OSSI-Mostly and OSSIMM $\hat{f}_0$ maps are close to GRE $\hat{f}_0$ but not exactly the same.

Figure 4.8 compares prospectively undersampled quantification results to multi-

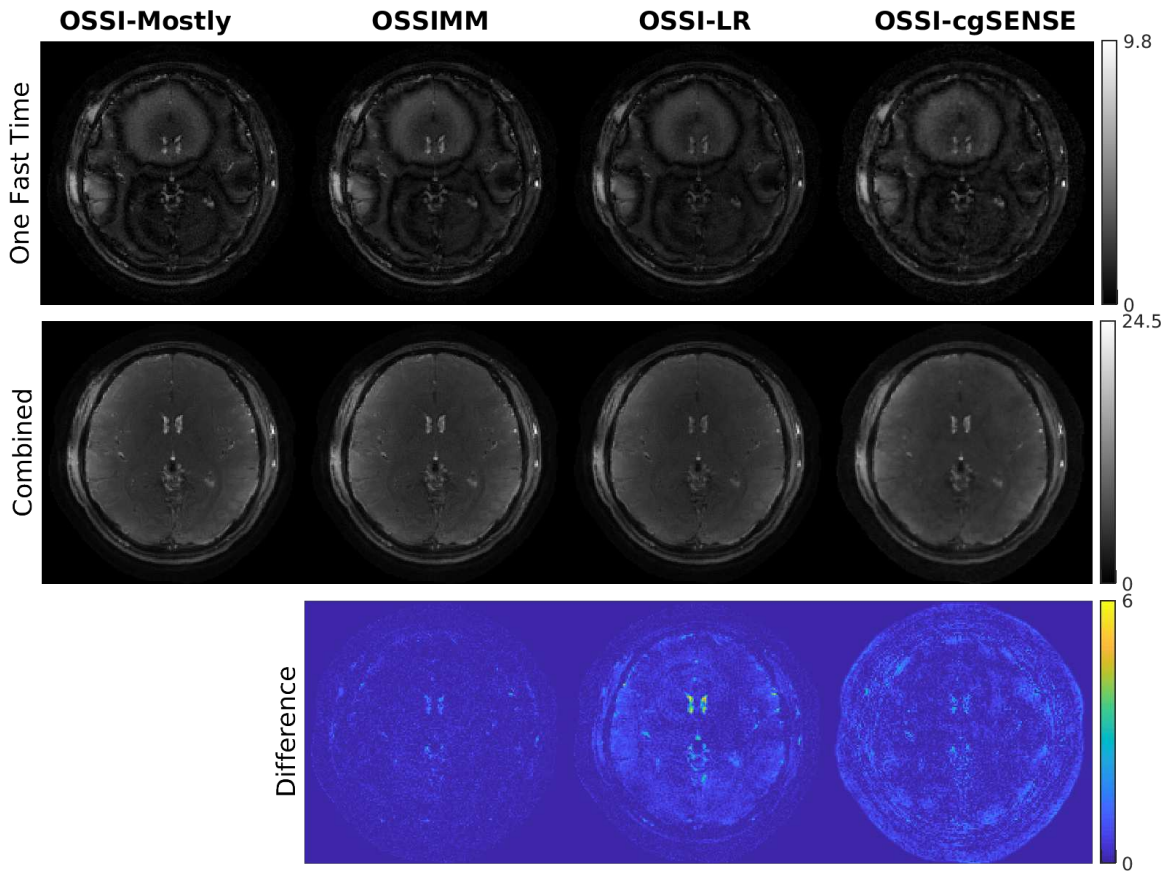

Figure 4.5: Manifold, low-rank, and cgSENSE reconstructions for retrospectively undersampled OSSI data are compared to the mostly sampled reconstruction. The example fast time images present spatial variation in OSSI. OSSIMM outperforms other approaches with cleaner high-resolution details and less structure in the difference map.

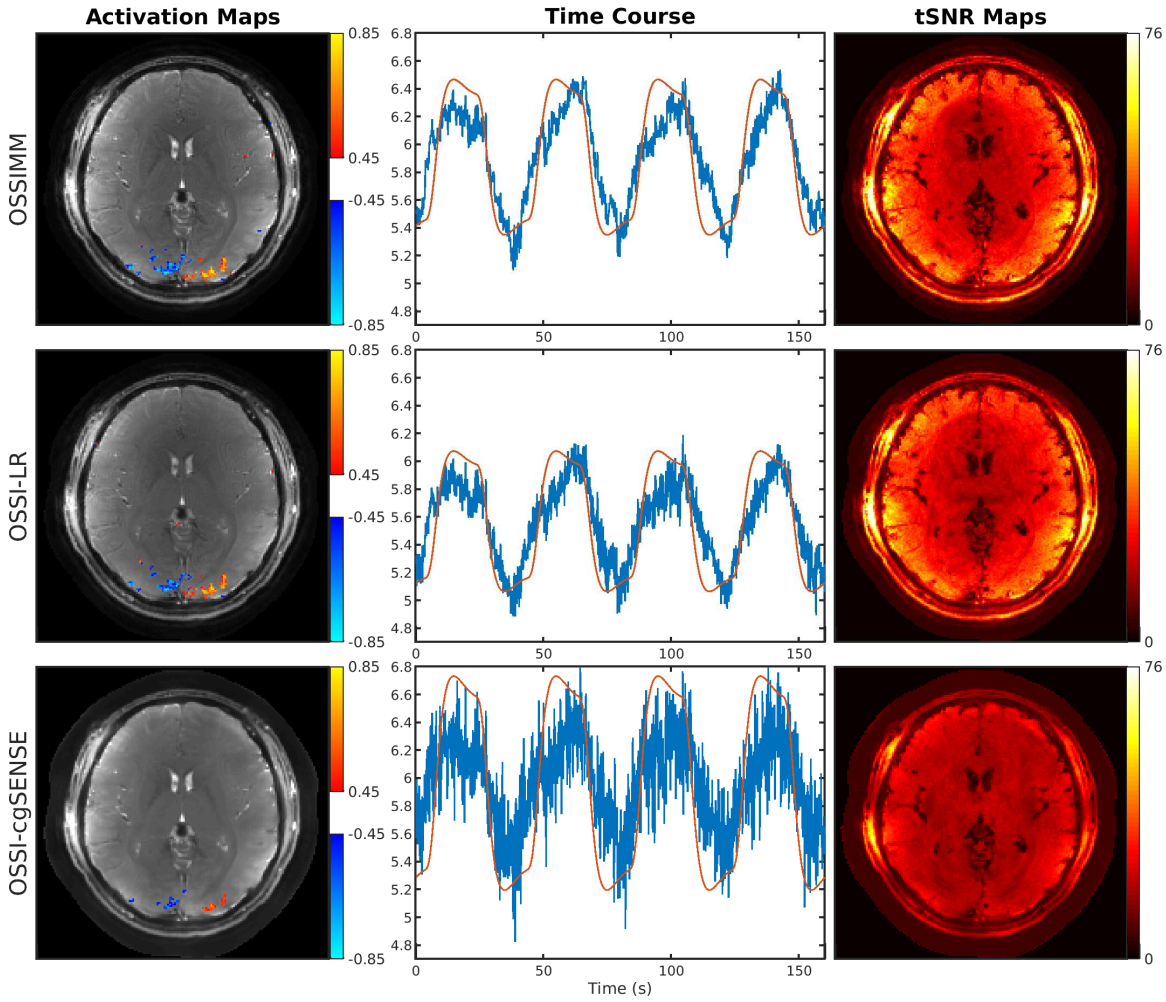

Figure 4.6: Functional results for prospectively undersampled data with spatial resolution of 1.3 mm and temporal resolution of 150 ms. The proposed OSSIMM reconstruction provides an activation map with high-resolution background image and larger activated regions, and time course (reference waveform in red) and temporal SNR map with higher SNR than other methods.

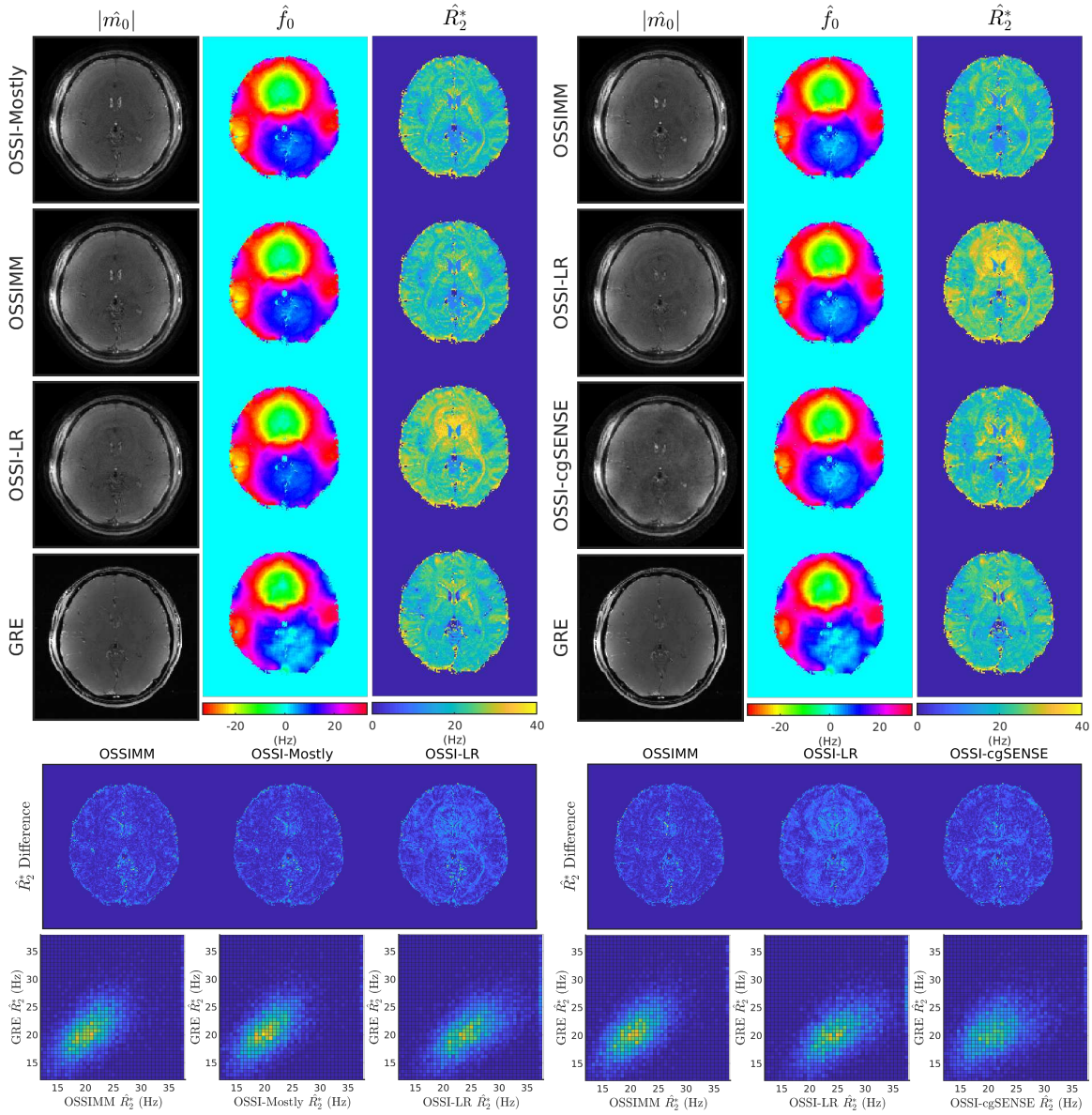

Figure 4.7: Retrospectively undersampled quantifications and comparison to multi-echo GRE estimates. OSSIMM presents similar results as the mostly sampled data. $\hat{R}_2^*$ difference maps (using GRE $\hat{R}_2^*$ as standard and of same color scale as $\hat{R}_2^*$ maps) and 2D histogram of $\hat{R}_2^*$ values show that OSSIMM provides comparable quantitative maps to GRE.

Figure 4.8: Prospectively undersampled quantifications compared to multi-echo GRE. OSSIMM results in reasonable parameter maps with 1.3 mm spatial resolution and a 150 ms acquisition time. OSSIMM also outperforms low-rank and cgSENSE reconstructions with less residual in the $\hat{R}_2^*$ difference map (same color scale as $\hat{R}_2^*$ maps).

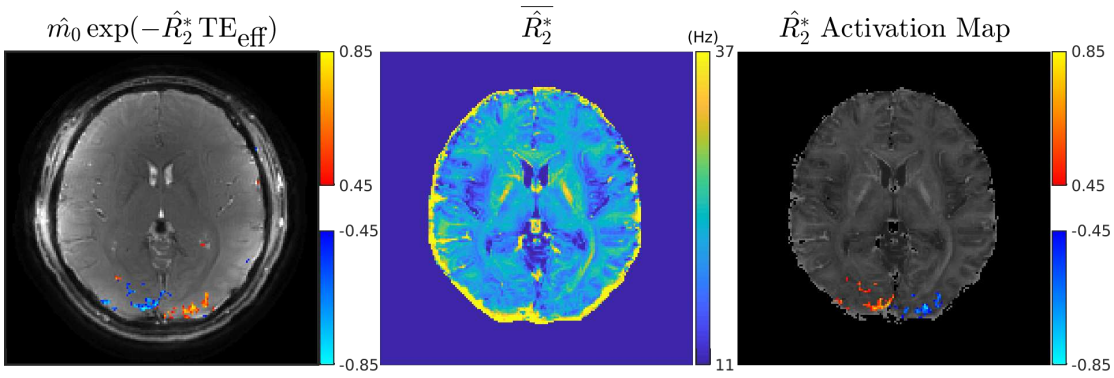

Figure 4.9: Activation maps from OSSIMM $\hat{m}_0$ and $\hat{R}_2^*$ with prospective undersampling demonstrating the dynamic quantification capacity of OSSIMM. Both time series of $\hat{m}_0 \exp(-\hat{R}_2^* \mathrm{TE}_{\mathrm{eff}})$ (left) and $\hat{R}_2^*$ (right) almost fully recover the functional activation. The $\overline{\hat{R}_2^*}$ (middle) is the mean of $\hat{R}_2^*$ time series after skull stripping (without any other mask) and well preserves the R_2^* contrast.

echo GRE. OSSIMM enables high-resolution quantification of m_0, R_2^* and f_0 with a 150 ms acquisition, and yields parameter estimates more similar to GRE than LR and cgSENSE reconstructions.

The parameter maps in Figs. 4.7 and 4.8 are from a single set of $n_c = 10$ fast time images, while OSSIMM jointly reconstructs undersampled measurements and quantifies physics parameters for every 10 fast time images of the OSSI fMRI time course. To demonstrate the dynamic quantification capacity of OSSIMM, Fig. 4.9 shows activation maps for $\hat{m}_0 \exp(-\hat{R}_2^* \mathrm{TE}_{\mathrm{eff}})$ and $\hat{R}_2^*$, where $\hat{m}_0$ and $\hat{R}_2^*$ are quantified using OSSIMM and prospectively undersampled data. OSSI $\mathrm{TE}_{\mathrm{eff}} \approx 17.5$ ms with a 2.6 ms actual TE [16].

The activation maps based on $\hat{m}_0 \exp(-\hat{R}_2^* \mathrm{TE}_{\mathrm{eff}})$ images well preserves R_2^* contrast of OSSI and has the same activated regions as the activation map from 2-norm combined OSSI images (in Fig. 4.6). The activation map from $\hat{R}_2^*$ maps recovers the activation and reduces false positives (negative activation in the positive activation region and vice versa). The colors of the activation are the opposite of activation in Fig. 4.6 due to the negative correlation between $m_0 \exp(-R_2^* \mathrm{TE}_{\mathrm{eff}})$ and R_2^*. The mean R_2^* map ($\overline{R_2^*}$) of the time series, when compared to GRE, leads to a smaller RMSE value of 4.4 Hz. The RMSE value = 3.7 Hz with a GRE $12 < \hat{R}_2^* < 38$ Hz mask.

Table 4.2 summarizes quantitative evaluations of different sampling schemes and

Table 4.2: Human reconstruction and R_2^* quantification evaluation for different sampling patterns and models

	OSSIMM	OSSI-LR	OSSI-cgSENSE	OSSI-Mostly
Retrospectively Undersampled				
$\hat{R}_2^*$ RMSE (Hz)	5.1	6.6	5.4	5.1
Additional Mask	4.5	6.1	4.9	4.5
Prospectively Undersampled				
$\hat{R}_2^*$ RMSE (Hz)	4.9	6.7	5.5	-
Additional Mask	4.3	6.4	5.0	-
# Activated Voxels	181	159	68	-
Average tSNR	26.4	26.5	18.8	-

reconstruction models. OSSI $\hat{R}_2^*$ RMSE values compared to GRE for retrospectively (Fig. 4.7) and prospectively (Fig. 4.8) undersampling are presented. As demonstrated by RMSE values with additional masking, OSSI RMSE decrease by about 0.5 Hz with the GRE $12 < \hat{R}_2^* < 38$ mask. The last two rows of the table correspond to Fig. 4.6 and are numbers of activated voxels and average tSNR within the brain for prospectively undersampled reconstructions. The proposed OSSIMM jointly reconstructs high-resolution images with more functional activation and parameter maps with smaller $\hat{R}_2^*$ RMSE than other approaches.

4.6 Discussion

We propose a novel manifold model OSSIMM that uses MR physics for the signal generation as the regularizer for image reconstruction from undersampled k-space data. The proposed model simultaneously provides high-resolution fMRI images and quantitative maps of important MRI physics parameters.

The proposed near-manifold regularizer has the advantage of allowing for potential imperfections of the manifold model. Instead of requiring the signal values to lie exactly on the manifold, it provides a balance between fitting the fast-time images to the noisy k-space data and to the manifold. For reconstruction, OSSIMM

outperforms low-rank and cgSENSE models by providing more functional activation, without spatial or temporal smoothing.

For quantification, OSSIMM dynamically tracks m_0, R_2^*, and f_0 changes with a temporal resolution of 150 ms in our experiments. The OSSIMM estimates $\hat{m}_0 \exp(-\hat{R}_2^* \, \mathrm{TE}_{\mathrm{eff}})$ or $\hat{R}_2^*$ contain most of the functional information of fMRI time series, and may be well-suited for examining quantitative changes in longitudinal studies. Moreover, OSSIMM quantification is faster than other quantification methods such as [35]. The manifold model and the near-manifold regularization can be generalized to other sparsely undersampled datasets for joint reconstruction and quantification.

There are multiple factors that contribute to slight mismatches between OSSI $\hat{R}_2^*$ and GRE $\hat{R}_2^*$. We noticed that OSSI and GRE images were not exactly aligned due to different gradient delays or the movement of the brain between different scans, especially around the edge of the brain. It is also possible that through-plane gradients change signals slightly differently between OSSI and GRE. The OSSIMM implementation could be improved with a larger dictionary with a larger range of R_2^* values and finer spacing of the varying physics parameters. The RF inhomogeneity in the brain may influence the accuracy of the dictionary fitting due to inaccuracy of the flip angle.

We have neglected the readout length effect for simplicity and have not performed field map correction for human data. The field map correction improves quantification for resolution phantom, but would increase computation for human fMRI time series. One interesting extension would be to dynamically quantify f_0 and correct for field inhomogeneity using the time-series of OSSI $\hat{f}_0$ maps. Because OSSI $\hat{f}_0$ maps are in the range of [-33.3, 33.3] Hz, we could use an initial estimate of $\hat{f}_0$ from two-echo GRE, and dynamically update the initial $\hat{f}_0$ based on OSSI $\hat{f}_0$ changes along time as in [105].

We believe that the reconstruction performance can be further improved with spatial-temporal modeling of OSSI fMRI image series. We will combine OSSIMM with the patch-tensor low-rank model [52] to exploit different aspects of prior information (linear and nonlinear), enlarge the capacity of regularization, and enable more aggressive undersampling. We will also extend the OSSIMM dynamic quantification to 3D fMRI. Because a known $\hat{T}_2$ map can be helpful for $\hat{R}_2^*$ estimation, one might considering modifying the OSSI sequence as in [35] with slowly varying flip angles

and other changes to simultaneously quantify T_2 and T_2'.

4.7 Conclusion

This chapter proposes OSSIMM, a novel reconstruction and quantification model for nonlinear MR signals. With a factor of 12 undersampling and without spatial or temporal smoothing, OSSIMM outperforms other reconstruction models with high-resolution structures and more functional activation. OSSIMM also provides dynamic R_2^* maps that are comparable to GRE $\hat{R}_2^*$ maps with a 150 ms temporal resolution.

4.8 Supporting Information

Figure 4.10 illustrates OSSI "fast time" and "slow time". Figure 4.11 demonstrates voxel locations with GRE $\hat{R}_2^* > 50$ Hz. Figure 4.12 presents phantom quantification results, and OSSI quantitative maps that were calculated with a known $\hat{T}_2$ map. Figure 4.13 presents fMRI results for mostly sampled human data.

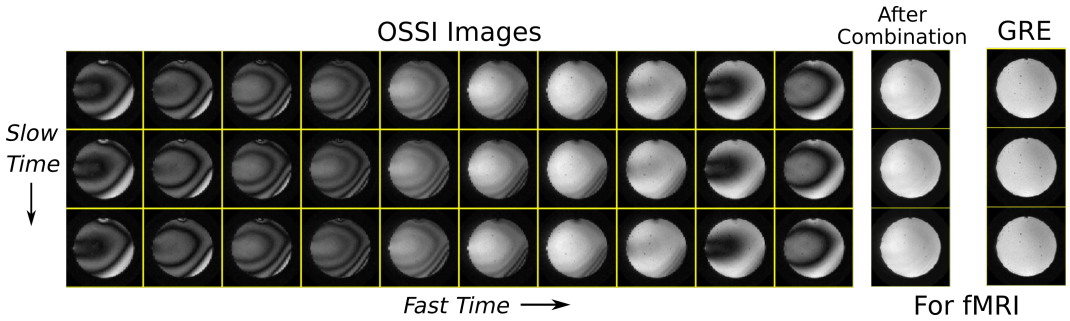

Figure 4.10: OSSI images with periodic and nonlinear oscillation patterns are structured along "fast time" and "slow time". Every n_c fast time images can be 2-norm combined to generate fMRI images that have comparable T_2^*-sensitivity as standard GRE fMRI.

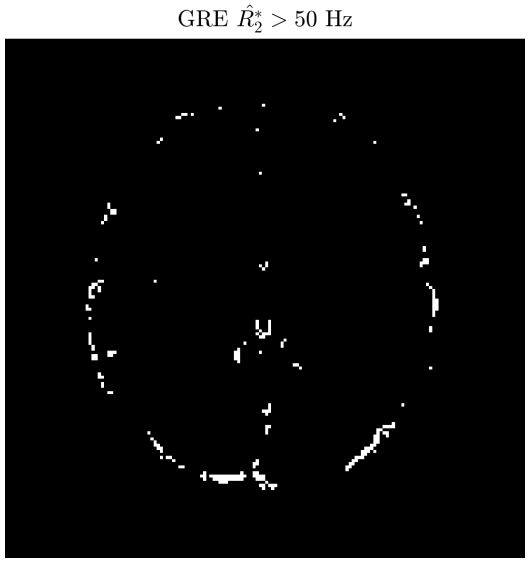

Figure 4.11: Most voxel locations with GRE $\hat{R}_2^* > 50$ Hz are around the edges of the brain.

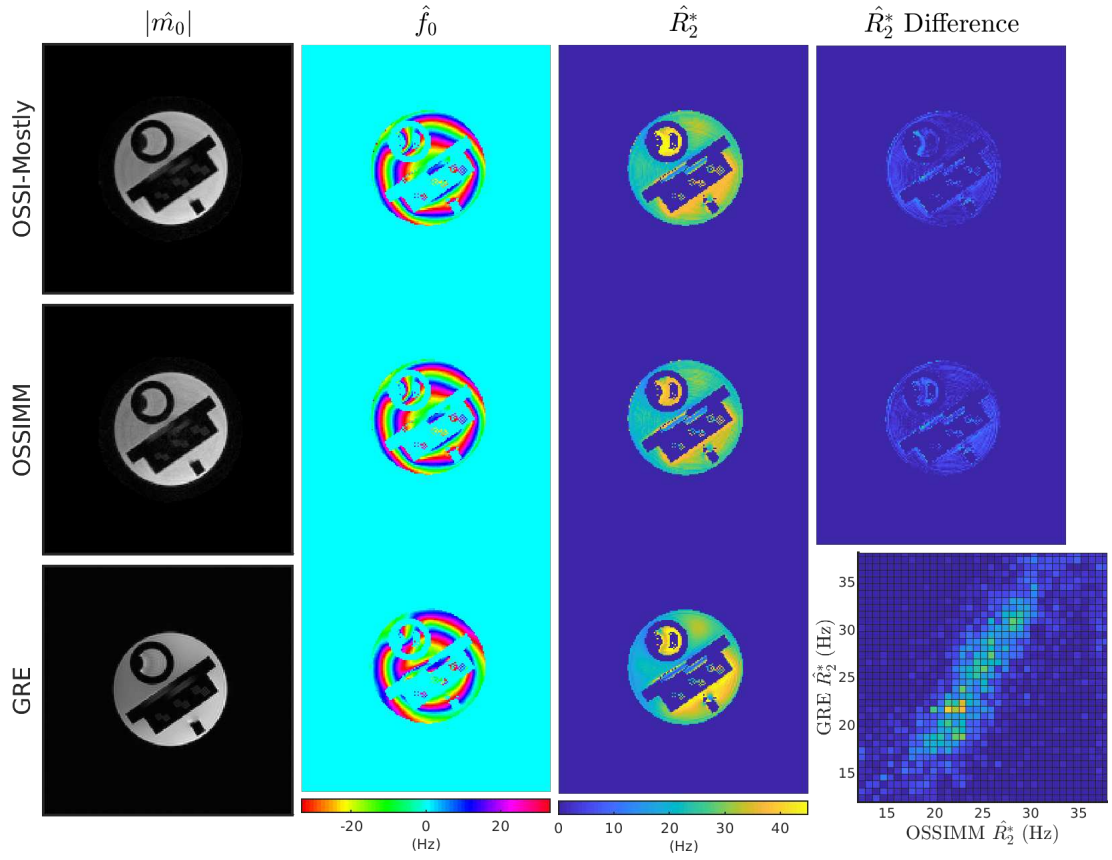

Figure 4.12: Phantom quantification of m_0, f_0, and R_2^* from mostly sampled OSSI data, retrospectively undersampled OSSI data (reconstructed and quantified using OSSIMM with a known $\hat{T}_2$ map), and multi-echo GRE. The $\hat{m}_0$ estimates are on arbitrary scales. The GRE $\hat{R}_2^*$ map is used as the standard for difference map calculation. The $\hat{R}_2^*$ maps and $\hat{R}_2^*$ difference maps use the same color scale. The 2D histogram (bottom right) compares OSSIMM and GRE $\hat{R}_2^*$ within the 12-38 Hz range. OSSI $\hat{R}_2^*$ and GRE $\hat{R}_2^*$ have similar contrasts.

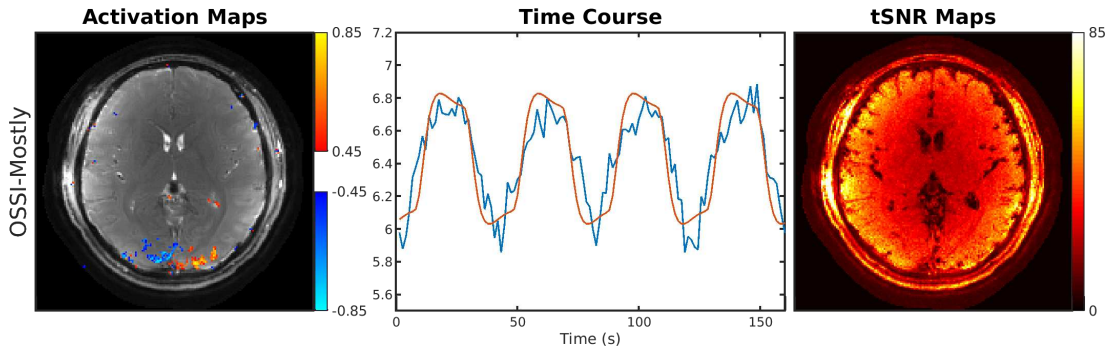

Figure 4.13: Functional results for mostly sampled data with spatial resolution of 1.3 mm and temporal resolution of 1.35 s. The number of activted voxels is 236, and the average temporal SNR within the brain is 31.3.

CHAPTER V

Voxel-wise Temporal Attention Network and Simulation-Driven Dynamic MRI Sequence Reconstruction

Deep learning-based approaches have been successful for structural MRI undersampled reconstruction [14, 15]. However, there are fewer works on learning-based dynamic MRI reconstruction [13, 113] with two main open questions: 1) what would be a good learning-based approach for temporal or spatial-temporal signal modeling, 2) for dynamic MRI sequence of images, how to get enough training data for the learning schemes that are data hungry? Inspired by these two questions, we propose a voxel-wise attention network based on the emerging attention mechanism [114, 115] for temporal modeling, together with a matched transfer learning approach to handle the problem of limited amounts of training data.

Our work has three novel contributions: 1) incorporate an attention mechanism for temporal learning and mapping, 2) propose a voxel-wise network architecture based on attention and Transformers for spatial-temporal undersampled reconstruction, 3) propose a two-stage learning scheme that pretrains the network with voxel-wise simulated data, and then fine-tunes with human temporal data for dynamic MRI. [1]

5.1 Introduction

Previous models [19, 20] for undersampled OSSI MRI sequence reconstruction focus on hand-crafted features of the data, whereas learning features using neural

[1] This chapter is based on [116].

networks has proven to be very useful and successful for vision tasks [117, 118] and undersampled MRI reconstruction [14, 15] in recent years. Another advantage of neural network approaches is fast computation in the testing stage, whereas iterative methods can be slow for reconstructing high-resolution images.

For dynamic MRI reconstruction, previous works used a cascade of convolutional neural networks (CNN) with designed data consistency layers [13] and convolutional recurrent neural network (RNN) for temporal dependence between images [113]. However, the convolutional operations in CNNs are local and fail to capture long-range dependencies [119, 120], and the shared weights for the spatial/temporal dimensions could potentially lead to spatial/temporal smoothness effects. Moreover, 3D CNNs for video inputs [121] or sequences of images often require large amounts of data for training due to the increased number of learnable parameters, and would be computationally expensive for long sequences. On the other hand, recurrent inference for images in a sequence is not ideal for modeling the temporal redundancy between images because of the causal nature; in particular, when all the input images in a sequence are undersampled and aliased, the recurrent inference will likely pass on the aliased features and noise.

We found that none of the existing methods work well for functional MRI with small BOLD signals [122], whereas the attention mechanism [114, 123] and Transformers [115, 124] that naturally exploit long-range dependence in image sequences could be a great fit for MRI spatial-temporal modeling.

A Transformer is a new neural network structure first presented in [115]. It consists of self-attention [114], multilayer perceptron, residual connections, and layer normalization [125]. Transformers have been the building block for important natural language processing networks such as BERT [126] and GPT-3 [127]. For visual tasks, recent works have demonstrated great potential of Transformers as they match or outperform state-of-the-art CNNs for different visual tasks [124, 128, 129]. The self-attention mechanism and Transformer architecture map a sequence of inputs to a sequence of outputs where each output in the sequence is a learned combination of all the inputs. We hypothesize that this attention design is beneficial for modeling spatial-temporal dependency in dynamic MRI image series and has the potential to outperform CNN and RNN methods.

Another major issue of the learning-based approach is the need for large amount of training data. In dynamic MRI, the object is changing as it is being imaged, so

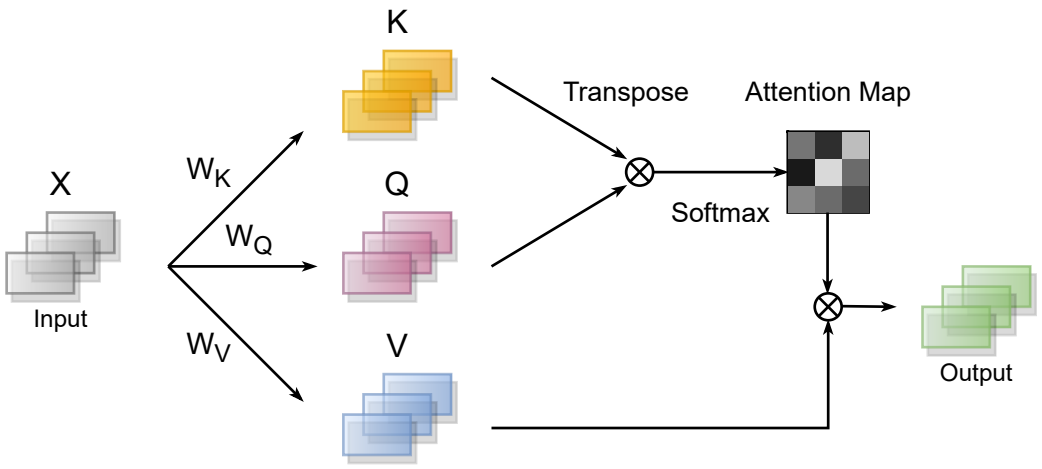

Figure 5.1: Illustration of the attention mechanism. A sequence of input vectors is mapped to a sequence of output vectors. Each vector in the output sequence is a weighted combination of all the vectors in the input sequence, and the weights are determined by the learned attention map.

it is impossible to collect truly fully sample reference data. All dynamic MRI data is inherently undersampled. So high quality "ground truth" training data is never available. This problem is especially acute for novel acquisition methods that have not accumulated a large database of human subjects for training.

We aim to tackle two open questions of dynamic MRI reconstruction - the model and the data - in two steps. We propose a novel voxel-wise attention network for temporal modeling of the image sequences to be reconstructed. The voxel-wise design of the network enables voxel-wise training, and we further propose a transfer learning scheme that pretrains the network with a large amount of voxel-wise simulated data to alleviate the demand for human fMRI data during training.

5.2 Methods

5.2.1 Attention Mechanism

The self-attention mechanism [114, 115] maps a sequence of input vectors to a sequence of output vectors by computing a weighted combination of all the input vectors for each of the output vector. The weights are determined by similarity between pairs of feature representations. Fig. 5.1 illustrates the attention mechanism. For an input sequence $X \in \mathbb{R}^{t \times d}$ of t vectors of dimension d (d can be vectorized

spatial dimensions or spatial representations for a sequence of 2D MRI images, and the complex MRI data is formed into real and imaginary channels), the self-attention mechanism first extracts feature representations by multiplying X with three learnable parameter matrices: $W_{\mathrm{Q}} \in \mathbb{R}^{d \times d_k}$, $W_{\mathrm{K}} \in \mathbb{R}^{d \times d_k}$, $W_{\mathrm{V}} \in \mathbb{R}^{d \times d_v}$, where $d = d_k = d_v$ in our reconstruction task. The relative size of d_k and d depends on the implementation of the network. The three resultant matrices are called query, key, and value, and are calculated by

$$Q = XW_{\mathrm{Q}}, \quad K = XW_{\mathrm{K}}, \quad V = XW_{\mathrm{V}}. \tag{5.1}$$

The output sequence of the attention mechanism is then formed as

$$A(Q, K, V) = \mathrm{softmax}\left(\frac{QK^T}{\sqrt{d}}\right) V \in \mathbb{R}^{t \times d}, \tag{5.2}$$

where $\mathrm{softmax}(\cdot) : \mathbb{R}^t \to (0, 1)^t$ denotes the softmax function

$$\sigma(\mathbf{z})_i = \frac{e^{z_i}}{\sum_{j=1}^{t} e^{z_j}},$$

applied row-wise to the input matrix, $i = 1, ..., t$ and $\mathbf{z} = (z_1, ..., z_t)$.

De-aliasing of a dynamic sequence with undersampling artifacts can be viewed as mapping a temporal sequence with aliasing to a sequence without aliasing. We use the attention mechanism as a key component for the dynamic sequence reconstruction.

5.2.2 Proposed Voxel-Wise Attention Network

We formulate the cost function of our reconstruction problem with two alternating minimization steps as

$$\hat{\mathbf{w}}_i = \arg\min_{\mathbf{w}} \|\mathbf{\Phi}(\mathbf{w}; \mathbf{X}_{i-1}) - \mathbf{X}_{\mathrm{true}}\|_1, \tag{5.3}$$

$$\hat{\mathbf{X}}_i = \arg\min_{\mathbf{X}} \frac{1}{2}\|\mathcal{A}(\mathbf{X}) - \mathbf{y}\|_2^2 + \beta\|\mathbf{X} - \mathbf{\Phi}(\mathbf{X}_{i-1}; \mathbf{w}_i)\|_2^2, \tag{5.4}$$

where $\mathbf{X} \in \mathbb{C}^{t \times H \times W}$ denotes the dynamic sequence of images to be reconstructed, and the index i corresponds to the ith iteration. The attention network is parameterized as $\mathbf{\Phi}(\cdot\,; \mathbf{w}_i)$, and $\mathbf{w}_i$ denotes the network weights for the ith "outer" iteration of the

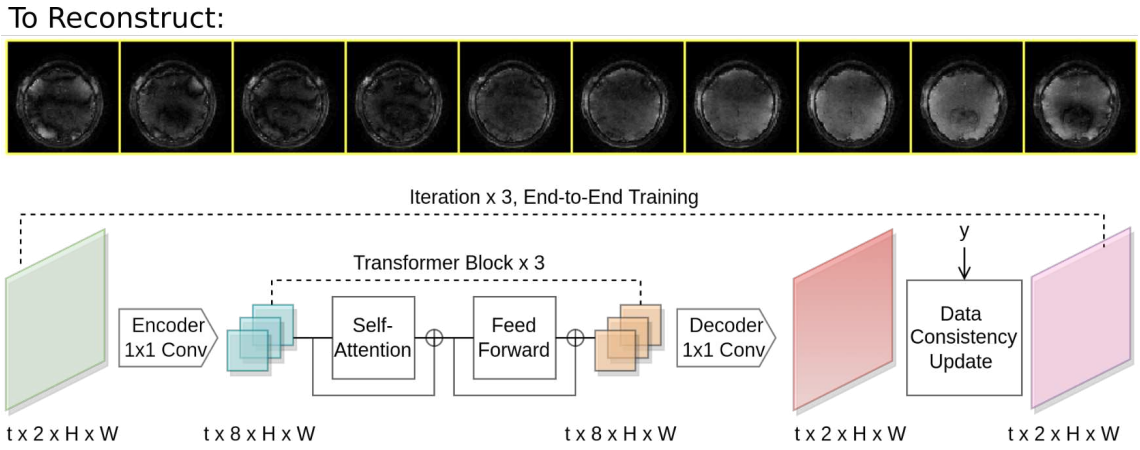

Figure 5.2: Our proposed voxel-wise temporal attention network architecture and the dynamic OSSI MRI images (with temporal dimension = 10) to be reconstructed. The data fidelity contains 2 iterations of CG-SENSE for multi-coil NUFFT reconstruction. The main part of the network (encoder-Transformer-decoder) can take voxel-wise simulations or spatial images/patches from human data as inputs.

alternating minimization process. $\mathbf{X}_0 \in \mathbb{C}^{t\times H\times W}$ is data-shared initialization, and $\mathbf{X}_{\text{true}} \in \mathbb{C}^{t\times H\times W}$ is the ground truth labels for training. $\mathcal{A}(\cdot)$ is a linear operator representing the MR physics, $\mathbf{y}$ denotes undersampled k-space measurements, and β is the regularization parameter.

We propose a voxel-wise attention network $\mathbf{\Phi}(\mathbf{w})$ with Transformers as building blocks for the method of Eq. (5.3). The voxel-wise attention network is composed of three components: 1) an encoder that brings the input time-series to the feature domain, 2) consecutive Transformer blocks [115, 124] that consist of attention, feed-forward operations, and residual connections, 3) a decoder that brings the Transformed sequence to the image domain. We use convolutions with 1×1 kernels in both the encoder and decoder to ensure the voxel-wise operations of the network. Fig. 5.2 presents the overall framework with an attention network and data consistency.

The input complex MRI image sequence is formed with 2 channels of real and imaginary data, and the dimension is $t \times C \times H \times W$ with $C = 2$. The encoder consists of 2 convolutional layers (followed by leakyReLU) and encodes the input to richer feature representations with an increased channel dimension of 8 and preserves the same spatial dimensions with 1×1 convolutions. The temporal sequence of feature maps from the encoder is transformed to another temporal sequence of maps with three consecutive Transformer blocks. The learnable weights W_{Q}, W_{K}, and W_{V} are

implemented with 1×1 convolutions as in [130, 131], and the feed-forward operation in each Transformer block is performed with 2 convolutional layers with 3×3 and instance normalization [132]. The decoder brings the transformed feature maps back to the image domain of size $t \times 2 \times H \times W$ with 2 convolutional layers.

The voxel-wise attention network is followed by a data fidelity layer for solving Eq. (5.4). Equation (5.4) is a quadratic least-squares problem that regularizes $\mathbf{X}$ to be close to the attention network output $\mathbf{\Phi}(\mathbf{X}_{i-1}; \mathbf{w}_i)$ by minimizing the Euclidean distance. We solve Eq. (5.4) using the conjugate gradient (CG) method and form a data fidelity layer that takes attention network transformed images $\mathbf{\Phi}(\mathbf{X}_{i-1}; \mathbf{w}_i)$ as part of the inputs, and performs 2 iterations of the CG update. The linear operator $\mathcal{A}$ with multi-coil and NUFFT operation is implemented using [133]. The output of the data fidelity layer becomes new inputs for the voxel-wise attention network, and we repeat this step 3 times as 3 outer iterations for the alternating minimization of $\mathbf{X}$ and $\mathbf{w}$. We choose the numbers of CG and outer iterations empirically.

5.2.3 Two-Stage Training and Data Simulation

We performed two-stage training to handle the problem with limited human data for learning. We pretrain the attention network with voxel-wise simulated temporal sequences (which could be easier to simulate than spatial-temporal sequences). After pretraining, we fine-tune the attention network together with data consistency using human data as training data and train the whole framework in an end-to-end fashion.

For simulated data, we generated the ground truth sequence [20] using Bloch simulation with varying physics parameters. The inputs for the network are complex Gaussian noise corrupted sequences with a standard deviation of 0.2 to very roughly model the aliasing artifacts. The pretraining of the attention network maps noisy input sequences to noiseless ground truth sequences, and trains the network to denoise.

5.2.4 Implementation Details

The human data were acquired with OSSI sequence [16]. We formed a human data training set with 10 oscillatory temporal images for each 2D slice and 22 distinct slices in total. We augmented the training data 10 times by circularly shifting every image set of 10 oscillating images with 10 different shift positions along the dynamic

time dimension. Ground truth images were reconstructed from mostly sampled data. The k-space data were multi-coil and undersampled using variable-density spiral trajectories with an undersampling factor of 12 as in [19]. We preprocessed the data by normalizing them using the maximum absolute value of data-shared images. We used data-shared initializations as inputs for the network.

The simulated data contains 8,662,000 voxel-wise time courses of dimension 10×1. We pretrained the network with simulated data for 60 epochs and fine-tuned the network with human data patches for 60 epochs. The testing data has 1480 dynamic images for a 200 s OSSI fMRI scan. In the testing stage, we reconstructed sets of 10 dynamic images of the OSSI fMRI data using the proposed network, and l_2-combined each set of 10 reconstructed images to get a sequence of fMRI images for evaluation. The functional task was a left/right reversing-checkerboard visual stimulus for 5 cycles (20 s L/20 s R).

5.3 Comparisons and Results

We compared our proposed approach to a 3D U-Net [134] that takes sets of 10 dynamic images as 3D volumes for processing. The network was trained with human fMRI data. Because 3D U-Net is a spatio-temporal network, we cannot easily pretrain the network with simulated data.

Fig. 5.3 presents attention map visualization for simulated temporal sequence mapping and human temporal sequence mapping, respectively. Each sample of the output sequence is formed based on a weighted combination of all the samples in the input sequence, and the weights are given by the rows of the learned attention map. Specifically, for every row of the attention map, all the values in the row sum to 1, and each value in the row represents the weight for the corresponding input vector of the input sequence. For the ith row, a weighted combination of all the input vectors produces the ith output vector of the output sequence.

For reconstruction, Fig. 5.4 shows that the proposed method leads to less structure in the difference maps than other reconstruction methods such as 3D U-Net. Every 10 reconstructed images are combined with l_2-norm for fMRI. Fig. 5.5 provides functional maps for the reconstructions. The proposed model results in fewer false positives and cleaner time course compared to the fully sampled data. Tab. 5.1 and Fig. 5.6 summarizes quantitative evaluations of the reconstruction and functional

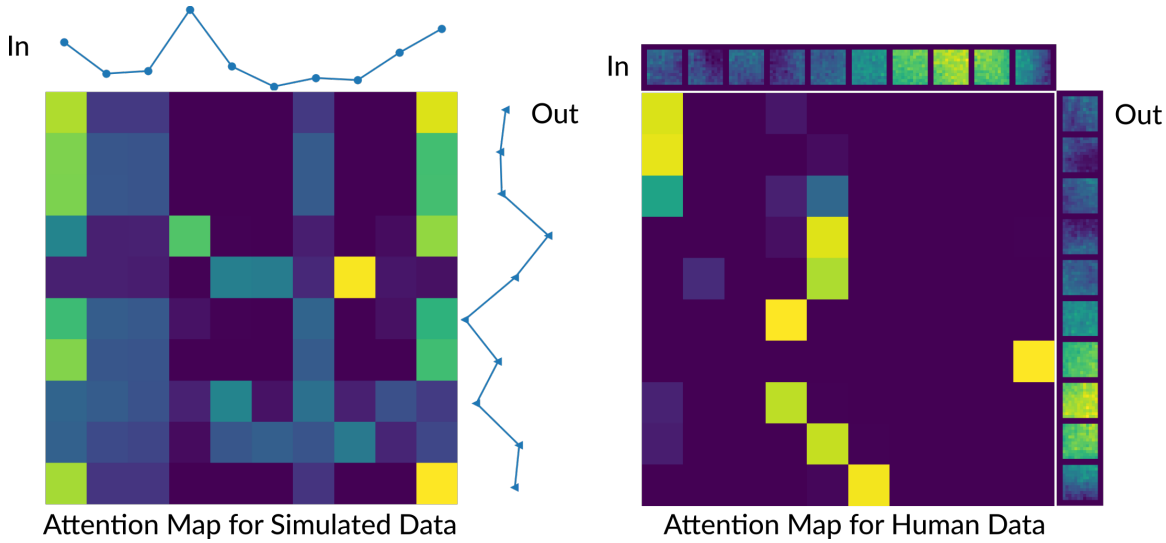

Figure 5.3: Attention map visualization at the testing stage for voxel-wise simulation data (left) and human data patch mapping (right). In the attention mechanism, each output value in a 10×1 sequence is generated with a weighted combination of all the values in the input sequence, and the learned weights are given by each row of the 10×10 attention maps for each output value. The figure presents absolute values of the complex input/output for illustration while the proposed network inputs real and imaginary parts and uses deep representations from the encoder for attention calculation.

performance. The proposed model outperforms other methods with lower NRMSE values, and also provides the largest area under the ROC curve.

5.4 Conclusions

We propose a novel voxel-wise attention network for dynamic MRI temporal modeling. The voxel-wise network design enables pretraining with voxel-wise simulated data that can be easier to obtain than spatial-temporal data, and resolves the training data limitation for dynamic imaging. Our proposed model reconstructs dynamic MRI images with a factor of 12 undersampling, and provides high-quality reconstruction and functional maps. The proposed learning-based reconstruction approach is at least 4× faster than the manifold model-based reconstruction method in Chapter IV. The proposed voxel-wise, attention-based model can potentially be used for MR fingering reconstruction and other dynamic reconstruction applications.

We can observe some horizontal line artifacts in the tSNR map of the proposed approach in Fig. 5.5 because the network was trained with patches while being tested with the whole brain images. In future work, we plan to design a hierarchical network or a multi-stage training scheme to help the network process the whole brain images. The network might take voxel-wise simulated time courses for the first stage, then fine-tune with sequences of image patches, finally refine with whole brain images. The proposed pipeline could potentially be improved with more sophisticated Transformer network designs for increased representation capacity and a GAN loss for sharpness of the images.

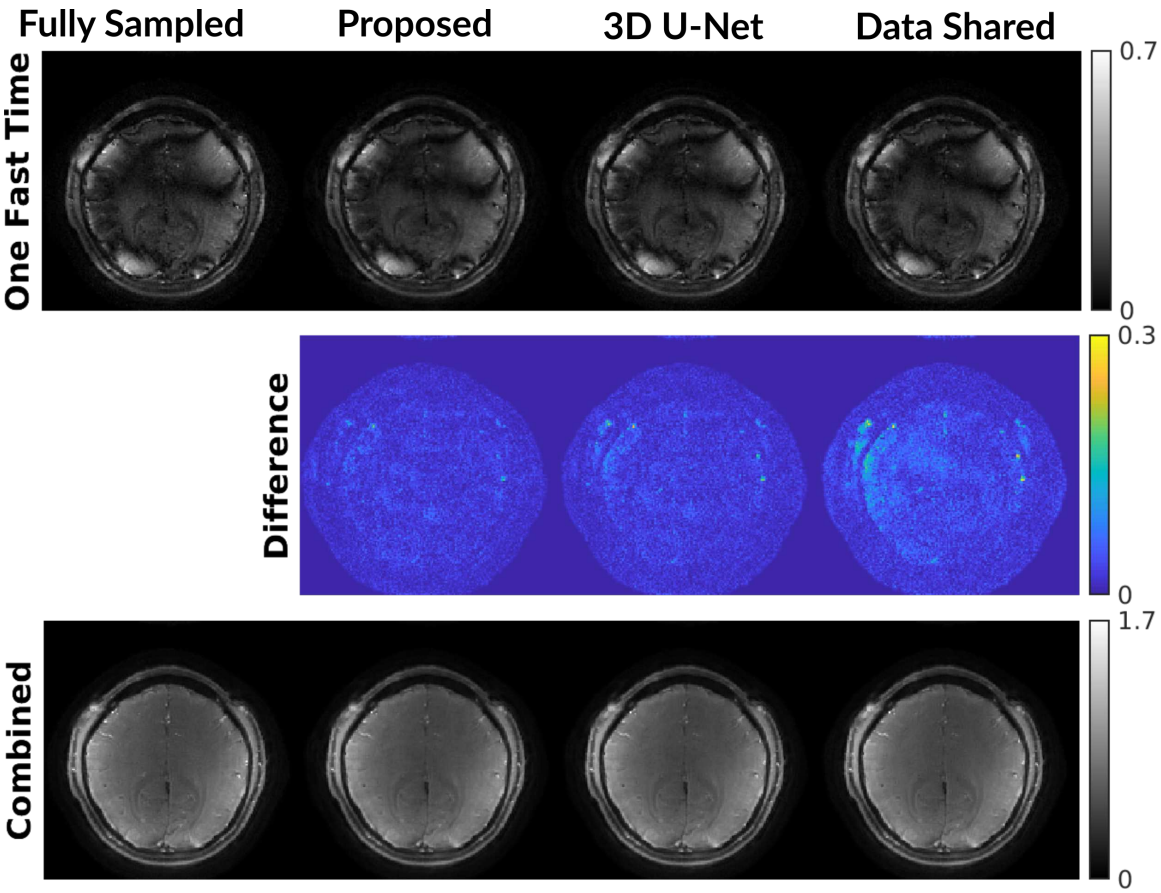

Figure 5.4: The proposed voxel-wise model presents less residual in the difference maps than spatial-temporal reconstruction using 3D U-Net.

Table 5.1: Quantitative evaluation for dynamic undersampled reconstructions

Reconstruction	Proposed	3D U-Net	Data Shared
NRMSE	**0.13**	0.15	0.16
AUC	**0.94**	0.91	0.93

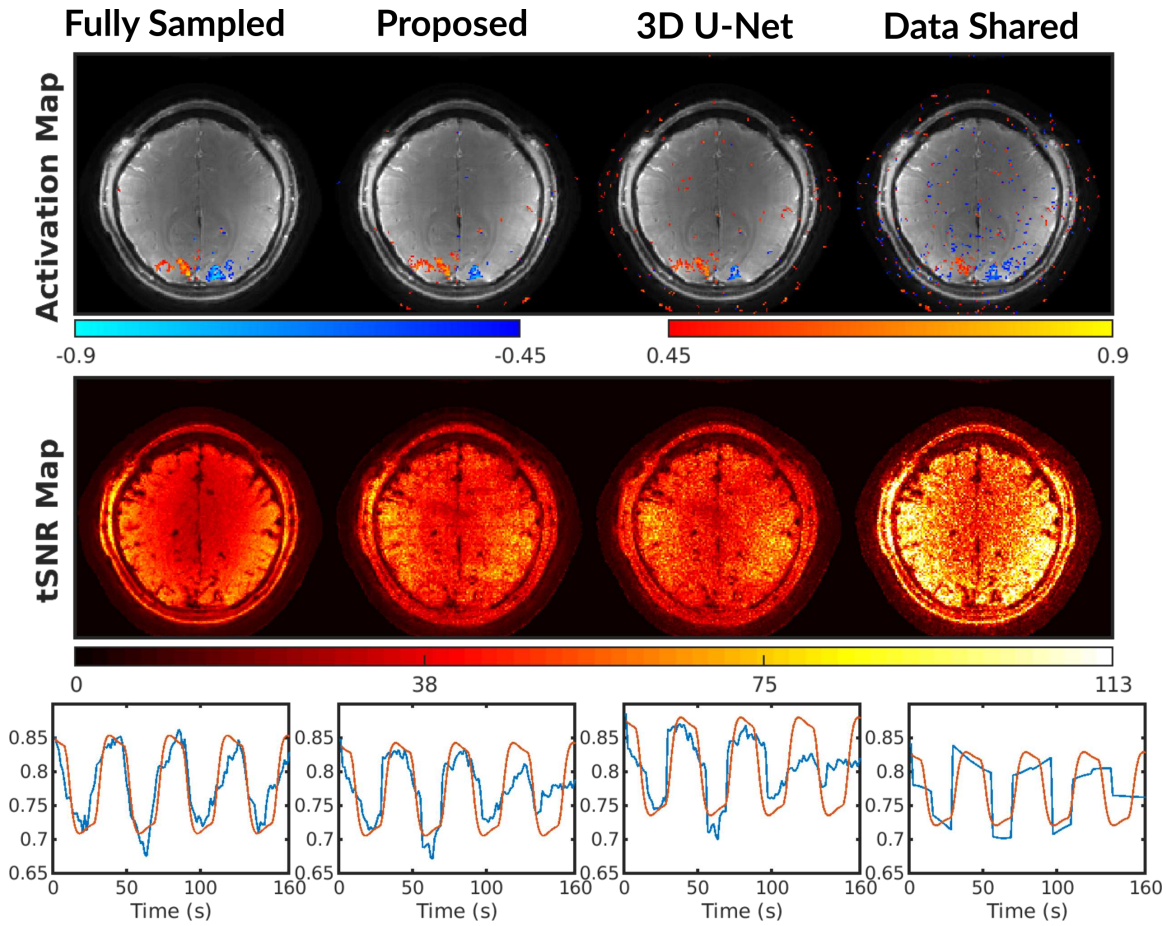

Figure 5.5: The proposed approach results in fewer false positives in the activation map, less noisy temporal SNR map, and a time course more similar to the ground truth.

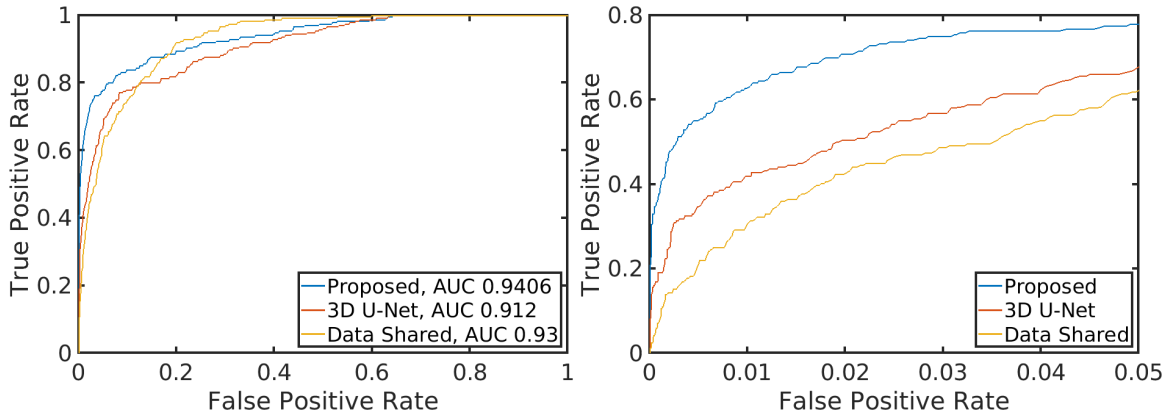

Figure 5.6: The ROC curves for fMRI demonstrate that the proposed model outperforms other reconstructions.

CHAPTER VI

Future Work

In previous chapters, we have proposed three different models: patch-tensor low-rank model, physics-based manifold model, and attention network model for undersampled MRI sequence reconstruction. All of them preserve the high SNR advantage of OSSI, and outperform other reconstruction models with higher spatial-temporal resolution and more functional activation. In future work, we propose an extended approach that combines the advantages of the tensor model and the manifold model, and propose new ideas for learning-based reconstruction and directions for other types of models.

6.1 Linear plus Nonlinear (L+N) Model for 3D OSSI fMRI Acceleration and Dynamic Quantification

The patch-tensor low-rank approach from Chapter III and physics-based manifold models from Chapter IV fit the OSSI sequence data to linear subspaces and a nonlinear manifold, respectively. The patch-tensor model exploits local spatial-temporal similarities with 3D patch tensors of vectorized spatial dimension, and fast and slow time dimensions. The physics-based manifold model focuses on nonlinear modeling of voxel-wise fast time signals and enables physics parameter quantification. Because the two models exploit different properties of the OSSI images, we propose a linear subspace plus nonlinear manifold (L+N) model that combines the advantages of the patch-tensor model with the manifold model for 3D OSSI joint reconstruction and quantification with more aggressive undersampling.

We form patch-tensors as in Chapter III, and impose low-rank constraints on

the first and third unfoldings of the patch-tensors [19]. For the second unfolding of the patch-tensor that is not very low-rank along the fast time dimension, instead of enforcing low-rankness, we fit the fast time signals to the manifold model and encourage the voxel-wise signal values to lie close to the manifold.

The cost function of the proposed L+N model is:

$$\begin{aligned}
\hat{\mathbf{X}} &= \arg\min_{\mathbf{X}} f(\mathbf{X}) \\
f(\mathbf{X}) &= \sum_{i=1,3}\sum_{m=1}^{M} \lambda_i \|\mathcal{P}_m(\mathbf{X})_{(i)}\|_* + \beta \sum_{n=1}^{N} \mathcal{R}\left(\mathbf{X}_{(2)}[:,n]\right) + \frac{1}{2}\|\mathcal{A}(\mathbf{X}) - \mathbf{y}\|_2^2, \\
\mathcal{R}(\mathbf{v}) &= \min_{m_0, T_2', f_0} \|\mathbf{v} - m_0 \mathbf{\Phi}(T_2', f_0; T_1, T_2)\|_2^2,
\end{aligned} \tag{6.1}$$

where $\mathbf{X} \in \mathbb{C}^{x\times y\times z\times t}$ is a complex OSSI fMRI time block to be reconstructed. $\mathcal{P}(\cdot)$ partitions and reshapes the input into M low-rank patch-tensors with $\mathcal{P}_m(\mathbf{X}) \in \mathbb{C}^{s_p\times n_c\times t_s}$, $m = 1,\ldots,M$. $\mathcal{P}_m(\mathbf{X})_{(i)}$ is the mode-i unfolding of $\mathcal{P}_m(\mathbf{X})$. λ_i is the regularization parameter for low-rankness of the mode-i unfolding . $N = xyzt_s$ for the near-manifold regularizer, and β is the regularization parameter. $\mathbf{v} \in \mathbb{C}^{n_c}$ is a vector of fast time signal values for each voxel in $\mathbf{X}$, $m_0\mathbf{\Phi}(T_2', f_0; T_1, T_2) \in \mathbb{C}^{n_c}$ denotes the manifold estimates. $\mathcal{A}(\cdot)$ is a linear operator consisting of coil sensitivities and the non-uniform Fourier transform including undersampling, $\mathbf{y}$ represents sparsely sampled k-space measurements.

The cost function Eq. (6.1) will be optimized using the alternating direction method of multipliers algorithm in Chapter III. The main difference would be for updating the second unfolding that is regularized by the near-manifold model, instead of applying the singular value soft-thresholding operator in Eq. (3.11), we will use the conjugate gradient method for the quadratic least-squares problem.

The sampling pattern we investigated initially is Poisson-disk undersampling of stack-of-spirals with a factor of 12 acceleration. Fig. 6.1, Fig. 6.2, and Fig. 6.3 show the preliminary results for Poisson-disk sampling of $kz - t$ planes, activation maps, and temporal SNR maps using the proposed reconstruction.

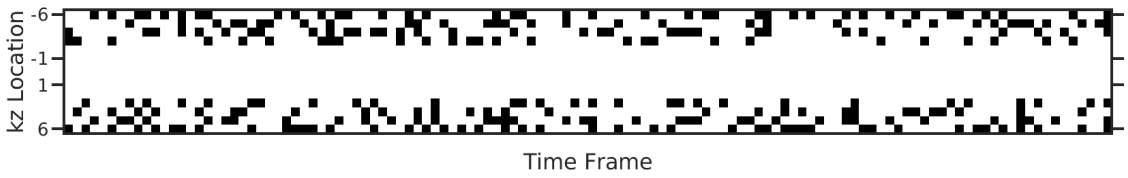

Figure 6.1: Poisson-disk sampling of k_z - t planes that keeps 80% of the variable-density spirals. White color denotes sampled location, and black color denotes kz planes that are not acquired.

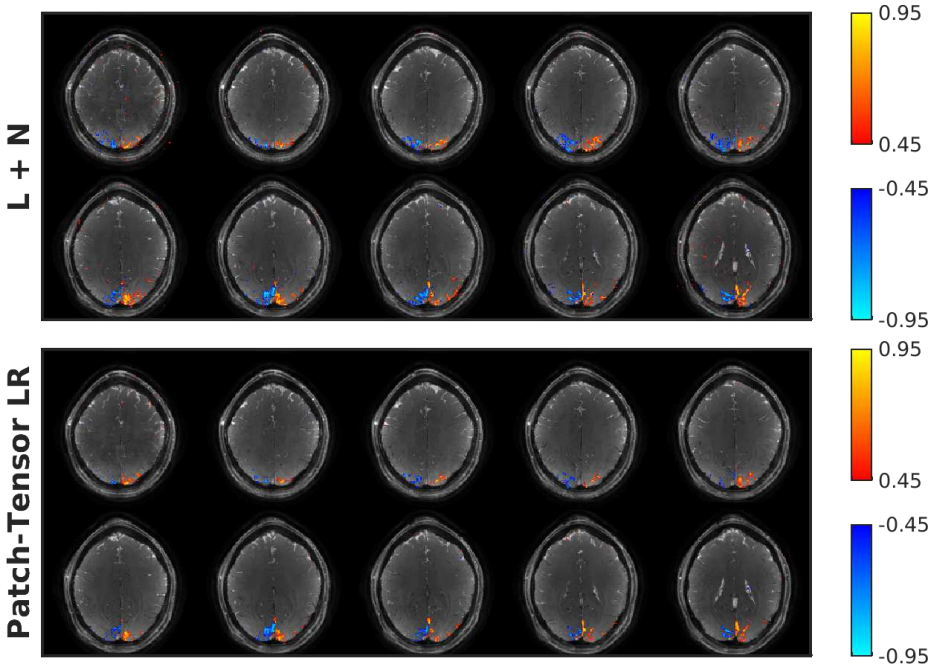

Figure 6.2: 3D OSSI activation map of the proposed model yields more activation than the patch-tensor low-rank model in Chapter III.

6.2 Other Ideas and Approaches

Our work presents innovations in high-dimensional modeling, physics constraint modeling, and MR image sequence modeling. In particular, the physics-based manifold model inspires us to design an unsupervised learning approach that models MR physics for OSSI signal generation to reconstruct OSSI images directly from physics parameters. In general, we hope to combine signal processing and physics insights with deep learning to advance different types of applications.

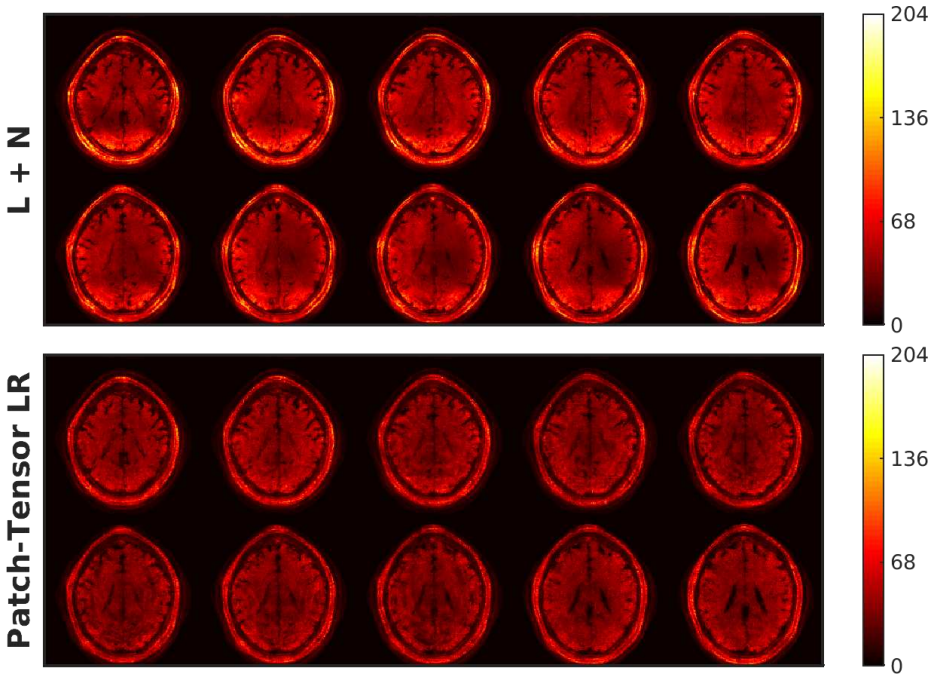

Figure 6.3: 3D OSSI temporal SNR map of the proposed model presents higher temporal SNR than the tensor low-rank model in Chapter III.

6.2.1 Transformers Related

Current Transformers use attention mechanisms that operate on matrices, which might be insufficiently general for high-dimensional data. To fully exploit high-dimensional information with attention mechanisms, we propose multi-dimensional attention. The multi-dimensional attention could model unfoldings of the high-dimensional tensor data as shown in recent work [135]. Furthermore, prior work [136] exploits low-rankness in 2D attention maps for efficient Transformers, while no works have been done for higher dimensional attention maps. Similar to the patch-tensor low-rank model in Chapter III, we propose to impose tensor low-rankness on high-dimensional attention maps.

We can also design a multi-dimensional attention mechanism. Instead of implementing it through unfolded matrices and matrix multiplication, we propose to implement the tensor attention with tensor multiplication. We could further incorporate sparsity constraints to encourage the high-dimensional attention maps to have sparse core tensors. Related works [137, 138] present sparse 2D attention maps.

Previous works such as inverting a CNN [139] for visualizing CNN representations

could potentially be extended to Transformers and would be interesting to investigate. More importantly, with the deep image prior [140] concept for unsupervised learning, we propose to use Transformers as the network architecture in deep image prior regularization for dynamic MRI sequence reconstruction.

For Transformer network design, we propose to use the hierarchical attention network as in [141] to model multi-scale spatial-temporal dependency of the image sequences for both self-supervised and unsupervised tasks.

6.2.2 More General Directions

We have considered some other interesting research directions and approaches:

- We can design a union of sparse subspaces model [142] to serve as a regularizer for for dynamic MRI reconstruction.
- We propose an MRI k-space inpainting model that exploits neighboring sample similarity using a local/adaptive SIREN network [143] for undersampled reconstruction.
- Another future research direction is to consider hierarchical and probabilistic network structures [144, 145, 146, 147, 148] to advance the learning and reasoning capacity of neural networks.

BIBLIOGRAPHY

[1] Albert Macovski. Noise in MRI. *Magnetic resonance in medicine*, 36(3):494–497, 1996.

[2] Song Lai and Gary H Glover. Three-dimensional spiral fMRI technique: a comparison with 2D spiral acquisition. *Magnetic resonance in medicine*, 39(1):68–78, 1998.

[3] Douglas C Noll. Methodologic considerations for spiral k-space functional MRI. *International Journal of Imaging Systems and Technology*, 6(2-3):175–183, 1995.

[4] Zhi-Pei Liang and Paul C Lauterbur. *Principles of magnetic resonance imaging*. SPIE Optical Engineering Press Bellingham, 2000.

[5] Dwight G Nishimura. *Principles of magnetic resonance imaging*. Standford Univ., 2010.

[6] David L Donoho. Compressed sensing. *IEEE Transactions on information theory*, 52(4):1289–1306, 2006.

[7] Michael Lustig, David L Donoho, Juan M Santos, and John M Pauly. Compressed sensing MRI. *IEEE signal processing magazine*, 25(2):72–82, 2008.

[8] Jeffrey A Fessler. Model-based image reconstruction for MRI. *IEEE signal processing magazine*, 27(4):81–89, 2010.

[9] Michael Lustig, David Donoho, and John M Pauly. Sparse MRI: The application of compressed sensing for rapid MR imaging. *Magnetic Resonance in Medicine: An Official Journal of the International Society for Magnetic Resonance in Medicine*, 58(6):1182–1195, 2007.

[10] Ricardo Otazo, Emmanuel Candes, and Daniel K Sodickson. Low-rank plus sparse matrix decomposition for accelerated dynamic MRI with separation of background and dynamic components. *Magnetic resonance in medicine*, 73(3):1125–1136, 2015.

[11] Saiprasad Ravishankar, Brian E Moore, Raj Rao Nadakuditi, and Jeffrey A Fessler. Low-rank and adaptive sparse signal (LASSI) models for highly accelerated dynamic imaging. *IEEE transactions on medical imaging*, 36(5):1116–1128, 2017.

[12] Saiprasad Ravishankar and Yoram Bresler. MR image reconstruction from highly undersampled k-space data by dictionary learning. *IEEE transactions on medical imaging*, 30(5):1028–1041, 2010.

[13] Jo Schlemper, Jose Caballero, Joseph V Hajnal, Anthony N Price, and Daniel Rueckert. A deep cascade of convolutional neural networks for dynamic MR image reconstruction. *IEEE transactions on Medical Imaging*, 37(2):491–503, 2017.

[14] Kerstin Hammernik, Teresa Klatzer, Erich Kobler, Michael P Recht, Daniel K Sodickson, Thomas Pock, and Florian Knoll. Learning a variational network for reconstruction of accelerated MRI data. *Magnetic resonance in medicine*, 79(6):3055–3071, 2018.

[15] Hemant K Aggarwal, Merry P Mani, and Mathews Jacob. MoDL: Model-based deep learning architecture for inverse problems. *IEEE transactions on medical imaging*, 38(2):394–405, 2018.

[16] Shouchang Guo and Douglas C Noll. Oscillating steady-state imaging (OSSI): A novel method for functional MRI. *Magnetic resonance in medicine*, 84(2):698–712, 2020.

[17] Oliver Bieri and Klaus Scheffler. Fundamentals of balanced steady state free precession MRI. *Journal of Magnetic Resonance Imaging*, 38(1):2–11, 2013.

[18] Y Zur, ML Wood, and LJ Neuringer. Spoiling of transverse magnetization in steady-state sequences. *Magnetic resonance in medicine*, 21(2):251–263, 1991.

[19] Shouchang Guo, Jeffrey A Fessler, and Douglas C Noll. High-resolution oscillating steady-state fMRI using patch-tensor low-rank reconstruction. *IEEE Transactions on Medical Imaging*, 39(12):4357–4368, 2020.

[20] Shouchang Guo, Jeffrey A Fessler, and Douglas C Noll. Manifold model for high-resolution fMRI joint reconstruction and dynamic quantification. *arXiv preprint arXiv:2104.08395*, 2021.

[21] Shouchang Guo and Douglas C Noll. High SNR functional MRI using oscillating steady state imaging. *Proceedings of International Society for Magnetic Resonance in Medicine, Paris*, page 5441, 2018.

[22] Shouchang Guo and Douglas C Noll. Comparison of oscillating steady state to GRE BOLD for fMRI. In *ISMRM 27th Annual Meeting*, page 1170, 2019.

[23] P van Gelderen, N F Ramsey, G Liu, J H Duyn, J A Frank, D R Weinberger, and C T Moonen. Three-dimensional functional magnetic resonance imaging of human brain on a clinical 1.5-T scanner. *Proceedings of the National Academy of Sciences of the United States of America*, 92(15):6906–10, jul 1995.

[24] Christoph Rettenmeier, Danilo Maziero, Yongxian Qian, and V. Andrew Stenger. A circular echo planar sequence for fast volumetric fMRI. *Magnetic Resonance in Medicine*, 81(3):1685–1698, mar 2019.

[25] Hao Sun, Jeffrey A. Fessler, Douglas C. Noll, and Jon-Fredrik Nielsen. Steady-state functional MRI using spoiled small-tip fast recovery imaging. *Magnetic Resonance in Medicine*, 73(2):536–543, feb 2015.

[26] Klaus Scheffler, Erich Seifritz, Deniz Bilecen, Ramesh Venkatesan, Jurgen Hennig, Michael Deimling, and E. Mark Haacke. Detection of BOLD changes by means of a frequency-sensitive trueFISP technique: preliminary results. *NMR in Biomedicine*, 14(7-8):490–496, nov 2001.

[27] Karla L. Miller, Brian A. Hargreaves, Jongho Lee, David Ress, R. Christopher deCharms, and John M. Pauly. Functional brain imaging using a blood oxygenation sensitive steady state. *Magnetic Resonance in Medicine*, 50(4):675–683, oct 2003.

[28] Kai Zhong, Jochen Leupold, Juergen Hennig, and Oliver Speck. Systematic investigation of balanced steady-state free precession for functional MRI in the human visual cortex at 3 Tesla. *Magnetic Resonance in Medicine*, 57(1):67–73, jan 2007.

[29] Karla L. Miller and Peter Jezzard. Modeling SSFP functional MRI contrast in the brain. *Magnetic Resonance in Medicine*, 60(3):661–673, sep 2008.

[30] Klaus Scheffler and Philipp Ehses. High-resolution mapping of neuronal activation with balanced SSFP at 9.4 tesla. *Magnetic Resonance in Medicine*, 76(1):163–171, jul 2016.

[31] Klaus Scheffler, Stefan Maderwald, Mark E. Ladd, and Oliver Bieri. Oscillating steady states. *Magnetic Resonance in Medicine*, 55(3):598–603, mar 2006.

[32] William R. Overall, Steven M. Conolly, Dwight G. Nishimura, and Bob S. Hu. Oscillating dual-equilibrium steady-state angiography. *Magnetic Resonance in Medicine*, 47(3):513–522, mar 2002.

[33] Y. Zur, M. L. Wood, and L. J. Neuringer. Spoiling of transverse magnetization in steady-state sequences. *Magnetic Resonance in Medicine*, 21(2):251–263, oct 1991.

[34] DL Foxall. Frequency-modulated steady-state free precession imaging. *Magnetic Resonance in Medicine*, 48(3):502–508, 2002.

[35] Charlie Yi Wang, Simone Coppo, Bhairav Bipin Mehta, Nicole Seiberlich, Xin Yu, and Mark Alan Griswold. Magnetic resonance fingerprinting with quadratic RF phase for measurement of T2* simultaneously with δf, T1, and T2. *Magnetic resonance in medicine*, 81(3):1849–1862, 2019.

[36] Relaxation Times. `https://itis.swiss/virtual-population/tissue-properties/database/relaxation-times/`. Accessed Jan. 16, 2020.

[37] Jerrold L. Boxerman, Leena M. Hamberg, Bruce R. Rosen, and Robert M. Weisskoff. Mr contrast due to intravascular magnetic susceptibility perturbations. *Magnetic Resonance in Medicine*, 34(4):555–566, oct 1995.

[38] Gary H Glover, Bryon A Mueller, Jessica A Turner, Theo G M van Erp, Thomas T Liu, Douglas N Greve, James T Voyvodic, Jerod Rasmussen, Gregory G Brown, David B Keator, Vince D Calhoun, Hyo Jong Lee, Judith M Ford, Daniel H Mathalon, Michele Diaz, Daniel S O'Leary, Syam Gadde, Adrian Preda, Kelvin O Lim, Cynthia G Wible, Hal S Stern, Aysenil Belger, Gregory McCarthy, Burak Ozyurt, Steven G Potkin, and FBIRN. Function biomedical informatics research network recommendations for prospective multicenter functional MRI studies. *Journal of magnetic resonance imaging : JMRI*, 36(1):39–54, jul 2012.

[39] Stephen M Smith. Fast robust automated brain extraction. *Human brain mapping*, 17(3):143–155, 2002.

[40] Martin Uecker, Peng Lai, Mark J Murphy, Patrick Virtue, Michael Elad, John M Pauly, Shreyas S Vasanawala, and Michael Lustig. ESPIRiT—an eigenvalue approach to autocalibrating parallel MRI: where SENSE meets GRAPPA. *Magnetic resonance in medicine*, 71(3):990–1001, 2014.

[41] Martin Uecker, Frank Ong, Jonathan I Tamir, Dara Bahri, Patrick Virtue, Joseph Y Cheng, Tao Zhang, and Michael Lustig. Berkeley advanced reconstruction toolbox. In *Proceedings of the 23th Annual Meeting of ISMRM, Montreal*, page 2486, 2015.

[42] Klaas P Pruessmann, Markus Weiger, Peter Börnert, and Peter Boesiger. Advances in sensitivity encoding with arbitrary k-space trajectories. *Magnetic*

Resonance in Medicine: An Official Journal of the International Society for Magnetic Resonance in Medicine, 46(4):638–651, 2001.

[43] Bradley P Sutton, Douglas C Noll, and Jeffrey A Fessler. Fast, iterative image reconstruction for MRI in the presence of field inhomogeneities. *IEEE transactions on medical imaging*, 22(2):178–188, 2003.

[44] Jeff Fessler. Michigan Image Reconstruction Toolbox. `https://web.eecs.umich.edu/~fessler/code/index.html`. Accessed Jan. 16, 2020.

[45] Statistical Parametric Mapping. `https://www.fil.ion.ucl.ac.uk/spm/`. Accessed Jan. 16, 2020.

[46] Tao Jin, Ping Wang, Michelle Tasker, Fuqiang Zhao, and Seong-Gi Kim. Source of nonlinearity in echo-time-dependent BOLD fMRI. *Magnetic Resonance in Medicine: An Official Journal of the International Society for Magnetic Resonance in Medicine*, 55(6):1281–1290, 2006.

[47] Gunnar Krüger and Gary H. Glover. Physiological noise in oxygenation-sensitive magnetic resonance imaging. *Magnetic Resonance in Medicine*, 46(4):631–637, 2001.

[48] D.C. Noll and W. Schneider. Theory, simulation, and compensation of physiological motion artifacts in functional MRI. In *Proceedings of 1st International Conference on Image Processing*, volume 3, pages 40–44. IEEE Comput. Soc. Press, 1994.

[49] G H Glover, T Q Li, and D Ress. Image-based method for retrospective correction of physiological motion effects in fMRI: RETROICOR. *Magnetic resonance in medicine*, 44(1):162–7, jul 2000.

[50] X Hu, T H Le, T Parrish, and P Erhard. Retrospective estimation and correction of physiological fluctuation in functional MRI. *Magnetic resonance in medicine*, 34(2):201–12, aug 1995.

[51] Amos A. Cao, Shouchang Guo, and Douglas C. Noll. Dynamic model-based reconstruction for oscillating steady state fMRI. In *Proceedings of the 27th Annual Meeting of ISMRM, Montreal*, page 3771, 2019.

[52] Shouchang Guo and Douglas C. Noll. Patch-tensor low-n-rank reconstruction for oscillating steady state fMRI acceleration. In *Proceedings of the 26th Annual Meeting of ISMRM, Paris*, page 3531, 2018.

[53] Shouchang Guo, Douglas C. Noll, and Jeffrey A. Fessler. Dictionary-based oscillating steady state fMRI reconstruction. In *Proceedings of the 27th Annual Meeting of ISMRM, Montreal*, page 1253, 2019.

[54] Steen Moeller, Essa Yacoub, Cheryl A Olman, Edward Auerbach, John Strupp, Noam Harel, and Kâmil Uğurbil. Multiband multislice GE-EPI at 7 tesla, with 16-fold acceleration using partial parallel imaging with application to high spatial and temporal whole-brain fMRI. *Magnetic resonance in medicine*, 63(5):1144–53, may 2010.

[55] Kawin Setsompop, Borjan A. Gagoski, Jonathan R. Polimeni, Thomas Witzel, Van J. Wedeen, and Lawrence L. Wald. Blipped-controlled aliasing in parallel imaging for simultaneous multislice echo planar imaging with reduced g-factor penalty. *Magnetic Resonance in Medicine*, 67(5):1210–1224, may 2012.

[56] Benjamin Zahneisen, Benedikt A Poser, Thomas Ernst, and V Andrew Stenger. Three-dimensional Fourier encoding of simultaneously excited slices: generalized acquisition and reconstruction framework. *Magnetic resonance in medicine*, 71(6):2071–81, jun 2014.

[57] Carl Ganter. Steady state of gradient echo sequences with radiofrequency phase cycling: Analytical solution, contrast enhancement with partial spoiling. *Magnetic Resonance in Medicine*, 55(1):98–107, jan 2006.

[58] Shouchang Guo, Jeffrey A Fessler, and Douglas C Noll. High SNR and high-resolution fMRI using 3D OSSI and tensor model reconstruction. In *Proceedings of the 27th Annual Meeting of ISMRM, Montreal*, page 3862, 2019.

[59] Scott A Huettel, Allen W Song, Gregory McCarthy, et al. *Functional magnetic resonance imaging*, volume 1. Sinauer Associates Sunderland, MA, 2004.

[60] Mark Chiew, Stephen M Smith, Peter J Koopmans, Nadine N Graedel, Thomas Blumensath, and Karla L Miller. k-t FASTER: acceleration of functional MRI data acquisition using low rank constraints. *Magnetic resonance in medicine*, 74(2):353–364, 2015.

[61] Fan Lam, Bo Zhao, Yinan Liu, Zhi-Pei Liang, Michael Weiner, and Norbert Schuff. Accelerated fMRI using low-rank model and sparsity constraints. *Proc. Int. Soc. Magn. Reson. Med. Salt Lake City*, page 2013, 2013.

[62] Andrii Y Petrov, Michael Herbst, and V Andrew Stenger. Improving temporal resolution in fMRI using a 3D spiral acquisition and low rank plus sparse (L+S) reconstruction. *Neuroimage*, 157:660–674, 2017.

[63] Ricardo Otazo, Emmanuel Candes, and Daniel K Sodickson. Low-rank plus sparse matrix decomposition for accelerated dynamic MRI with separation of background and dynamic components. *Magnetic resonance in medicine*, 73(3):1125–1136, 2015.

[64] Ji Liu, Przemyslaw Musialski, Peter Wonka, and Jieping Ye. Tensor completion for estimating missing values in visual data. *IEEE transactions on pattern analysis and machine intelligence*, 35(1):208–220, 2012.

[65] Silvia Gandy, Benjamin Recht, and Isao Yamada. Tensor completion and low-n-rank tensor recovery via convex optimization. *Inverse Problems*, 27(2):025010, 2011.

[66] Shahrooz F Roohi, Dornoosh Zonoobi, Ashraf A Kassim, and Jacob L Jaremko. Multi-dimensional low rank plus sparse decomposition for reconstruction of under-sampled dynamic MRI. *Pattern Recognition*, 63:667–679, 2017.

[67] Rebecca Ramb, Michael Zenge, Li Feng, Matthew Muckley, Christoph Forman, Leon Axel, Dan Sodickson, and Ricardo Otazo. Low-rank plus sparse tensor reconstruction for high-dimensional cardiac MRI. In *Proc. Int. Society Magnetic Resonance Medicine*, page 1199, 2017.

[68] Anthony G Christodoulou, Jaime L Shaw, Christopher Nguyen, Qi Yang, Yibin Xie, Nan Wang, and Debiao Li. Magnetic resonance multitasking for motion-resolved quantitative cardiovascular imaging. *Nature biomedical engineering*, 2(4):215–226, 2018.

[69] Lieven De Lathauwer, Bart De Moor, and Joos Vandewalle. A multilinear singular value decomposition. *SIAM journal on Matrix Analysis and Applications*, 21(4):1253–1278, 2000.

[70] Yeyang Yu, Jin Jin, Feng Liu, and Stuart Crozier. Multidimensional compressed sensing MRI using tensor decomposition-based sparsifying transform. *PloS one*, 9(6):e98441, 2014.

[71] Jingfei He, Qiegen Liu, Anthony G Christodoulou, Chao Ma, Fan Lam, and Zhi-Pei Liang. Accelerated high-dimensional MR imaging with sparse sampling using low-rank tensors. *IEEE transactions on medical imaging*, 35(9):2119–2129, 2016.

[72] Chao Ma, Bryan Clifford, Yuchi Liu, Yuning Gu, Fan Lam, Xin Yu, and Zhi-Pei Liang. High-resolution dynamic 31P-MRSI using a low-rank tensor model. *Magnetic resonance in medicine*, 78(2):419–428, 2017.

[73] Anthony G Christodoulou, Gage Redler, Bryan Clifford, Zhi-Pei Liang, Howard J Halpern, and Boris Epel. Fast dynamic electron paramagnetic resonance (EPR) oxygen imaging using low-rank tensors. *Journal of Magnetic Resonance*, 270:176–182, 2016.

[74] Burhaneddin Yaman, Sebastian Weingärtner, Nikolaos Kargas, Nicholas D Sidiropoulos, and Mehmet Akçakaya. Low-Rank Tensor Models for Improved Multidimensional MRI: Application to Dynamic Cardiac T_1 Mapping. *IEEE transactions on computational imaging*, 6:194–207, 2019.

[75] Charilaos I Kanatsoulis, Xiao Fu, Nicholas D Sidiropoulos, and Mehmet Akçakaya. Tensor completion from regular sub-Nyquist samples. *IEEE Transactions on Signal Processing*, 68:1–16, 2019.

[76] Joshua D Trzasko and Armando Manduca. A unified tensor regression framework for calibrationless dynamic, multi-channel MRI reconstruction. In *Proceedings of the 21st Annual Meeting of ISMRM, Salt Lake City, Utah, USA*, volume 603, page 21, 2013.

[77] Joshua D Trzasko. Exploiting local low-rank structure in higher-dimensional MRI applications. In *Wavelets and Sparsity XV*, volume 8858, page 885821. International Society for Optics and Photonics, 2013.

[78] Aurélien Bustin, Gastão Lima da Cruz, Olivier Jaubert, Karina Lopez, René M Botnar, and Claudia Prieto. High-dimensionality undersampled patch-based reconstruction (HD-PROST) for accelerated multi-contrast MRI. *Magnetic resonance in medicine*, 81(6):3705–3719, 2019.

[79] Stephen Boyd, Neal Parikh, and Eric Chu. Distributed optimization and statistical learning via the alternating direction method of multipliers. *Foundations and Trends in Machine Learning*, 3(1):1–122, 2011.

[80] Mário AT Figueiredo and Robert D Nowak. An EM algorithm for wavelet-based image restoration. *IEEE Transactions on Image Processing*, 12(8):906–916, 2003.

[81] Frank Ong and Michael Lustig. Beyond low rank+ sparse: Multiscale low rank matrix decomposition. *IEEE journal of selected topics in signal processing*, 10(4):672–687, 2016.

[82] J Trzasko, A Manduca, and E Borisch. Local versus global low-rank promotion in dynamic MRI series reconstruction. In *Proc. Int. Symp. Magn. Reson. Med*, volume 19, page 4371, 2011.

[83] Chi-Ming Tsai and Dwight G Nishimura. Reduced aliasing artifacts using variable-density k-space sampling trajectories. *Magnetic Resonance in Medicine: An Official Journal of the International Society for Magnetic Resonance in Medicine*, 43(3):452–458, 2000.

[84] Juan M Santos, Charles H Cunningham, Michael Lustig, Brian A Hargreaves, Bob S Hu, Dwight G Nishimura, and John M Pauly. Single breath-hold whole-heart MRA using variable-density spirals at 3T. *Magnetic Resonance in Medicine: An Official Journal of the International Society for Magnetic Resonance in Medicine*, 55(2):371–379, 2006.

[85] Brian Hargreaves. Variable-Density Spiral Design Functions. `http://mrsrl.stanford.edu/~brian/vdspiral/`. Accessed Jan. 16, 2020.

[86] Jin Hyung Lee, Brian A Hargreaves, Bob S Hu, and Dwight G Nishimura. Fast 3D imaging using variable-density spiral trajectories with applications to limb perfusion. *Magnetic Resonance in Medicine: An Official Journal of the International Society for Magnetic Resonance in Medicine*, 50(6):1276–1285, 2003.

[87] Michael Lustig, David Donoho, and John M Pauly. Sparse MRI: The application of compressed sensing for rapid MR imaging. *Magnetic Resonance in Medicine: An Official Journal of the International Society for Magnetic Resonance in Medicine*, 58(6):1182–1195, 2007.

[88] Feng Huang, Sathya Vijayakumar, Yu Li, Sarah Hertel, and George R Duensing. A software channel compression technique for faster reconstruction with many channels. *Magnetic resonance imaging*, 26(1):133–141, 2008.

[89] Jeffrey A Fessler and W Leslie Rogers. Spatial resolution properties of penalized-likelihood image reconstruction: space-invariant tomographs. *IEEE Transactions on Image processing*, 5(9):1346–1358, 1996.

[90] Valur T Olafsson, Douglas C Noll, and Jeffrey A Fessler. Fast spatial resolution analysis of quadratic penalized Least-Squares image reconstruction with separate real and imaginary roughness penalty: Application to fMRI. *IEEE transactions on medical imaging*, 37(2):604–614, 2017.

[91] Sunrita Poddar, Yasir Q Mohsin, Deidra Ansah, Bijoy Thattaliyath, Ravi Ashwath, and Mathews Jacob. Manifold recovery using kernel low-rank regularization: Application to dynamic imaging. *IEEE Transactions on Computational Imaging*, 5(3):478–491, 2019.

[92] Saiprasad Ravishankar, Brian E Moore, Raj Rao Nadakuditi, and Jeffrey A Fessler. Low-rank and adaptive sparse signal (LASSI) models for highly accelerated dynamic imaging. *IEEE transactions on medical imaging*, 36(5):1116–1128, 2017.

[93] Feng Xue and Thierry Blu. On The Degrees Of Freedom in Total Variation Minimization. In *ICASSP 2020-2020 IEEE International Conference on Acoustics, Speech and Signal Processing (ICASSP)*, pages 5690–5694. IEEE, 2020.

[94] Baran Gözcü, Rabeeh Karimi Mahabadi, Yen-Huan Li, Efe Ilıcak, Tolga Çukur, Jonathan Scarlett, and Volkan Cevher. Learning-based compressive MRI. *IEEE transactions on medical imaging*, 37(6):1394–1406, 2018.

[95] Cagla D Bahadir, Alan Q Wang, Adrian V Dalca, and Mert R Sabuncu. Deep-learning-based optimization of the under-sampling pattern in MRI. *IEEE Transactions on Computational Imaging*, 6:1139–1152, 2020.

[96] Shouchang Guo, Douglas C. Noll, and Jeffrey A. Fessler. OSSI manifold model for high-resolution fMRI joint reconstruction and quantification. In *Proceedings of the 28th Annual Meeting of ISMRM, Montreal*, page 1018, 2020.

[97] Seiji Ogawa, Tso-Ming Lee, Asha S Nayak, and Paul Glynn. Oxygenation-sensitive contrast in magnetic resonance image of rodent brain at high magnetic fields. *Magnetic resonance in medicine*, 14(1):68–78, 1990.

[98] Douglas C Noll. A primer on MRI and functional MRI. *Technical Raport, University of Michigan*, 2001.

[99] Bo Zhao, Kawin Setsompop, Huihui Ye, Stephen F Cauley, and Lawrence L Wald. Maximum likelihood reconstruction for magnetic resonance fingerprinting. *IEEE transactions on medical imaging*, 35(8):1812–1823, 2016.

[100] Jakob Assländer, Martijn A Cloos, Florian Knoll, Daniel K Sodickson, Jürgen Hennig, and Riccardo Lattanzi. Low rank alternating direction method of multipliers reconstruction for MR fingerprinting. *Magnetic resonance in medicine*, 79(1):83–96, 2018.

[101] Guozhi Dong, Michael Hintermüller, and Kostas Papafitsoros. Quantitative magnetic resonance imaging: From fingerprinting to integrated physics-based models. *SIAM Journal on Imaging Sciences*, 12(2):927–971, 2019.

[102] Jonathan I Tamir, Frank Ong, Suma Anand, Ekin Karasan, Ke Wang, and Michael Lustig. Computational MRI with physics-based constraints: Application to multicontrast and quantitative imaging. *IEEE Signal Processing Magazine*, 37(1):94–104, 2020.

[103] Oliver Speck and Jürgen Hennig. Functional Imaging by I0-and T2*-parameter mapping using multi-image EPI. *Magnetic resonance in medicine*, 40(2):243–248, 1998.

[104] Anders BA Wennerberg, Tomas Jonsson, Hans Forssberg, and Tie-Qiang Li. A comparative fMRI study: T2*-weighted imaging versus R2* mapping. *NMR in Biomedicine: An International Journal Devoted to the Development and Application of Magnetic Resonance In Vivo*, 14(1):41–47, 2001.

[105] Valur T Olafsson, Douglas C Noll, and Jeffrey A Fessler. Fast Joint Reconstruction of Dynamic R2* and Field Maps in Functional MRI. *IEEE transactions on medical imaging*, 27(9):1177–1188, 2008.

[106] Gene H Golub and Victor Pereyra. The differentiation of pseudo-inverses and nonlinear least squares problems whose variables separate. *SIAM Journal on numerical analysis*, 10(2):413–432, 1973.

[107] Gene Golub and Victor Pereyra. Separable nonlinear least squares: the variable projection method and its applications. *Inverse problems*, 19(2):R1, 2003.

[108] Donghwan Kim and Jeffrey A Fessler. Adaptive restart of the optimized gradient method for convex optimization. *Journal of Optimization Theory and Applications*, 178(1):240–263, 2018.

[109] Adrien B Taylor, Julien M Hendrickx, and François Glineur. Exact worst-case performance of first-order methods for composite convex optimization. *SIAM Journal on Optimization*, 27(3):1283–1313, 2017.

[110] C. Y. Lin and J. A. Fessler. Efficient dynamic parallel MRI reconstruction for the low-rank plus sparse model. *IEEE Trans. Computational Imaging*, 5(1):17–26, March 2019.

[111] Patrice Péran, Gisela Hagberg, Giacomo Luccichenti, Andrea Cherubini, Valentina Brainovich, Pierre Celsis, Carlo Caltagirone, and Umberto Sabatini. Voxel-based analysis of R2* maps in the healthy human brain. *Journal of Magnetic Resonance Imaging: An Official Journal of the International Society for Magnetic Resonance in Medicine*, 26(6):1413–1420, 2007.

[112] Douglas C Noll, Jonathan D Cohen, Craig H Meyer, and Walter Schneider. Spiral k-space MR imaging of cortical activation. *Journal of Magnetic Resonance Imaging*, 5(1):49–56, 1995.

[113] Chen Qin, Jo Schlemper, Jose Caballero, Anthony N Price, Joseph V Hajnal, and Daniel Rueckert. Convolutional recurrent neural networks for dynamic MR image reconstruction. *IEEE transactions on medical imaging*, 38(1):280–290, 2018.

[114] Dzmitry Bahdanau, Kyunghyun Cho, and Yoshua Bengio. Neural machine translation by jointly learning to align and translate. *arXiv preprint arXiv:1409.0473*, 2014.

[115] Ashish Vaswani, Noam Shazeer, Niki Parmar, Jakob Uszkoreit, Llion Jones, Aidan N Gomez, Lukasz Kaiser, and Illia Polosukhin. Attention is all you need. *arXiv preprint arXiv:1706.03762*, 2017.

[116] Shouchang Guo, Jeffrey A. Fessler, and Douglas C. Noll. Voxel-wise temporal attention network and simulation-driven dynamic MRI sequence reconstruction. In *Proceedings of the 30th Annual Meeting of ISMRM, London*, page 4050, 2022.

[117] Alex Krizhevsky, Ilya Sutskever, and Geoffrey E Hinton. Imagenet classification with deep convolutional neural networks. *Advances in neural information processing systems*, 25:1097–1105, 2012.

[118] Kaiming He, Xiangyu Zhang, Shaoqing Ren, and Jian Sun. Deep residual learning for image recognition. In *Proceedings of the IEEE conference on computer vision and pattern recognition*, pages 770–778, 2016.

[119] Guilin Liu, Rohan Taori, Ting-Chun Wang, Zhiding Yu, Shiqiu Liu, Fitsum A Reda, Karan Sapra, Andrew Tao, and Bryan Catanzaro. Transposer: Universal texture synthesis using feature maps as transposed convolution filter. *arXiv preprint arXiv:2007.07243*, 2020.

[120] Morteza Mardani, Guilin Liu, Aysegul Dundar, Shiqiu Liu, Andrew Tao, and Bryan Catanzaro. Neural ffts for universal texture image synthesis. *Advances in Neural Information Processing Systems*, 33:14081–14092, 2020.

[121] Joao Carreira and Andrew Zisserman. Quo vadis, action recognition? a new model and the kinetics dataset. In *proceedings of the IEEE Conference on Computer Vision and Pattern Recognition*, pages 6299–6308, 2017.

[122] Shouchang Guo and Douglas C. Noll. Recurrent u-net based temporal regularization for dynamic undersampled reconstruction in OSSI fMRI. In *Proceedings of the 29th Annual Meeting of ISMRM, Virtual*, page 2698, 2021.

[123] Xiaolong Wang, Ross Girshick, Abhinav Gupta, and Kaiming He. Non-local neural networks. In *Proceedings of the IEEE conference on computer vision and pattern recognition*, pages 7794–7803, 2018.

[124] Alexey Dosovitskiy, Lucas Beyer, Alexander Kolesnikov, Dirk Weissenborn, Xiaohua Zhai, Thomas Unterthiner, Mostafa Dehghani, Matthias Minderer, Georg Heigold, Sylvain Gelly, et al. An image is worth 16x16 words: Transformers for image recognition at scale. *arXiv preprint arXiv:2010.11929*, 2020.

[125] Jimmy Lei Ba, Jamie Ryan Kiros, and Geoffrey E Hinton. Layer normalization. *arXiv preprint arXiv:1607.06450*, 2016.

[126] Jacob Devlin, Ming-Wei Chang, Kenton Lee, and Kristina Toutanova. Bert: Pre-training of deep bidirectional transformers for language understanding. *arXiv preprint arXiv:1810.04805*, 2018.

[127] Tom B Brown, Benjamin Mann, Nick Ryder, Melanie Subbiah, Jared Kaplan, Prafulla Dhariwal, Arvind Neelakantan, Pranav Shyam, Girish Sastry, Amanda Askell, et al. Language models are few-shot learners. *arXiv preprint arXiv:2005.14165*, 2020.

[128] Hanting Chen, Yunhe Wang, Tianyu Guo, Chang Xu, Yiping Deng, Zhenhua Liu, Siwei Ma, Chunjing Xu, Chao Xu, and Wen Gao. Pre-trained image processing transformer. *arXiv preprint arXiv:2012.00364*, 2020.

[129] Ze Liu, Yutong Lin, Yue Cao, Han Hu, Yixuan Wei, Zheng Zhang, Stephen Lin, and Baining Guo. Swin transformer: Hierarchical vision transformer using shifted windows. In *Proceedings of the IEEE/CVF International Conference on Computer Vision*, pages 10012–10022, 2021.

[130] Han Zhang, Ian Goodfellow, Dimitris Metaxas, and Augustus Odena. Self-attention generative adversarial networks. In *International conference on machine learning*, pages 7354–7363. PMLR, 2019.

[131] Yanhong Zeng, Jianlong Fu, and Hongyang Chao. Learning joint spatial-temporal transformations for video inpainting. In *European Conference on Computer Vision*, pages 528–543. Springer, 2020.

[132] Dmitry Ulyanov, Andrea Vedaldi, and Victor Lempitsky. Instance normalization: The missing ingredient for fast stylization. *arXiv preprint arXiv:1607.08022*, 2016.

[133] M. J. Muckley, R. Stern, T. Murrell, and F. Knoll. TorchKbNufft: A high-level, hardware-agnostic non-uniform fast Fourier transform. In *ISMRM Workshop on Data Sampling & Image Reconstruction*, 2020. Source code available at https://github.com/mmuckley/torchkbnufft.

[134] Özgün Çiçek, Ahmed Abdulkadir, Soeren S Lienkamp, Thomas Brox, and Olaf Ronneberger. 3D U-Net: learning dense volumetric segmentation from sparse annotation. In *International conference on medical image computing and computer-assisted intervention*, pages 424–432. Springer, 2016.

[135] Francesca Babiloni, Ioannis Marras, Gregory Slabaugh, and Stefanos Zafeiriou. TESA: Tensor Element Self-Attention via Matricization. In *Proceedings of the IEEE/CVF Conference on Computer Vision and Pattern Recognition*, pages 13945–13954, 2020.

[136] Sinong Wang, Belinda Z Li, Madian Khabsa, Han Fang, and Hao Ma. Linformer: Self-attention with linear complexity. *arXiv preprint arXiv:2006.04768*, 2020.

[137] Andre Martins and Ramon Astudillo. From softmax to sparsemax: A sparse model of attention and multi-label classification. In *International Conference on Machine Learning*, pages 1614–1623. PMLR, 2016.

[138] Pedro Henrique Martins, Vlad Niculae, Zita Marinho, and André Martins. Sparse and Structured Visual Attention. *arXiv preprint arXiv:2002.05556*, 2020.

[139] Aravindh Mahendran and Andrea Vedaldi. Visualizing deep convolutional neural networks using natural pre-images. *International Journal of Computer Vision*, 120(3):233–255, 2016.

[140] Dmitry Ulyanov, Andrea Vedaldi, and Victor Lempitsky. Deep image prior. In *Proceedings of the IEEE conference on computer vision and pattern recognition*, pages 9446–9454, 2018.

[141] Shouchang Guo, Valentin Deschaintre, Douglas Noll, and Arthur Roullier. Paying u-attention to textures: Multi-stage hourglass vision Transformer for universal texture synthesis. *arXiv preprint arXiv:2202.11703*, 2022.

[142] Ehsan Elhamifar and René Vidal. Sparse subspace clustering: Algorithm, theory, and applications. *IEEE transactions on pattern analysis and machine intelligence*, 35(11):2765–2781, 2013.

[143] Vincent Sitzmann, Julien Martel, Alexander Bergman, David Lindell, and Gordon Wetzstein. Implicit neural representations with periodic activation functions. *Advances in Neural Information Processing Systems*, 33:7462–7473, 2020.

[144] Geoffrey Hinton. How to represent part-whole hierarchies in a neural network. *arXiv preprint arXiv:2102.12627*, 2021.

[145] Frederic Morin and Yoshua Bengio. Hierarchical probabilistic neural network language model. In *International workshop on artificial intelligence and statistics*, pages 246–252. PMLR, 2005.

[146] Zichao Yang, Diyi Yang, Chris Dyer, Xiaodong He, Alex Smola, and Eduard Hovy. Hierarchical attention networks for document classification. In *Proceedings of the 2016 conference of the North American chapter of the association for computational linguistics: human language technologies*, pages 1480–1489, 2016.

[147] Balaji Lakshminarayanan, Alexander Pritzel, and Charles Blundell. Simple and scalable predictive uncertainty estimation using deep ensembles. *Advances in neural information processing systems*, 30, 2017.

[148] Raja Giryes, Guillermo Sapiro, and Alex M Bronstein. Deep neural networks with random gaussian weights: A universal classification strategy? *IEEE Transactions on Signal Processing*, 64(13):3444–3457, 2016.